A Study of Pollutant Formation from the Lean Premixed Combustion of Gaseous
Fuel Alternatives to Natural Gas

K.B. Fackler

A dissertation

submitted in partial fulfillment of the

requirements for the degree of

Doctor of Philosophy

University of Washington

2011

Philip Malte, Co-Chair

John Kramlich, Co-Chair

Igor Novosselov

Program Authorized to Offer Degree:

Mechanical Engineering

University of Washington

Abstract

A Study of Pollutant Formation from the Lean Premixed Combustion of Gaseous Fuel Alternatives to Natural Gas

K.B. Fackler

Co-Chairs of the Supervisory Committee:
Professor P.C. Malte
Department of Mechanical Engineering

Professor J.C. Kramlich
Department of Mechanical Engineering

The goal of this research is to identify how nitrogen oxide (NO_X) emissions and flame stability (blowout) are impacted by the use of fuels that are alternatives to typical pipeline natural gas. The research focuses on lean, premixed combustors that are typically used in state-of-the-art natural gas fueled systems. An idealized laboratory lean premixed combustor, specifically the jet-stirred reactor, is used for experimental data. A series of models, including those featuring detailed fluid dynamics and those focusing on detailed chemistry, are used to interpret the data and understand the underlying chemical kinetic reasons for differences in emissions between the various fuel blends. An ultimate goal is to use these data and interpretive tools to develop a way to predict the emission and stability impacts of changing fuels within practical combustors.

All experimental results are obtained from a high intensity, single-jet stirred reactor (JSR). Five fuel categories are studied: (1) pure H_2, (2) process and refinery gas, including combinations of H_2, CH_4, C_2H_6, and C_3H_8, (3) oxygen blown gasified coal/petcoke composed of H_2, CO, and CO_2, (4) landfill and digester gas composed

of CH_4, CO_2, and N_2, and (5) liquified natural gas (LNG)/shale/associated gases composed of CH_4, C_2H_6, and C_3H_8. NO_X measurements are taken at a nominal combustion temperature of 1800 K, atmospheric pressure, and a reactor residence time of 3 ms. This is done to focus the results on differences caused by fuel chemistry by comparing all fuels at a common temperature, pressure, and residence time. This is one of the few studies in the literature that attempts to remove these effects when studying fuels varying in composition. Additionally, the effects of changing temperature and residence time are investigated for selected fuels. At the nominal temperature and residence time, the experimental and modelling results show the following trends for NO_X emissions as a function of fuel type:

1. NO_X emissions decrease with increasing H_2 fuel fraction for combustion of CH_4/H_2 blends. This appears to be caused by a reduction in the amount of NO made by the prompt pathway involving the reaction of N_2 with hydrocarbon radicals as the CH_4 is replaced by H_2.

2. For category 2 (the process and refinery blend) and category 5 (the LNG, shale, and associated gases), NO_X emissions increase with the addition of C_2 and C_3 hydrocarbons. This appears to be due to an increased production of free radicals resulting from increasing CO production when higher molecular weight hydrocarbons are broken down.

3. For category 3 (the O_2 blown gasified coal/petcoke), NO_X emissions increase with increasing CO fuel fraction. The reason for this is attributed to CO producing more radicals per unit heat release than H_2. When CO replaces H_2, an increase in NO_X emissions is seen due to an increase in the productivity of the N_2O and Zeldovich pathways.

4. For category 4 (the landfill gas) the addition of diluents such as CO_2 and N_2 at constant air flow produces more NO_X per kg of CH_4 consumed, and N_2 is more effective than CO_2 in increasing the NO_X emission index. The increase in emission index appears to be due to an enhancement of the prompt NO_X pathway as the diluents are added and the mixture moves towards stoichiometric. In addition, the presence of CO_2 as a diluent catalyzes the loss of flame radicals, leading to less NO_X formation than when an equivalent amount of N_2 is used as a diluent.

For a selected set of fuels, detailed spacial reactor probing is carried out. At the nominal temperature and residence time, the experimental results show the following trends for flame structure as a function of fuel type:

1. Pure H_2 is far more reactive in comparison to CH_4 and all other pure alkane fuels. This results in relatively flat NO_X and temperature profiles; whereas, the alkane fuels drop in both temperature and NO_X production in the jet, where more fresh reactor feed gases are present.

2. For category 2 (the Process and Refinery blends), H_2 addition increases reactivity in the jet while decreasing overall NO_X emissions. The increased reactivity is especially evident in the CO profiles where the fuels blended with C_2H_6 and H_2 have CO peaks on jet centerline and CO for pure CH_4 peaks slightly off centerline.

3. For category 3 (the O_2 blown gasified coal/petcoke), the temperature profiles for the gasification blend and pure H_2 are nearly identical, which is likely due to the high reactivity of H_2 dominating the relatively low reactivity of CO. Despite a small temperature difference, the addition of CO causes an increase in NO_X production.

4. For category 4 (the landfill gas), the temperature profiles are virtually indistinguishable. However, the addition of diluent decreases reactivity and spreads out the reaction zone with the CO concentration peaking at 2 mm off of centerline instead of 1 mm. Diluent addition increases NO_X production in comparison to pure CH_4 for reasons explained above.

5. For category 5 (the LNG, shale, and associated gases), the temperature profiles are all very similar. The increased reactivity of C_2H_6 is evident from looking at the CO profiles. Increased C_2H_6 promotes CO production on jet centerline which is indicative of the hydrocarbon material breaking down earlier in the jet.

At temperatures and residence times other than the nominal conditions, the experimental results show the following trends:

1. The NO_X emissions from LPM combustion of pure CH_4, H_2, C_2H_6, and C_3H_8 are shown to vary linearly with residence time and in an Arrhenius fashion with temperature. This occurs because (1) more reaction time leads to more NO_X formation, and (2) NO_X formation is a strong, non-linear function of temperature.

2. The addition of both H_2 and C_2H_6 to a LPM CH_4 flame is effective at extending its lean blowout limit.

The results of both two and three dimensional CFD simulations are presented to illustrate the general flow, temperature, and species structure within the reactor. Since the two dimensional model is far more computationally efficient, it is employed to study various fuel mixtures with more sophisticated chemical mechanisms. The CFD results from the LPM combustion of H_2, H_2/CO, and CH_4 with NO_X formation are presented.

A three dimensional CFD simulation is run for LPM CH_4 combustion that uses a global CH_4 oxidation mechanism. While this model does not predict intermediate radicals and NO_X, the CO contours and flow field can be used as guidelines to develop a chemical reactor network (CRN), which can incorporate detailed chemistry. In addition, this model runs quickly enough that it is a good way to initialize the temperature and flow field for simulations that do incorporate more complex chemistry.

The two dimensional model is used to illustrate the difference in combustion behavior between the various fuels tested. In particular, it illustrates the geometric locations of the super-equilibrium radical fields and shows where and through which pathways NO_X is formed. The pathway breakdowns show good agreement with the CRN modeling results.

The main goal of the CFD modeling is to use the results of each model to develop Chemical Reactor Networks, CRNs, that are customized for a particular burner. The CRN can then be used to estimate the impacts due to fuel variation.

TABLE OF CONTENTS

LIST OF FIGURES

vii

LIST OF TABLES

ACKNOWLEDGMENTS

DEDICATION

To my sister and parents.

Chapter 1

INTRODUCTION

1.1 Overview

Lean-premixed (LPM) combustion technology is utilized in state of the art gas turbines to provide extremely efficient power generation with low emissions. Traditionally, natural gas has been used almost exclusively in LPM combustion. While extensive research on natural gas-fueled LPM combustion has been reported, much less research has been conducted on the use of alternatives to natural gas for LPM combustion devices. In the future, gas turbines will be run with a variety of fuel compositions ranging from syngases with high H_2 content to landfill and digester gas, which are mainly composed of CH_4, CO_2, and N_2. Alternative fuel blends will have a wide range of heating values, flame speeds, and chemical composition. It is important to study the behavior of these fuels under LPM conditions to maximize performance efficiency, while minimizing the overall emissions. In order to use alternative fuels effectively, knowledge must be gained pertaining to the expected emissions at comparable combustion temperatures as well as the relative resistance to blowout.

The range of fuel compositions studied in this work is shown below in Table 1.1. It is the goal of this research to study fuel blends that will typify the composition of future fuels. Five fuel categories are studied: (1) pure H_2, (2) process and refinery gas, including combinations of H_2, CH_4, C_2H_6, and C_3H_8, (3) oxygen blown gasified coal/petcoke composed of H_2, CO, and CO_2, (4) landfill and digester gas composed of CH_4, CO_2, and N_2, and (5) liquified natural gas (LNG)/shale/associated gases composed mainly of CH_4, C_2H_6, and C_3H_8. The baseline fuel for which all blends are

compared is CH_4. In addition to the blends outlined in Table 1.1, it is of both academic and general interest to perform parameterized studies within each fuel blend. Parameterized studies allow one to track differences that arise from variations in composition. As an example, we study mixtures of H_2/CH_4 that have limited application (e.g., 80/20). However, the study of this fuel blend provides useful chemical kinetic information that helps generalize the results of other more practical mixtures.

Table 1.1: Summary of gas composition used in this study

Category	Source		H_2	CO	CH_4	CO_2	N_2	C_2	C_3
1	High H_2	Range in Field	90 - 100						
		Nominal Fuel	100						
		Alternative Fuel	90			10			
2	Process and Refinery	Range in Field	25 - 55	10	30 - 65	5		0 - 25	0 - 25
		Nominal Fuel	25		50			25	
		Alternative Fuel 1	25		50				25
		Alternative Fuel 2	25		65			10	
		Alternative Fuel 3	55		35			10	
3	Gasified Coal/Petcoke (O_2 Blown)	Range in Field	35 - 40	45 - 50		10 - 15			
		Nominal Fuel	40	50		10			
		No Alternatives							
4	Landfill and Digester Gas	Range in Field			35 - 65	35 - 55	0 - 20		
		Nominal Fuel			50	35	15		
		Alternative Fuel 1			50	50			
		Alternative Fuel 2			50		50		
5	LNG	Range See below			75 - 95			5 - 25	
	Shale Gas	Range See below			82 - 97	2.5		0 - 14	1
	Associated Gas	Range See below			75 - 95			5 - 25	
	LNG/Shale/ Associated Gases	Nominal Fuel			95			5	
		Alternative Fuel 1			90			10	
		Alternative Fuel 2			75			25	
		Alterntative Fuel 3			75				25

This study focuses on the formation of NO_X in LPM combustion devices with an emphasis on the effects of varying fuel composition. Additionally, the effects of

reactor residence time and post-flame combustor temperature are also investigated for a selected set of fuels. An atmospheric pressure jet-stirred reactor (JSR) is the research tool used in this study, and both experimental and modelling results are presented for LPM combustion within this combustor. In addition to the study of emissions, the effect that fuel composition has on the resistance to lean blowout is also investigated.

1.2   Literature Review

A general overview of prior research in the area LPM combustion of gaseous fuel alternatives to natural gas is presented in the following section.

1.2.1 CH_4 mixed with C_2 and C_3 hydrocarbons

Although most LPM combustion research has focused on natural gas, or CH_4 in particular, there has been a fair amount of research conducted on higher molecular weight hydrocarbons such as C_2H_6 and C_3H_8 and mixes of CH_4 with these hydrocarbons. The relative abundance of research is because natural gas blends can contain relatively high concentrations of these components. Flores et al. [1] investigated the influence of high concentrations of C_2H_6 and C_3H_8 in a commercial microturbine, and found that the presence of the higher-hydrocarbons results in a considerable increase in NO_X emissions when the fuels are burned at constant equivalence ratio. Malte et al. [2] used an atmospheric pressure JSR to study OH and NO_X formation from various fuels under LPM combustion at a constant measured flame temperature of 1700 K. Under lean conditions, they found that both C_3H_8 and C_2H_2 produces more NO_X than CH_4 when burned at constant measured flame temperature. Marks et al. [3] studied the effects of adding both C_2H_6 and C_3H_8 to a LPM CH_4 flame in three different industrial boilers operating at atmospheric pressure and found that the addition of these higher hydrocarbons increase NO_X emissions when compared on both constant Wobbe index and thermal loading. Spangelo et al. [4] observed more

than a 50% increase in NO_X emissions switching from CH_4 to C_3H_8 in a partially premixed swirl burner operated at constant thermal loading. Corr et al. [5] studied LPM combustion of both CH_4 and C_2H_4 in a JSR and found that for both fuels the NO_X emissions decrease with increased reactor loading (shorter residence time) and CH_4 combustion produces about 75% of the NO_X that C_2H_4 does when burned at the same measured flame temperature. Littlejohn et al. [6] performed LPM combustion experiments in an atmospheric pressure dump combustor fed with a low-swirl injector (LSI). As opposed to the traditional high-swirl injector (HSI), the LSI does not induce a center recirculation zone [7]. They found that both C_2H_6 and C_3H_8 produce more NO_X than CH_4 at constant adiabatic flame temperature. Lee [8] investigated emissions from the LPM combustion of both prevaporized-liquid and gaseous hydrocarbon fuel alternatives to natural gas and found that NO_X emissions increase linearly with fuel C:H ratio. In a similar study, Rutar et al. [9] investigated the LPM combustion of methanol, methane, ethane, ethene, propane, n-butane, and toluene and report similar results to those obtained by Lee. Thus, the clear trend of the literature is that fuels containing higher molecular weight hydrocarbons tend to produce more NO_X than fuels containing only CH_4. This appears to hold whether the fuels are burned at the same flame temperature, or the same thermal loading.

1.2.2 CH_4 mixed with H_2

In the last couple of decades there has been much interest in the addition of H_2 into CH_4 for use in LPM combustion devices. The work generally focused on experiments at atmospheric pressure where LPM CH_4 flames are mixed with H_2 in order to extend the lean blow out limits. This results in lower temperatures which reduces NO_X emissions [10], [11], [12], [13]. There have been experiments that have attempted to isolate the chemical effect of H_2 addition by holding equivalence ratio, adiabatic flame temperature, or thermal loading constant. Interestingly, the results vary and the trends appear to be dependant on the geometry or operating conditions of the

experiment or simulation.

There are many researchers that have found that H_2 addition into CH_4 has little to no effect on NO_X emissions. Schefer et al. [14] compared the emissions of LPM combustion of pure CH_4 to a mixture composed of 45% H_2/55% CH_4 in a lab scale, high-swirl, dump combustor and found no apparent effect on NO_X emissions when the mixtures both had equal adiabatic flame temperatures. Xie et al. [15] studied NO_X formation in a LPM opposing jet-stirred reactor with minimal heat loss for both pure H_2 and pure CH_4 combustion and found that there is virtually no difference in the NO_X emissions between the two pure fuels when compared at equal measured gas temperature. Ren et al. [16] investigated the effect of mixing CH_4 reforming products into a LPM CH_4 flame in a single-jet stagnation-flow configuration. They found that at constant equivalence ratio, the addition of H_2 caused no change in NO_X emissions moving from 0% H_2 to 25% H_2 mixed into CH_4. Sequiera et al. [17] studied the effect of adding both H_2 and/or CO to a LPM CH_4 flame in an atmospheric dump combustor fed with an LSI, which is similar to the device used by Littlejohn et al. [6]. They found that for a fixed adiabatic flame temperature and air flow rate, the NO_X emissions are insensitive to fuel composition. Morris et al. [18] studied the effects of adding up to 12% H_2 to natural gas in a LPM dry-lox-NO_X (DLN) annular can combustor manufactured by the General Electric Company and found that at constant firing temperature the H_2 addition has no effect on NO_X emissions.

There is research showing that NO_X emissions decrease when H_2 is added to CH_4 and other hydrocarbons in general. Delattin et al. [19] performed experiments in an atmospheric pressure primary zone swirl-stabilized combustor on various LPM fuel mixtures simulating both wet and dry partially reformed natural gas. There are several methods that are used to reform natural gas. Whichever method is employed, the process involves breaking down CH_4 into a fuel blend composed of H_2, CO, and varying concentrations of CO_2. In the study performed by Delattin et al. [19], the dry blends were composed of 20% and 40% H_2, respectively, with the majority of

the remaining fuel composed of CH_4 with small traces of CO and CO_2. They found that the flame area, shape and position of flames mixed with high reformate content are significantly different than for a pure CH_4 flame. In addition, they found that at constant equivalence ratio the reformate mixtures show both lower NO_X and CO emissions. Malte et al. [2] studied the combustion of a 50/50 mixture of H_2 and CO in the same study cited above. They found that the reformate mixture produces less NO_X than all of the hydrocarbon fuels when burned at constant measured flame temperature. Although the effect of mixing H_2 into a LPM C_3H_8 flame is not explored in the current study, there are a handful of past studies that have explored the emissions differences between the two fuels. Anderson [20] looked into the effect of mixing up to 44% H_2 into a LPM C_3H_8 flame stabilized with a flameholder. At constant adiabatic flame temperature it was found that the flames mixed with H_2 produce less NO_X. Engleman et al. [21] burned pure C_3H_8, H_2, and CO premixed in a single jet-stirred reactor and measured the flame temperature. Their data show that the H_2 flame produces considerably less NO_X than the C_3H_8 flame when compared at equal measured temperature. Other researchers running experiments with porous burners have found that the addition of H_2 slightly reduces NO_X emissions when run at constant thermal loading [22] and equivalence ratio [23] and significantly reduces NO_X emissions when run at constant adiabatic flame temperature [24].

There are studies that show NO_X emissions increase when H_2 is added to CH_4. Lee et al. [25] performed lean premixed atmospheric pressure experiments in a model gas turbine combustor manufactured by GE and found that at constant loading (based on the LHV of the fuel), pure H_2 produces more NO_X than pure CH_4. Therkelsen et al. [26] studied the effects of fuel and air premixing and the effect of 0-100% H_2 addition into a LPM CH_4 flame burned in a commercially available gas turbine combustor operated at 4 atm. They found that mixture uniformity has a strong effect on NO_X emissions with higher emissions correlating with poorer premixing. They also found that H_2 addition significantly increases NO_X emissions when run at constant thermal

loading. Daniele et al. [27] burned four different syngas mixtures in LPM mode in a generic, high pressure, turbulent jet combustor. They compare NO_X emissions of a $20\%H_2/20\%CO/60\%CH_4$ mixture to fuels composed of just H_2/CO and $H_2/CO/N_2$. At constant adiabatic flame temperature, the NO_X emissions from the H_2 rich fuels are significantly higher than those produced from the fuel with large CH_4 composition for all pressures that were studied. Cheng et al. [28] studied the effect of mixing up to 100% H_2 into a LPM CH_4 flame fired in an industrial scale dump combustor, fed with an LSI, at pressures between 2 and 8 atm. They found that the NO_X emissions do increase slightly for fuels with increasing H_2 percentage. Beerer [29] studied the NO_X emissions from the LPM combustion of both pure CH_4 and a blend of 10% $CH_4/90\%$ H_2 in flare quarl combustor fed with an LSI at pressures between 3 and 5 atm. He found that the high H_2 blend produced significantly more NO_X than pure CH_4 at constant adiabatic flame temperature for all pressures investigated.

Some researchers have found that the NO_X trend depends on how their experiment or simulation is run. Coppens et al. [30] ran experiments with premixed CH_4 flames mixed with up to 35% H_2 stabilized on a perforated plate burner at atmospheric pressure. For flames at constant equivalence ratio, they found that H_2 addition has little effect on NO_X emissions in the lean regime, while mixes of CH_4/H_2 produce less NO_X while operating in rich mode. Hu et al. [31] numerically studied the effect of 0 to 100% H_2 addition in LPM laminar CH_4/air flames and found the same trends as Coppens et al. Kim et al. [10] studied the effect of H_2 addition into a LPM CH_4 flame in an atmospheric pressure swirl stabilized flame with varying swirl intensity. The addition of H_2 was found to shift the reaction zone upstream causing an increase in the concentration of OH radicals and an increase in NO production at constant adiabatic flame temperature. This effect was found to be the largest at the lowest swirl angle investigated of $30°$; however, as the swirl angle is increased to $60°$ there is no apparent effect of H_2 addition on NO_X formation. Guo et al. [32] numerically studied the effects of H_2 addition in lean counterflow CH_4/air premixed flames using the GRI-Mech 3.0.

They found that for LPM CH_4 flames at constant equivalence ratio, the addition of the reformate gas reduces NO_X emissions near stoichiometric conditions; whereas, the addition of reformate gas increases NO_X emissions at ultra-lean conditions. Griebel et al. [33] have performed experiments in a generic high-pressure combustor operating between 5 and 14 bar with pure CH_4 and 20% H_2 mixed into an LPM CH_4 flame. For very lean equivalence ratios ($\Phi = 0.43$), it was found that there is almost no difference in NO_X emissions between the pure CH_4 and the H_2 mix. They found that at richer conditions ($\Phi = 0.5$) the H_2 mix shows no pressure effect and produces higher NO_X emissions for all pressures investigated. The pure CH_4 flame was found to produce slightly less NO_X as pressure is increased.

Thus, the replacement of CH_4 by H_2 leads to apparently inconsistent results, with NO_X sometimes increasing, sometimes staying nearly constant, and sometimes decreasing. This suggests that other factors may be influencing the NO_X trends.

Among several ways to compare emissions data, many researchers have decided to correlate NO_X emissions with equivalence ratio, adiabatic flame temperature, or thermal loading (based on the LHV), etc. Correlating NO_X emissions to constant adiabatic flame temperature seems to be the most correct because of the high temperature sensitivity of the Zeldovich pathway to NO_X formation. It should also be noted that when an LPM CH_4/H_2 flame is held at constant equivalence ratio and the H_2 content of the fuel is increased, the adiabatic flame temperature of the flame also increases. In fact, for an equivalence ratio of 0.6, a H_2 flame has an adiabatic flame temperature that is more than 150 degrees K hotter than a CH_4 flame.

1.2.3 Landfill Gas

The use of landfill gas in LPM combustion systems is of interest for future gas turbine systems. Landfill gas is the product of the decomposition of municipal waste from landfills. Similar in composition to landfill gas, digester gas is the product of anaerobic digestion of organic material from waste-water treatment plants. The composition

of either gas varies depending on the feedstock; however, landfill gas is primarily composed of CH_4 and CO_2 with up to 15% N_2 and trace contaminants [34]. Qin et al. performed tests in an LPM stagnation flow experiment at atmospheric pressure and found that the addition of CO_2 to a LPM CH_4 flame increases the total NO_X emissions per mass of CH_4 consumed [35]. Some recent research has focussed on the effects of exhaust gas recirculation (EGR), where the oxidant stream is diluted with with products of combustion, namely: CO_2, N_2, H_2O, and O_2 [36], [37], and [38]. Røkke et al. studied the effects of adding diluent to both LPM and diffusion flames at atmospheric pressure. In the LPM mode, they found that mixing was sufficient enough that it did not matter whether the diluent was injected into the fuel or oxidant stream. They also found that the addition of both N_2 and CO_2 decreased NO_X emissions; however, the flame temperature was not held constant [37]. ElKady et al. looked at the addition of 35% EGR to an LPM CH_4 flame at 10 atm and found that the EGR addition decreased NO_X emissions at constant flame temperature [36]. Li et al. studied the effect of varying both EGR percentage and pressure and found that at constant flame temperature, EGR increases NO_X formation at pressures below 5 atm, while EGR reduces NO_X emissions at pressures above 5 atm [38].

1.3 Organization

The dissertation is organized into the following chapters:

- Chapter 2 provides general overview of LPM combustion in industrial gas turbines, and the basic concepts of NO_X formation follows this discussion.

- Chapter 3 presents the experimental setup.

- Chapter 4 discusses the development of a chemical kinetic model that is used to interpret the experimental data.

- In Chapter 5, the major experimental findings as well as modelled interpretation of the data are presented.

- CFD modeling results for LPM H_2, H_2/CO, and CH_4 combustion with NO_X formation are presented in Chapter 6.

- A summary of the results are reported in Chapter 7.

1.4   Research Objectives

The general objectives of our research are summarized below.

1. Experimentally determine the emissions differences between fuel blends and use the numerical tools to quantify, interpret, and develop general mechanistic understandings for the reasons behind the differences in NO_X emissions.

2. Develop modelling tools including CFD and chemical reactor models to accurately characterize the experimental results obtained from the JSR.

3. Extend these tools for use in other industrial and experimental combustors.

4. Use the experimental and modelling results to help develop a set of Gaseous Fuel Interchangeability Criteria or a methodology based on selected fuel properties that can aid both turbine manufacturers and operators to develop and run gas turbines on gaseous fuel alternatives to natural gas.

Chapter 2

BACKGROUND AND REVIEW

2.1   Gas Turbines

Over the past couple of decades, natural gas fired combined cycle combustion turbines
have become a leading technology for new power generation projects. Over this time
period, gas turbine technology has made significant progress. Stringent rules on NO_X
emissions have forced manufacturers to make considerable technological advances.

Gas turbine designs first emerged in the 1930's when it was decided that the piston
engine had reached a technological limit as the engine of choice for aircraft propulsion
[39]. The vast success of gas turbines for aircraft propulsion motivated manufacturers
in both America and Europe to develop similar machines for utility applications in
the 1950's. As opposed to their aircraft counterparts, industrial gas turbines were
designed with less importance placed on weight and size and more emphasis placed
on long, reliable operability, fuel economy, and low emissions [40].

2.2   Oxides of Nitrogen

Oxides of nitrogen (NO_X) is a term used to signify the sum of nitric oxide (NO)
and nitrogen dioxide (NO_2). These two species are easily interchanged in combustion
systems and in the environment, so from a regulatory sense their sum is treated as a
single pollutant.

2.2.1   Formation of NO_X

In order to develop suitable NO_X control methods, the mechanism of NO_X formation
in combustion must be understood. There are five major NO_X formation pathways:

(1) Zeldovich [41], (2) N_2O [42], (3) NNH [43], (4) prompt [44], and (5) the oxidation of fuel bound nitrogen [45]. Since the fuel bound nitrogen pathway is only of concern where fuel-bound nitrogen is present, it will be neglected in the present study because our target fuels are free of bound nitrogen.

Many processes require combustion to occur at temperatures exceeding 1800 K. Zeldovich NO_X becomes the principal NO_X formation route above this critical temperature. The formation of Zeldovich NO_X occurs under high temperature combustion processes via the following three reactions:

$$O + N_2 \Leftrightarrow NO + N \tag{2.1}$$

$$N + O_2 \Leftrightarrow NO + O \tag{2.2}$$

$$N + OH \Leftrightarrow NO + H \tag{2.3}$$

First, an O atom combines with N_2 to form NO and an N atom. The N atom combines with O_2 to produce another NO molecule and an O atom. The third reaction is added because it is an equally important route for N atoms oxidizing to NO molecules. This reaction also produces H radicals which are important for producing more O radicals through the following chain branching reaction.

$$H + O_2 \Leftrightarrow O + OH \tag{2.4}$$

The reaction rate constants are a strong, exponential function of temperature, and above 1800 K this mechanism becomes an important contributor to NO_X emissions from most practical combustion equipment. The Zeldovich reaction mechanism is linked to the combustion chemistry through O_2, OH, and O. If the majority of the NO formation occurs at a sufficiently long enough time after fuel combustion has completed, N_2, O_2, and O concentrations can be assumed to be at equilibrium, and N atoms can be assumed to be in steady state. If it is also assumed that NO concentration is far from equilibrium, i.e. the NO levels remain small as in LPM combustion,

the reverse Zeldovich rates can be neglected and the NO formation rate can be written as in Equation 2.5, where $k_{N1,f}$ is the forward rate constant of Equation 2.1; $[O]_{eq}$ and $[N_2]_{eq}$ are the equilibrium concentrations of O-atom and N_2, respectively [46].

$$\frac{d[NO]}{dt} = 2k_{N1,f}[O]_{eq}[N_2]_{eq} \tag{2.5}$$

The above equilibrium assumption, however, is not valid within turbulent flame zones followed by short residence time post-flame zones as is the case within the experiments carried out in this study, principally due to non-equilibrium radical behavior in active combustion regions [46]. We will show that the simplified NO_X formation rate cannot be applied to NO_X formation within this study, and the other formation pathways are equally important both due to the low temperature combustion studied (below 1800 K) and the super-equilibrium radical concentrations.

The nitrous oxide mechanism was originally proposed by Malte and Pratt [42] to explain NO_X formation in high-intensity, lean, premixed combustion. N_2O produces NO as shown in Equations 2.6 through 2.11.

$$N_2 + O + M \Leftrightarrow N_2O + M \tag{2.6}$$

$$N_2O + O \Leftrightarrow N_2 + O_2 \tag{2.7}$$

$$N_2O + O \Leftrightarrow NO + NO \tag{2.8}$$

$$N_2O + H \Leftrightarrow N_2 + OH \tag{2.9}$$

$$N_2O + OH \Leftrightarrow N_2 + HO_2 \tag{2.10}$$

$$N_2O + H \Leftrightarrow NO + NH \tag{2.11}$$
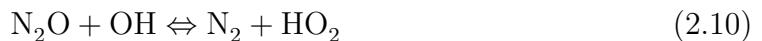
N_2O is principally formed by Equation 2.6, while NO is mainly formed from Equations 2.8 and 2.11.

The NNH pathway has been proposed by Bozzelli and Dean, which is composed of the following two main reactions shown in Equations 2.12 and 2.13.

$$N_2 + H + M \Leftrightarrow NNH + M \tag{2.12}$$

$$NNH + O \Leftrightarrow NH + NO \tag{2.13}$$

The NNH molecule is mainly produced by Equation 2.12, which is thought to be close to equilibrium within the flame zone [43], and NO is formed through Equation 2.13.

The last pathway for NO_X formation was proposed by Fenimore in 1971 [44]. Known as the Fenimore or prompt mechanism, this pathway relies on the reaction of N_2 with hydrocarbon radicals, CH_i. The principal reaction initiating the pathway is shown in Equation 2.14.

$$CH + N_2 \Leftrightarrow HCN + N \tag{2.14}$$

The HCN and N-atom produced by this reaction are believed to quickly oxidize to NO; however, under ceratin conditions some of the HCN and N goes back to N_2.

2.2.2 Available NO_X Control Technologies

NO_X emissions regulations are becoming more stringent as we move into the future. As of 2006, the United States EPA has issued the emissions standards for electricity producing land based gas turbines outlined in Table 2.1 [40].

Table 2.1: Summary of US EPA NO_X emissions standards for electricity producing gas turbines from 2006.

Fuel	Size (MW)	NO_X emissions (ppmv, corrected to 15% O_2, dry)
Natural Gas	Under 3	42
	3 - 110	25
	above 110	15
Fuel Alternatives to Natural Gas	Under 3	96
	3 - 110	74
	above 110	42

In addition to the federal standards shown above, many local governments such as the SCAQMD in California have opted to impose NO_X emissions standards as low

as 0.07 lbm/MWhr [47]. Assuming a thermal efficiency of 57% and CH_4 combustion, this corresponds to about 2.2 ppm corrected to 15% O_2. In many local governments there is a requirement to use the best available control technology, requiring power plant operators to follow the state of the art technology [40]. Currently, the main NO_X control technologies are the following:

- Water or steam injection

- Selective Catalytic Reduction

- Staged Combustion

- Lean premixed combustion

In water/steam injection, water or steam is introduced into the primary combustion zone. This reduces the flame temperature and causes up to an 80% decrease in NO_X formation [48]. Steam injection can negatively impact gas turbine performance by causing pressure fluctuations. In addition to performance issues, a water/steam injection system can add significant capital cost and increase fuel consumption [49]. The last major drawback to this technology is that while reducing NO_X emissions, water/steam injection can give rise to significant increases in the emissions of CO and unburned hydrocarbons (UHC), occurring mainly at part load [40].

The main post-combustion technology for NO_X control is selective catalytic reduction (SCR). In SCR, NO_X is reduced to N_2 by injecting ammonia into the exhaust stream over a narrow temperature range in the presence of a catalyst. Due to the required narrow temperature range, SCR is best suited to be used in combined cycle/cogeneration systems that are equipped with heat recovery systems. These systems are quite bulky and costly; thus they are generally not used in simple-cycle applications.

Another major NO_X control strategy employed is staged combustion in which the combustion takes place in a succession of combustion regimes that are typically rich-lean. Variable geometry combustors are used in this technology and successful NO_X control is dependant on rapid mixing between stages [46].

In premixed combustion, the air and fuel are combined prior to the combustion zone. This provides an overall improved homogeneity of the air fuel mixture, thus leading to a higher combustion efficiency. The implementation of fuel and air pre-mixing along with lean operation results in a significant lowering of the combustion temperature in the dome region of the can combustor. One drawback to implement-ing this technology is that the stoichiometry needed for low NO_X emissions nearly coincides with the weak extinction limit for most hydrocarbon fuels. Fortunately, this problem can be remedied through the use of fuel staging, variable geometry, etc. which can provide control over the primary zone air flow so as to maintain a proper air/fuel ratio to prevent flame blowout. The process of employing fuel-staged, lean premixed combustion is known as the dry low NO_X (DLN) technique. In the past few decades, DLN combustors have been widely used by Solar, General Electric, Al-stom, Siemens, and Rolls Royce to achieve reliable single digit NO_X emissions when operated on natural gas [40].

The optimal NO_X control method is one that does not significantly reduce system efficiency, curtails emissions , and can be applied to older units without requiring a significant amount of new hardware. In the past couple of years, DLN technology has become the most popular method of control; however, lean premixed operation is associated with lean blowout and acoustic instability problems. Although the indus-trial gas turbines of the past employing diffusion flame technology were able to burn a wide variety of fuels with varying flame speeds and heating values, new gas turbines employing DLN technology have been primarily run on natural gas. The uncertainty of future natural gas supply, and the availability of other fuels, has greatly increased interest in using alternatives to natural gas in lean premixed DLN technology. As be-

fore mentioned, it is the goal of this study to determine the consequences in regards to emissions and lean blowout limits associated with using alternatives to natural gas in DLN gas turbines.

Chapter 3

JSR OVERVIEW AND DIAGNOSTICS

The well-stirred reactor (WSR) has been used since the mid 20th century to study many aspects of premixed turbulent combustion including global reaction rates, pollutant formation, and turbulent flame stability near blowout [46]. WSR designs have been constructed in many different ways from a single jet impinging on a truncated cone to dozens of jets emerging from the center of a sphere. The basic idea is to have mixing occur as fast as possible. While the WSR is known as an experimental device, the idealized model is referred to as the perfectly-stirred reactor (PSR). The basic concept behind the PSR is that premixed fuel and air flow into a fixed volume at constant pressure and are instantaneously mixed with the combustion products. The reaction that occurs achieves a steady state combustion temperature and the mass flow leaving the reactor maintains this reaction temperature as well as the species concentrations associated with the homogenous reactor volume [45]. That is, the PSR is uniform in temperature and species concentrations. While the WSR attempts to achieve this homogeneity, there are typically two or more combustion regimes within the experimental device that are associated with the inlet reactant stream.

Throughout the years, many researchers have built experimental well-stirred reactors in hopes of approaching the ideal PSR. Longwell and Weiss were among the first to build such a reactor in which they studied reaction rates of hydrocarbon fuels near blowout [50]. Their design incorporated a spherical reactor body with the premixed fuel and air being injected in the center of the body through a perforated ball. In the 70's Pratt and Malte studied NO_X formation in a single-jet stirred reactor burning premixed CO and air [42]. In the 90's Zelina and Ballal constructed an experimental

PSR that is toroidal in geometry in which the premixed reactants enter through 32 jets on the outer surface of the toroid [51]. In the late 1980's Thornton et al. developed a single-jet stirred reactor that employs a cavity in the shape of a truncated cone [52]. This WSR geometry is what many UW researchers have been using to study LPM combustion kinetics from the early 90's through today. The reactor currently used in this study is of this same geometry and was constructed out of high purity Greencast alumina by Lee [8].

3.1 Experimental Overview

All of the experimental data are obtained from a high intensity, backmixed, single-jet, stirred reactor shown in Figure 3.1. Both fuel and air enter the reactor through the
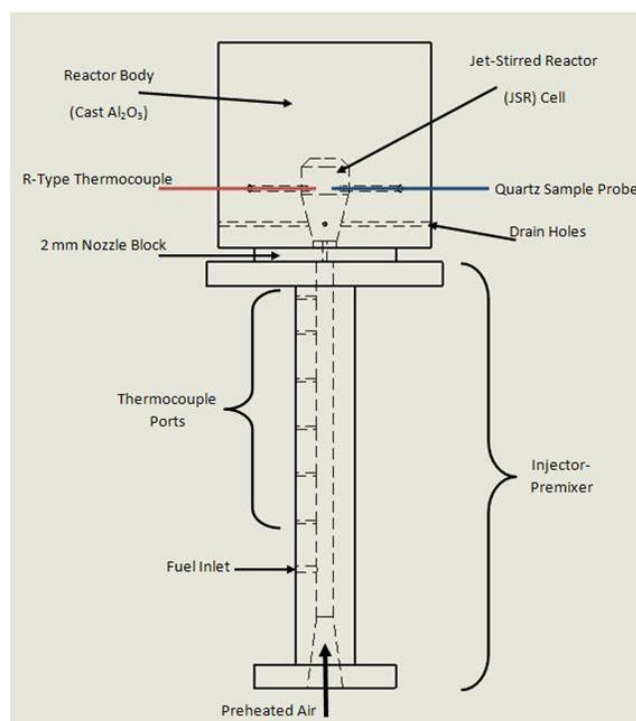
Figure 3.1: Diagram of Experimental Setup

premixer. The air is preheated to 573 K. Neglecting back heating from the reactor

cavity, the fuel and air mixture has a nominal temperature of about 550 K as it enters the reactor cavity. The stagnation pressure of the premixed fuel/air mixture is measured 5 cm upstream of the reactor cavity and is typically about 21 psig. The premixed reactants enter the cast alumina reactor cavity through a 2mm nozzle resulting in a sonic jet velocity of approximately 450 m/s. The total volume of the reactor is 15.8 cc, the mass flow rate of air is 1.08E-3 kg/s, and nominal combustion temperature is held constant at 1800 K. This results in a mean fluid residence time of 2.7 ± 0.3 ms.

As shown in Figure 3.2, both temperature and species concentrations are measured at 2/3's of the reactor height with the nominal sampling location being 2 mm inside the reactor wall. This sampling location is far enough into the reactor to avoid thermal and fluid boundary layer effects, but not so far as to experience the effects of the jet. In addition to collecting data at the standard sampling location, detailed reactor spatial probing is conducted in order to gain insight of flame structure within the reactor. Both temperature and species measurements are taken radially between the reactor wall and centerline at 2/3's of the total reactor height.
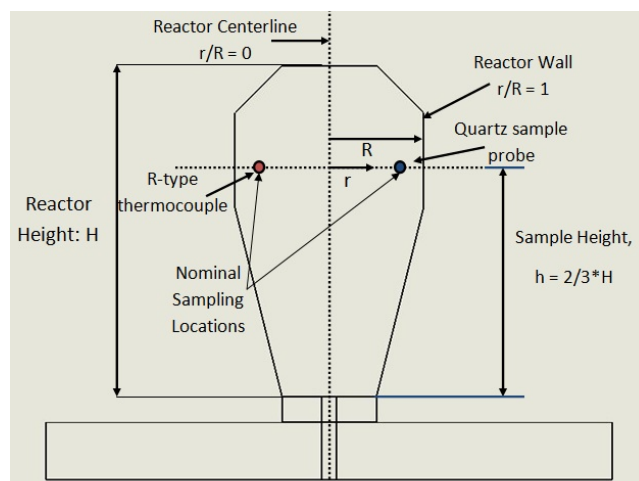
Figure 3.2: Sampling locations within the JSR

The combustion gas temperature is measured with a type R thermocouple that is coated with alumina to prevent catalytic effects. The measured temperature on the coated thermocouple bead is affected by a balance between convection from the hot gases to the bead and loses from the bead radiating to the colder reactor wall and conduction through the thermocouple wires as shown in Equation 3.1.

$$Q_{conv} = Q_{rad} + Q_{cond} \tag{3.1}$$

Other researchers have shown that using sufficiently thin thermocouple wire reduces the conduction to a negligible amount [8], [53].

Neglecting conduction in the wire, the measured combustion temperature is between 50 and 70 K below the reported temperature which is obtained by correcting the measured thermocouple temperature for radiation to the colder reactor wall [54]. The hot combustion gases are sampled through a warm water cooled, quartz sample probe. The sample gas is drawn by a metal bellows pump into a heated teflon tube (to prevent condensation). The sample is then drawn through an ice bath where the H_2O in the sample is removed and the dried gas is sent to a three gas (CO_2, CO, and O_2) analyzer and a NO_X analyzer (Thermo Electron Model 10) in parallel. The CO_2 and CO analyzers operate on the NDIR principle, while the O_2 and NO_X analyzers are paramagnetic and chemiluminescent instruments, respectively.

3.2   Heat Transfer through the JSR

In order to properly model the NO_X data and compare it to data obtained from other fuels at various equivalence ratios, the true gas temperature must be measured. As mentioned above, the thermocouple loses heat both due to radiation to the colder reactor wall and to conduction along the wires. In order to properly correct the temperature read by the thermocouple, the temperature of the inside reactor wall must be known with a reasonable degree of certainty.

Several experimental researchers at the UW have reported some degree of heat

loss from various jet-stirred reactors for both atmospheric ([54], [8]), and high-pressure ([54], [55]) JSR experiments. In general, the high pressure experiments were found to be more adiabatic than the atmospheric pressure tests; however, all experiments showed that the heat loss is minimized when the mass flow rate through the reactor is increased. A larger mass flow rate decreases the overall reactor residence time as given in Equation 3.2, where τ is the reactor residence time, ρ is the density of the fluid in within the reactor based on the combustion temperature and pressure, V is the reactor volume, and $\dot{m}$ is the total mass flow rate through the reactor.

$$\tau = \frac{\rho V}{\dot{m}} \tag{3.2}$$

Since the present study is concerned with the differences between a variety of fuels, the goal is to keep variations in residence time to a minimum to help remove this parameter since it does have a mild effect on emissions [54]. With the exception of the experiments investigating the effect of residence time, the air flow rate is kept constant at 1.08E-3 kg/s for all constant temperature experiments (1800 K) for every fuel tested. For the blowout tests, the air flow rate is also set constant at 1.08E-3 kg/s. However, due to differences in blowout temperature (e.g. H_2 vs. CH_4), the residence time is larger due to an inherent increase in density when the reactor is colder.

Past JSR researchers have used an optical pyrometer to measure the reactor wall temperature. In the work by Shuman, for a measured thermocouple temperature of 1813 K, the measure wall temperatures ranges from 1030 to 1220°C [55]. Lee reports a typical measured wall temperature of 1602 K [8]. Steele reports a measured wall temperature of 1563 K for the atmospheric tests conducted in his work [54]. Although all three experimentalists measured the wall temperature in order to properly correct their thermocouple measurements, none of them attempted to quantify the actual heat loss from the reactor.

The heat loss in the present reactor is quantified by two methods. In the first proceedure, a First Law balance is performed on the JSR by taking the difference

between the enthalpy of the premixed reactants coming into the reactor and that of the hot combustion products leaving the reactor as shown in Equations 3.3 and 3.4. The estimated heat loss from the first law balance is 440.6 W, which is about 20% of the incoming energy based on the LHV of the fuel. The inputs and outputs of the analysis are shown in Table 3.1.

$$Q_{out} = \sum N_r(h_f^\circ + \bar{h} - \bar{h}^\circ)_r - N_p(h_f^\circ + \bar{h} - \bar{h}^\circ)_p \tag{3.3}$$

$$q_{out} = \frac{Q_{out}\dot{m}_{CH_4}}{M_{CH_4}} \tag{3.4}$$

where,

- Q_{out} is the heat loss from the reactor (kJ/kmol$_{CH_4}$)

- N_r and N_p are the mole numbers of each species for reactants and products, respectively (kmoles)

- h_f° is the enthalpy of formation (kJ/kmole)

- $\bar{h}$ is the enthalpy of each species at elevated temperature in kJ/kmole

- $\bar{h}^\circ$ is the enthalpy of each species at 298 K (kJ/kmole)

- q_{out} is the reactor rate of heat loss (W)

- $\dot{m}_{CH_4}$ is the mass flow rate of CH$_4$ (kg/s)

- M_{CH_4} is the molecular weight of CH$_4$ (kg/kmole)

The second approach to quantifying reactor heat loss involves a simple one dimensional heat transfer model. As shown in Figure 3.3, heat is transferred to the reactor wall from the gas via convection and radiation. The convective heat transfer coefficient is estimated as 200 W/m^2-K from using boundary layer theory analysis of

Table 3.1: Inputs and results from first law balance on the reactor

Input parameters	Output parameters	q_{out} (W)
$T_{preheat} = 571$ K	$T_{gas} = 1800$ K	
$\dot{m}_{CH_4} = 4.62\text{e-}5$ kg/s	$y_{O_2} = 0.068$	440.6
$\phi = 0.718$	$y_{CO_2} = 0.079$	
	$y_{CO} = 0.00242$	

flow around a body of revolution as outlined in Kays et al. [56]. The radiation to the reactor wall is quite insignificant due to the small mean beam length (0.017 m) calculated for the JSR. The emissivity of the combustion products is determined as 0.009 from the charts in Incropera et al. [57], and 0.012 from a more refined algorithm presented by Modest [58]. For the remainder of this analysis, the gaseous radiation to the wall is neglected. The heat convected to the wall is then transferred through the reactor wall by conduction. The radiative losses through the exhaust ports and feed jet are assumed to be negligible due to the small area that these holes encompass. The conduction resistance is modelled as two concentric spheres as given by Equation 3.5.
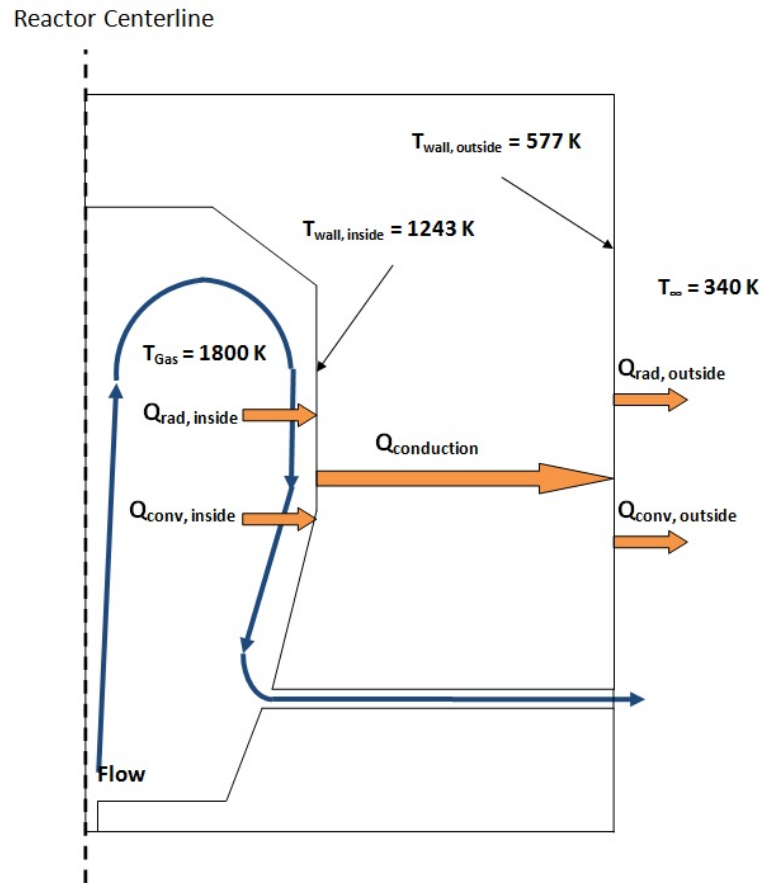
Figure 3.3: Diagram illustrating the modes of heat transfer out of the JSR

$$R_{\text{Conduction}} = \frac{(1/r_1) - (1/r_2)}{4\pi k} \tag{3.5}$$

where,

- $R_{\text{Conduction}}$ is the conduction resistance (K/W)

- r_1 and r_2 are the inside and outside radii, respectively (m)

- k is the thermal conductivity of the castable alumina (W/m-K) [59] (average k for calculated wall temperatures is 2.3 W/m-K)

The heat then is transferred to the ambient environment through natural convection and radiation. The temperature of the ambient environment is that of the plenum where the reactor exhausts. The one dimensional thermal circuit used in this analysis is shown in Figure 3.4. Note that the temperature of the gas and that of the ambient environment are measured; whereas the the inside and outside wall temperatures are calculated.
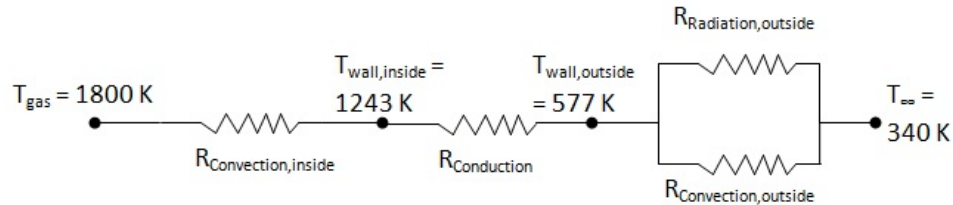
Figure 3.4: One dimensional thermal circuit for the JSR

The total reactor heat loss calculated from this analysis is found to be 422 W, which is remarkably close to the heat loss calculated from the first law analysis shown above. A summary of the results are shown in Table 3.2.

Table 3.2: Measured and Calculated temperatures, thermal resistances, and heat loss from the thermal model illustrated by Figures 3.3 and 3.4

Measured Temperatures	Calculated Temperatures	Thermal Resistances (W/K)	q_{out} (W)
$T_{gas} = 1800$ K	$T_{wall,inside} = 1243$ K	$R_{convection,inside} = 1.32$	
$T_{\infty} = 340$ K	$T_{wall,outside} = 577$ K	$R_{conduction} = 1.58$	422
$T_{wall,outside} = 563$ K		$R_{conv/rad,outside} = 0.56$	

There are a couple of points that should be made about this one dimensional heat transfer analysis. Each one of the thermal resistances is of the same order of magnitude; thus there is no clear mode of heat transfer to focus on improvement. This

being said, the reactor is run at the current flow rates to promote fast mixing and approach well-stirred condition. Decreasing the flow rates through the reactor will certainly increase the convective resistance on the inside wall of the reactor; however, this is not advised since mixing will be compromised. Constructing the reactor body out of a material with a lower thermal conductivity will increase the conductive resistance of the reactor. Increasing the outside dimensions of the reactor will augment the conduction resistance; however, the increase in outside surface area reduces the convection/radiation resistance on the outside of the reactor at a quicker rate. It seems that constructing the reactor out of a material with a lower thermal conductivity or adding insulation to the outside (although this will also increase surface area) is the best method of making the reactor operate in a more adiabatic manner. Most of the materials that will tolerate these temperatures have a fairly large k. This is why layered designs are often used.

The second and third points to make is that the calculated and measured surface temperatures on the outside of the reactor are in good agreement ($T_{meas,avg} = 563K, T_{meas,avg} = 577K$, while the inside wall temperature is a couple hundred degrees lower than what other JSR researchers have measured. This is a source of concern since it will add about 30 K to the calculated gas temperature. It is assumed that the relatively cold calculated wall temperature is an effect associated with the simple one dimensional model. For the chemical modelling results shown in Chapter 5 it is assumed that the inside wall of the reactor is 1500 K, which gives a nominal corrected gas temperature of 1800 K. This wall temperature is the median temperature between the measured results of past researchers and the results computed by CFD. This is discussed further in Appendix C.

Chapter 4

CHEMICAL REACTOR NETWORK DEVELOPMENT

As mentioned in Chapter 1, the Chemical Reactor Network (CRN) for the JSR used in this study is developed using insight from detailed spatial measurements of the reactor, the results of CFD simulations with simplified chemistry, and classical fluid dynamic correlations. In this chapter, a general overview of the CFD simulations with simplified chemistry is presented with an emphasis placed on their aid in the development of the CRN. While CFD simulations are able to provide a detailed solution of the actual flow-field within the JSR, incorporation of complex chemical mechanisms into the model is limited due to a huge increase in computational expense.

CFD simulations are run in both two and three dimensions. The computational grid, the heat transfer, and the turbulence models used for both the two and three dimensional simulations are first presented. Next, the three dimensional CFD results from LPM CH_4 combustion employing a simplified global mechanism are shown. Finally, the results of this simulation are used to construct a CRN.

4.1 Grid, Fluid Dynamics and Heat Transfer Models

For both the two and three dimensional CFD models a structured hexagonal grid is generated encompassing both the solid and fluid portions of the JSR. For the 3D model, one quarter of the physical domain is modeled. In 2D model, the domain is modeled as axisymmetric. The fluid dynamic and heat transfer models are the same for both the two and three dimensional models.

4.1.1   Grid

The three dimensional CFD simulations are conducted with a structured domain of about 1,000,000 cells encompassing both the solid and fluid portion of the JSR. It is necessary to model the solid portion of the domain in order to properly incorporate heat transfer from the reactor. The grid and a blow up of the reactor region for the three-dimensional model are shown in Figure 4.1.
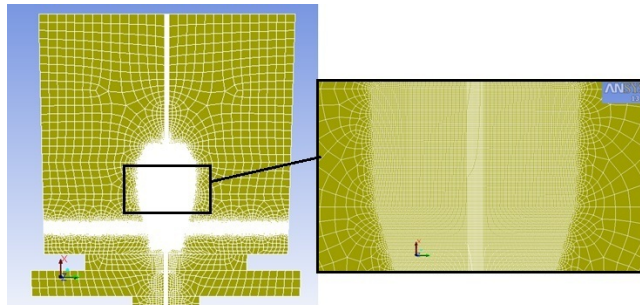
Figure 4.1: Grid used in Three Dimensional CFD simulations

Use of a structured hexagonal domain is necessary to avoid convergence issues. The refined portion of the grid is concentrated within the combustion chamber and has a nominal cell length of 0.158 mm. Approximately, 71% of the cells in the entire domain are fluid cells with the remainder composed of solid cells. Optimally, the number of solid cells would be smaller; however, the solid cells on the combustor boundary are the same size as the adjacent fluid cells within the boundary layer. The size of the solid cells increase as the outside wall of the combustor is approached.

The two dimensional CFD simulations are conducted with a structured domain of about 36,000 cells encompassing both the solid and fluid portion of the JSR as shown in Figure 4.2. Similar to the three dimensional grid, about 70% of the domain is made up of fluid cells; however, in the refined portion of the combustion chamber the nominal cell length is about 0.065 mm.
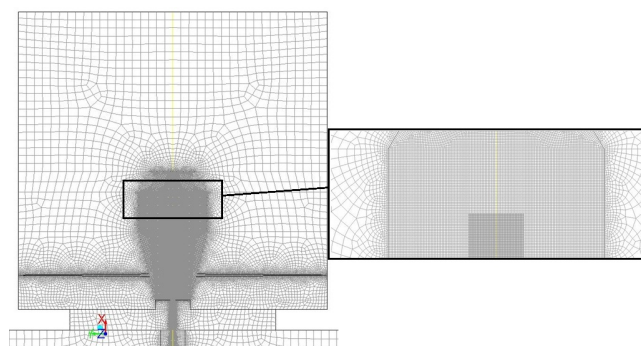
Figure 4.2: Grid used in Two Dimensional CFD simulations

4.1.2   Fluid Dynamics and Heat Transfer Models

The flow of reactants going through the nozzle block is choked; thus the density within the fluid portion of the domain is modeled with the ideal gas equation. Velocity and mass flow inlets can only be applied to simulations involving incompressible flow. Since the flow within the JSR nozzle is compressible, the before mentioned boundary conditions will not converge. Instead, the inlet and outlet are set as pressure boundaries. The correct stagnation properties are set for both boundaries and the model will adjust the mass flow rate through the reactor. For both the two and three dimensional simulations the upstream stagnation properties are set at the measured stagnation pressure and temperature which are approximately 21 psig and 550 K as mentioned above. The outlet pressure and temperature for the three dimensional simulation are set to 0 psig and 2000 K.

There are some difficulties associated with the outlets for the 2D axisymmetric model. The drain holes are represented by a single slot. Optimally, the area of the slot would be equivalent to the area encompassed by the four drain holes. This causes the height of the slot at the combustor exit to be quite small. The height of the slot is then increased to avoid the numerical difficulties; however this increase causes too small of a pressure drop resulting in erroneous fluid dynamics within the combustion

chamber. In order to correctly predict the fluid dynamics within the combustion chamber the outlet pressure is increased from 0 approximately 4.4 psig [60]. The temperature is set the same as in the 3D model. For all modeled conditions, the mass flow rate difference between the model and experiment is less than 1%.

Due to the recirculating nature of the flow within the combustion chamber, model convergence was not attainable for either the standard [61] or realizable [62] k-ε models. Instead, the Reynolds stress model [63] is employed due to its inherent ability to handle the highly recirculating nature of the flow inside the JSR.

A multidimensional heat transfer model is utilized that accounts for convection on both the inner and outer surfaces of the JSR, conduction throughout the entire domain, and radiation on both the inner and outer surface of the JSR. The radiation on the inner surface is modelled using the Discrete Ordinates Model [64], while the radiation on the outer surface is modelled as the actual ceramic surface with a temperature dependant emissivity (nominal emissivity is 0.67) and a view factor equal to unity. The partial differential equations that govern both flow and heat transfer within the JSR are solved using the ANSYS Fluent software package [65].

4.2 CFD Modelling for CRN Development

To aid in the development of the CRN, a simple 3 step global chemistry mechanism is used to model LPM CH_4 combustion [66]. The simplified chemistry within the reactor is modelled with the Finite Rate/Eddy-Dissipation model [67]. In this model, the reaction rate is computed by both an Arrhenius expression and an expression that incorporates turbulent effects. The turbulent mixing, or eddy-dissipation reaction rate is governed by the the large eddy mixing time scale: k/ε, while the chemical rate is generally governed by one or two global reaction steps [65]. The reaction steps and rates are shown below in Table 4.1. The net reaction rate is computed as the smaller of the two rates.

The global chemistry does a reasonably good job of predicting CH_4 and CO ox-

Table 4.1: Reaction steps and global rates for the CH_4 oxidation mechanism developed by Nicol. Units are: kmoles, m^3, and K.

Reaction	Rate
$CH_4 + \frac{3}{2}O_2 \rightarrow CO + 2H_2O$	$R_1 = 10^{15.220}[CH_4]^{1.460}[O_2]^{0.5217}\exp^{-20643/T}$
$CO + \frac{1}{2}O_2 \rightarrow CO_2$	$R_2 = 10^{14.902}[CO]^{1.6904}[O_2]^{1.570}\exp^{-11613/T}$
$CO_2 \rightarrow CO + \frac{1}{2}O_2$	$R_3 = 10^{14.349}[CO_2]^{1.0}\exp^{-62281/T}$

idation as shown in Figures 4.3 and 4.4. The contours of temperature and CO concentration are shown in Figure 4.5.
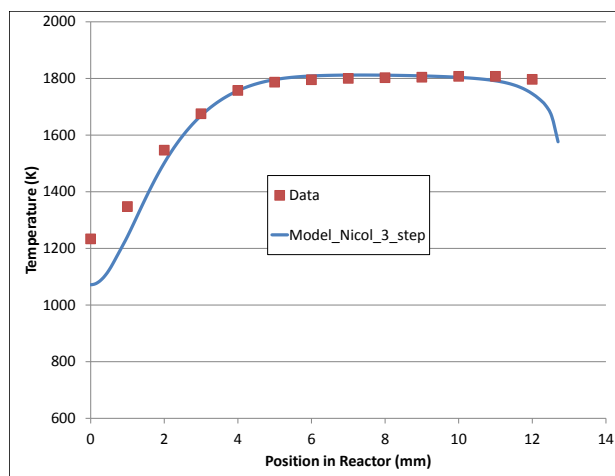
Figure 4.3: Profile of temperature from reactor centerline to wall, measured and predicted by CFD for CH_4 combustion for exit gas O_2 of 6.6% (mole %, dry)

Figure 4.5 illustrates the two zone combustion behavior of the JSR. The highly turbulent flame zone is anchored around the nozzle, which is outlined by the region of high CO concentration. This flame zone is then followed by a super-equilibrium post flame recirculation zone, where the radicals (indicated by CO concentration) are starting to relax and the temperature is fairly uniform at about 1800 K. Although this CFD model does not predict radicals and NO_X, the CO contours and flow field can be used as guidelines to develop a chemical reactor network (CRN), which can
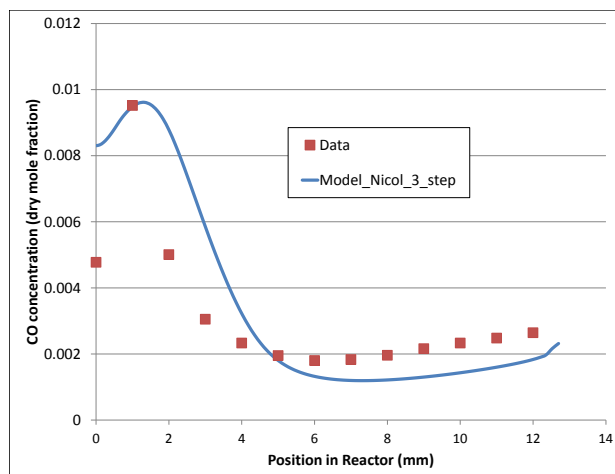
Figure 4.4: Profile of CO from reactor centerline to wall, measured and predicted by CFD for CH_4 combustion for exit gas O_2 of 6.6% (mole %, dry)

(a) CO concentration (mole fraction)
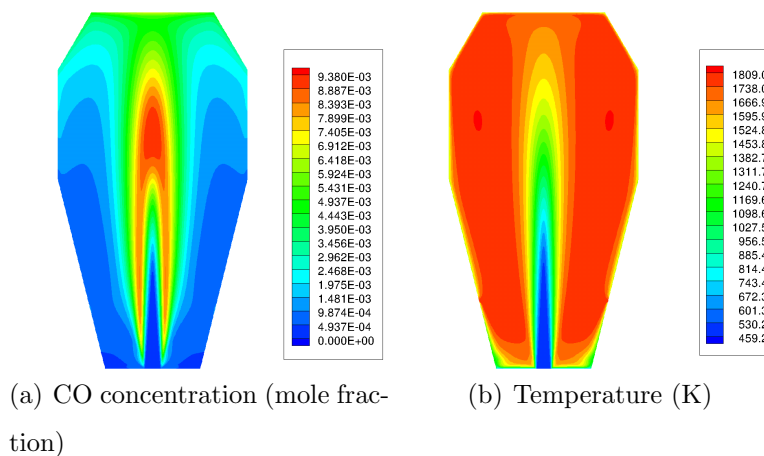
(b) Temperature (K)

Figure 4.5: CO and temperature contours by CFD for JSR fired on CH_4 computed by global chemistry. The nominal recirculation zone temperature is 1800 K.

incorporate detailed chemistry.

Finally, the flowfield computed by CFD is analyzed to determine the location and strength of recirculation zones. Shown in Figure 4.6 are the contours of the stream function within the JSR. Note the strongly recirculating flow in the upper portion of

the reactor to either side of the jet.
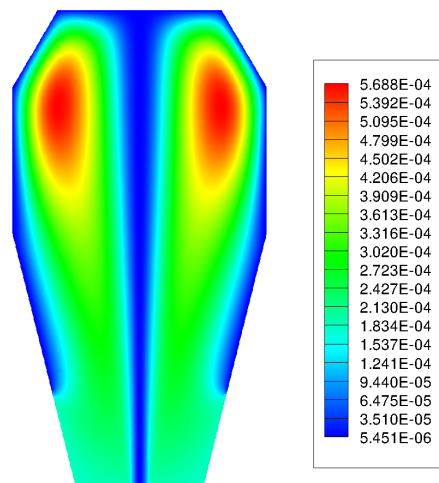
Figure 4.6: Contours of stream function within the JSR (kg/s).

4.3 Development of the CRN

The CFD model is used as a basis to construct a chemical reactor network composed of perfectly stirred reactors (PSR) as shown in Figure 4.7.
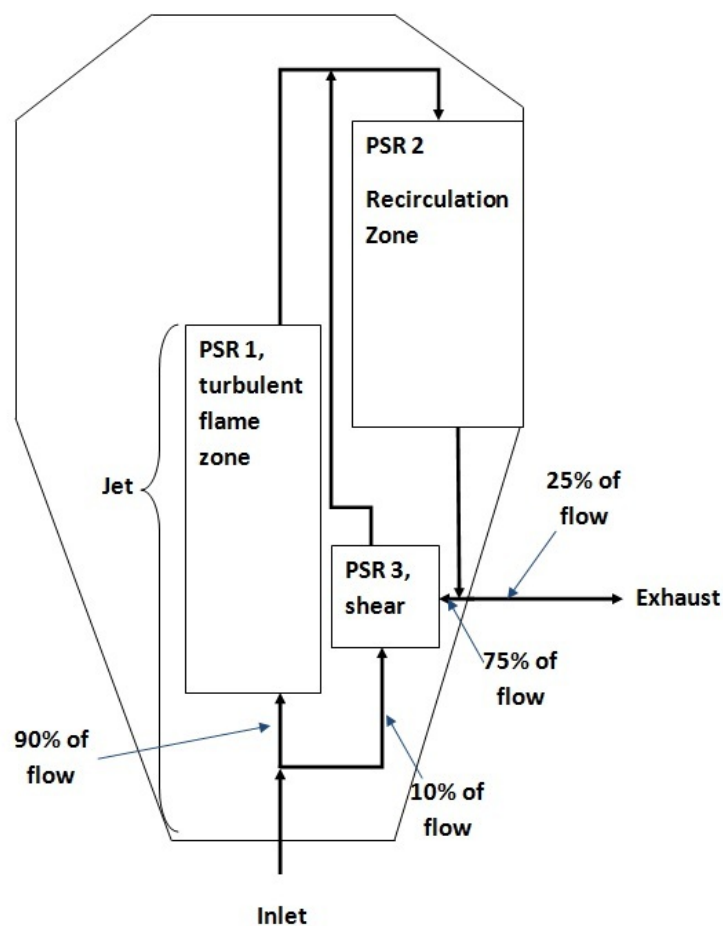
Figure 4.7: Chemical Reactor Network constructed from the calculated flow field within the CFD model

The first element, PSR 1, represents the turbulent flame brush that does not see any entrainment from the recirculation zone. It is modelled as a PSR at blowout, which is an adiabatic PSR that is 1% larger than the smallest volume that will sustain combustion with the given inlet conditions. Using the results of the CFD model and following a procedure developed by Novosselov [68], it is found that approximately 90% of the flow leaving the jet passes through PSR 1. About 10% of the flow proceeds through the side of the jet and mixes with hot gases coming from the recirculation zone. Denoted as PSR 3, or shear zone, this reactor is representative of

a turbulent premixed strained flame, where cold reactants strain against hot recircu-
lated products. PSR 3 is also adiabatic since it does not come into contact with the
outside wall. Its volume is estimated to be about half of the volume computed for
PSR 1 from the CFD simulation. The contents of both PSR 1 and PSR 3 continue
into PSR 2, which represents the recirculation zone within the JSR. PSR 2 is assigned
the remaining reactor volume (most of the JSR volume) and is run at the measured
temperature of 1800 K. For LPM CH_4 combustion at a nominal recirculation zone
temperature of 1800 K, the volumes of the turbulent flame brush, recirculation zone,
and shear zone, are 0.36 cc, 15.3 cc, and 0.18 cc, respectively. The CFD model is again
consulted to choose the flow fraction that is being exhausted rather than sent back to
the recirculation zone. At several axial locations along the height of the reactor, the
downward mass flow is integrated. For reference, three of the velocity profiles used in
the integration are shown in Figure 4.8.
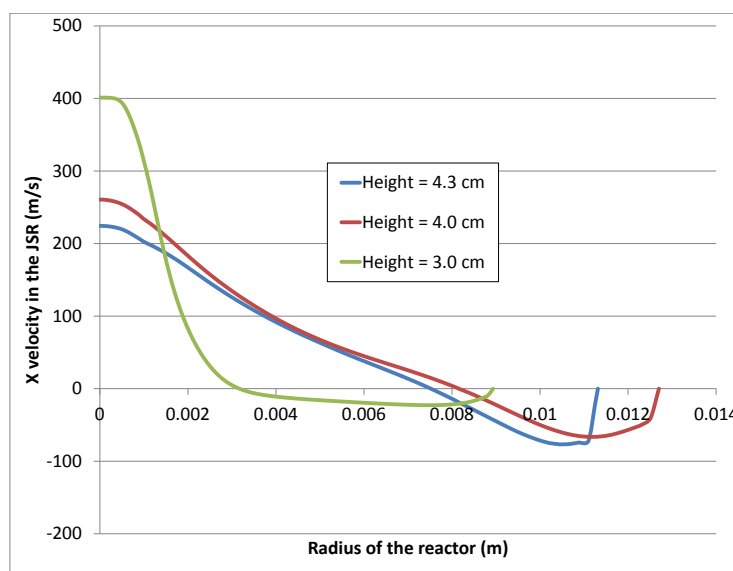
Figure 4.8: Axial velocity profiles for three locations along the height of the reactor

The positive velocity shown is characteristic of fluid travelling in the same direction

as the jet, and the negative velocity corresponds to fluid travelling towards the drain holes (this is the flow that is integrated as mentioned above). By subtracting this mass flow from the known mass flow leaving the reactor (mass conservation), one obtains an estimate for the mass flow that is returning to the recirculation zone through PSR 3. This calculation finds that approximately 75% of the flow returns to the recirculation zone, while 25% is exhausted. This flow fraction is verified by using the particle tracking feature within the software [65]. With this flow network established, it is now possible to calculate mixing-influenced states using detailed chemistry in the CRN.

Chapter 5

EXPERIMENTAL AND CRN MODELING RESULTS

The experimental data presentation is divided into seven sections:

1. The first section deals with issues associated with pollutant oxidation in the sample probe.

2. Detailed reactor scans are presented for the fuel compositions outlined in Table 1.1.

3. The effects of residence time and combustor temperature are investigated for a selected set of pure fuels.

4. The effect that fuel composition has on the resistance to lean blowout is presented.

5. Available chemical mechanisms with NO_X formation are identified and tested against emissions data from LPM CH_4 combustion.

6. The CRN modeling of LPM CH_4 combustion from 1700 - 1800 K is analyzed.

7. Parameterized studies that investigate sequential composition changes within each fuel category are presented.

8. Comments are made about NO_X entitlement based on our experimental data and the results of modeling.

5.1 Sample Probe Effects

There is some question about the accuracy of the measured CO data collected during the experiments. Specifically, we are concerned about the extent of CO oxidation within the probe after the sample has been removed from the reactor. As before mentioned, there are super-equilibrium levels of H, O, and OH within both the turbulent flame brush and the post flame zone. When the combustion gases are sampled, the initial CO in the sample begins to oxidize to CO_2 via the reaction: $CO + OH \rightarrow CO_2 + H$. Steele found that the amount of CO that is oxidized in the sample probe is in proportion to its concentration in the reactor; thus, more CO in the combustion products results in greater conversion to CO_2 [54]. He investigated the chemistry and gas dynamics within the probe using the chemical code GEPROB written by Pratt et al. [69], and found that for LPM CH_4 combustion at atmospheric pressure and a nominal combustion temperature of 1800 K in the recirculation zone, approximately 62% of the CO oxidizes to CO_2 within the sample probe [54]. All of the experimental CO results shown in this chapter are reported as measured, dry, actual O_2.

In addition to CO oxidation in the probe, various researchers have reported that almost all of the NO sampled in the reactor converts to NO_2 by the time it is measured by the analyzer via the reaction: $NO + HO_2 \rightarrow NO_2 + OH$ [54], [70]. This would not be a major concern since all of the NO_2 is converted to NO at the analyzer; however, NO_2 is water soluble and can be lost in the water knockout trap and to condensation in the sample lines. Shuman investigated the possible loss of NO_2 in the sample line by placing an NO_X-to-NO converter in series. The results showed that there was not a significant difference in the measured NO_X concentrations with and without the converter [55]. Although the tests performed by Shuman were at 3 atm instead of 1 atm, it is assumed that the same results apply to the present atmospheric pressure JSR since the sample system pressures are similar; thus, no appreciable NO_X is lost in the sample system. For all testing, the sample lines are maintained above the dew

point with electrical heating tape.

5.2 Reactor Scans

Detailed reactor scans are conducted for each fuel category at 2/3's of the reactor height as shown in Figure 3.2. In all cases, the plots include the scan for pure CH_4 as a comparison point. Both temperature and major species concentrations are measured radially from the reactor centerline to the reactor wall in order to gain perspective on the structure of the LPM flame for each fuel blend.

5.2.1 Pure H_2

The temperature and NO_X profiles for H_2 and CH_4 are shown below in Figures 5.1 and 5.2. Although these two fuels have the same temperature within the recirculation zone, H_2 is far more reactive along the centerline in comparison to the CH_4 and all other pure alkane fuels. Despite a significantly higher temperature on centerline, LPM H_2 combustion is found to produce about 35% less NO_X in comparison to CH_4 measured at the nominal temperature of 1800 K within the recirculation zone.
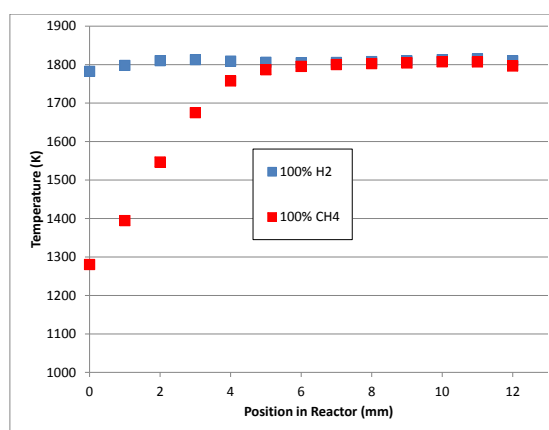
Figure 5.1: Temperature profile across the JSR for LPM CH_4 and H_2 combustion
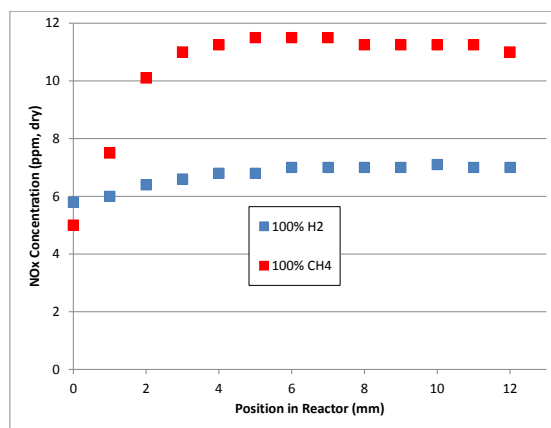
Figure 5.2: NO_X concentration profile across the JSR for LPM CH_4 and H_2 combustion

5.2.2 Process and Refinery Blends

As mentioned above, process and refinery blends are composed mainly of H_2, CH_4, and other higher order hydrocarbons. Similar to the trend shown above, the addition of H_2 appears to increase reactivity on centerline while decreasing overall NO_X emissions. The temperature, CO, and NO_X profiles are shown in Figures 5.3, 5.4, and 5.5, respectively. The increase in reactivity is especially evident looking at the CO profiles in Figure 5.4. While the fuel blends with H_2 and C_2H_6 addition have CO profiles that peak on centerline, pure CH_4 combustion actually peaks off of centerline at a radial location that is slightly larger than the radius of the reactor inlet. Essentially, CH_4 reacts so slowly that the center does not have enough time to make much CO. The faster reacting hydrocarbons make enough CO to show a peak on centerline.
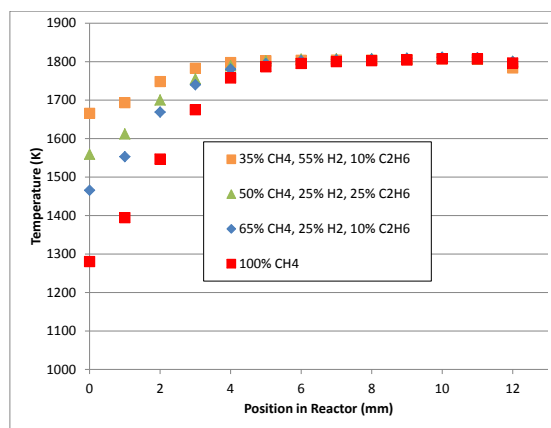
Figure 5.3: Temperature profile across the JSR for the Process and Refinery Fuel Blends
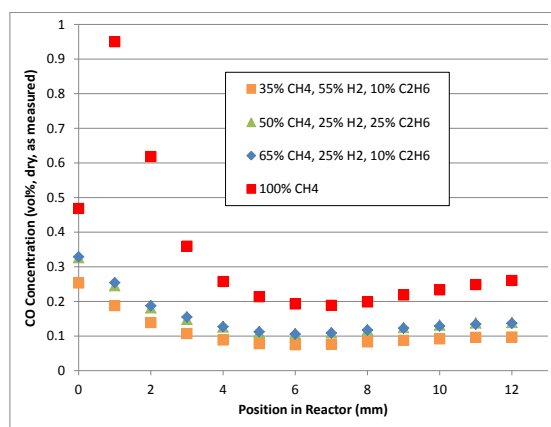
Figure 5.4: CO concentration profile across the JSR for the Process and Refinery Fuel Blends

It is interesting to note the effect of C_2H_6 addition. Table 1.1 shows that both the nominal process and refinery blend and alternative blend 2 contain 25% H_2. However, the nominal blend has 15% more C_2H_6 and this is replaced by CH_4 in the alternative fuel. While both of these blends are more reactive than pure CH_4 on centerline, the addition of C_2H_6 actually increases the temperature by about 100 degrees K on centerline. In Figure 5.5 the NO_X profiles for these two blends are almost identical
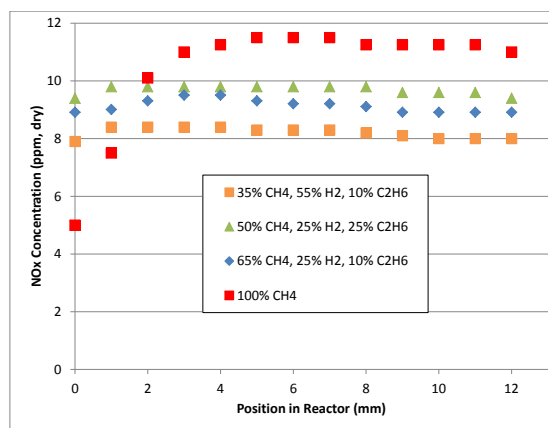
Figure 5.5: NO$_X$ concentration profile across the JSR for the Process and Refinery Fuel Blends

within the accuracy of the instrument; however, the NO$_X$ concentration is about 0.5 ppm larger for the blend with more C$_2$H$_6$. As mentioned above, this result is consistent with previous studies showing that NO$_X$ emissions increase with increasing fuel mole fraction of heavier hydrocarbons [8], [9], [71].

5.2.3   Gasified Coal/Petcoke (O$_2$ Blown)

Category 3 is a product of the gasification process. As outlined above, it is primarily composed of H$_2$ and CO with small concentrations of CO$_2$ but without any hydrocarbon species. The temperature, CO, and NO$_X$ profiles are shown in Figures 5.6, 5.7, and 5.8, respectively.
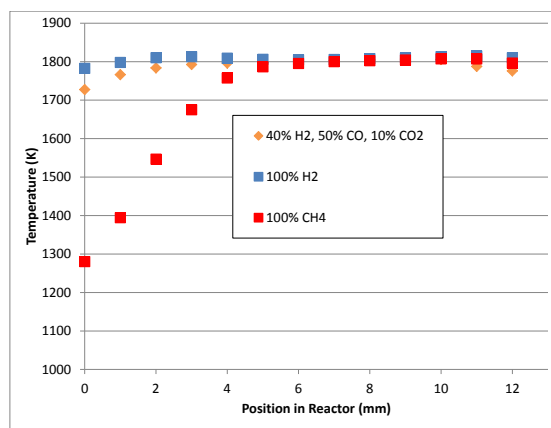
Figure 5.6: Temperature profile across the JSR for the Gasified Coal/Petcoke blend with pure CH_4 and H_2 shown for reference
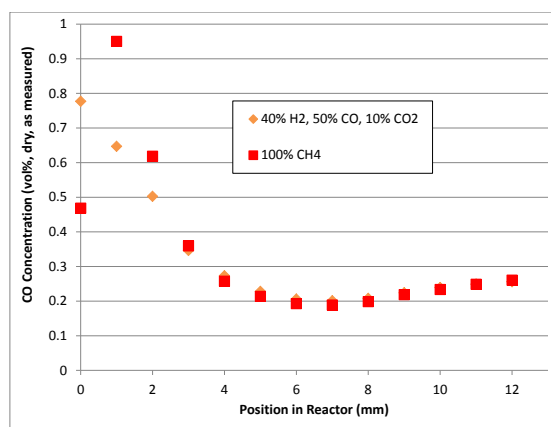
Figure 5.7: CO concentration profile across the JSR for the Gasified Coal/Petcoke blend with pure CH_4 shown for reference

The temperature profiles for the gasification blend and pure H_2 are almost identical. Since H_2 is so highly reactive it dominates over the relatively low reactivity of the CO. Despite the small temperature difference, the gasification blend actually produces about 2 ppm more NO_X than pure H_2 combustion.
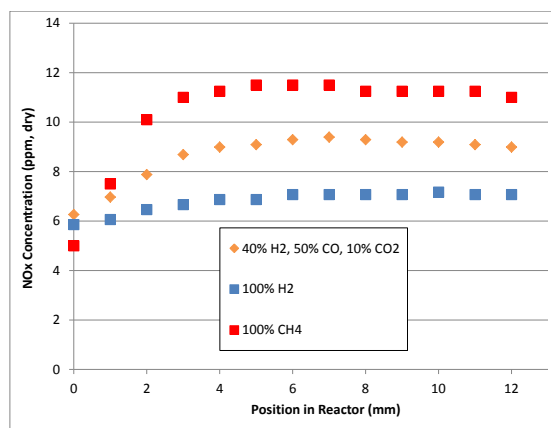
Figure 5.8: NO_X concentration profile across the JSR for the Gasified Coal/Petcoke blend with pure CH_4 and H_2 shown for reference

5.2.4 Landfill and Digester Gas

Landfill gas is mainly composed of CH_4 and CO_2 with varying levels of N_2. The profiles for temperature, CO, and NO_X are shown in Figures 5.9, 5.10, and 5.11, respectively.
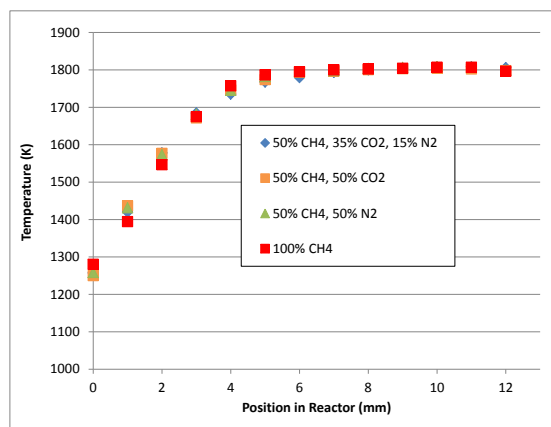
Figure 5.9: Temperature profile across the JSR for the Landfill and Digester Gases with pure CH_4 shown for reference

Although the temperature profiles for each landfill blend and pure CH_4 are practically indistinguishable, the CO and NO_X profiles are quite different. Shown in Figure 5.10, the addition of diluent seems to spread out the reaction zone with the CO concentration peaking at 2 mm away from the centerline instead of 1 mm for CH_4 combustion. This trend makes sense since the addition of diluent will slow the flame speed of the mixture; thus, spreading out the turbulent flame brush region.
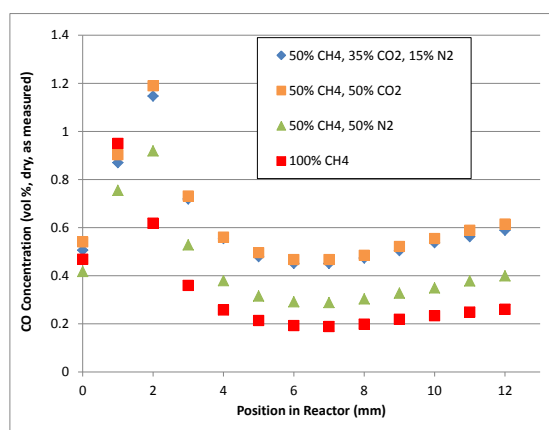
Figure 5.10: CO concentration profile across the JSR for the Landfill and Digester Gases with pure CH_4 shown for reference
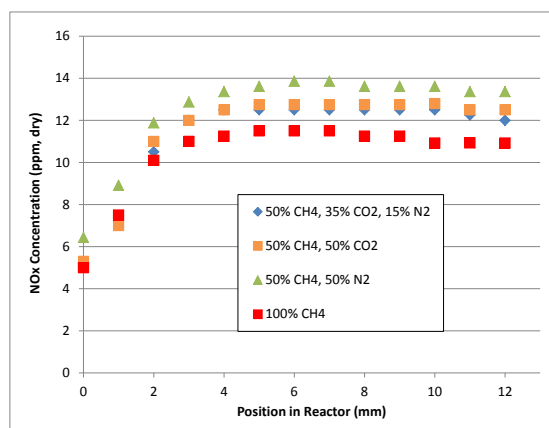
Figure 5.11: NO_X concentration profile across the JSR for the Landfill and Digester Gases with pure CH_4 shown for reference

Note that the CO concentration within the recirculation zone is larger for the landfill gases than for pure CH_4. Within the recirculation zone, the landfill mixtures that contain CO_2 actually have a CO concentration that is more than double that of pure CH_4. The rise in CO emissions for landfill gas blends is partially due to an increase in the equivalence ratio required to maintain temperature (since air flow rate is kept constant). This effect is relatively unaffected by the diluent since both N_2 and CO_2 have approximately the same specific heat (as kJ/kg-K) within the range of preheat and combustion temperatures used in this study ($C_{p,CO_2}/C_{p,N_2} = 0.96$ to 1.07 over the temperature range from 500 to 1800 K). The larger increase in CO emissions for the landfill blends containing CO_2 can possibly be attributed to a competition between CO_2 and O_2 for H-atom, which will lead to increased CO formation through the reaction $CO_2 + H \rightleftarrows CO + OH$ [72]. Since CO_2 could be consuming H-atom, an important reactant in the primary chain branching reaction $H + O_2 \rightleftarrows O + OH$, the presence of CO_2 is expected to result in a smaller radical pool. Although the landfill gas blends with CO_2 and N_2 lead to an increase in NO_X (because of the increased equivalence ratio and thus increased prompt NO_X formation), the main reason for the lower NO_X emissions for the landfill gas diluted with CO_2 compared to N_2 is the smaller radical pool produced when diluted with CO_2.

5.2.5   LNG, Shale, and Associated Gas

LNG, Shale, and Associated Gases are mainly composed of CH_4 with varying levels of C_2 and C_3 hydrocarbons. The profiles for temperature, CO, and NO_X are shown in Figures 5.12, 5.13, and 5.14, respectively.
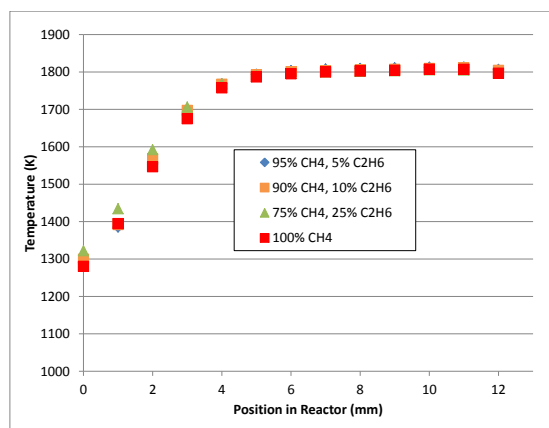
Figure 5.12: Temperature profile across the JSR for the LNG, Shale, and Associated Gases with pure CH_4 shown for reference

Since each of the nominal fuel blends in this category is composed mainly of CH_4, the fact that the temperature profiles are similar is not surprising. The addition of C_2H_6 promotes an increased reactivity on centerline as indicated by the rise of CO concentration shown in Figure 5.13. This added reactivity is also thought to be the main reason for the larger NO_X emissions produced by fuels containing larger amounts of C_2H_6 as shown in Figure 5.14.
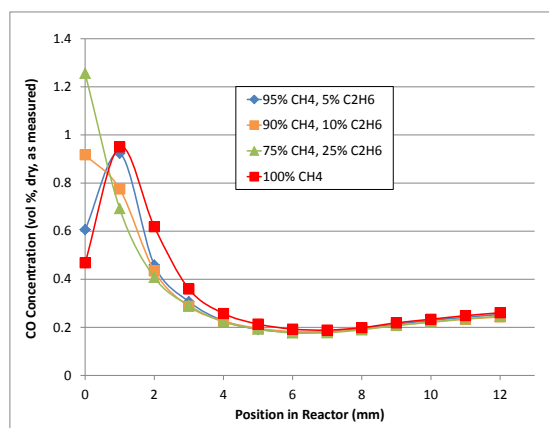
Figure 5.13: CO concentration profile across the JSR for the LNG, Shale, and Associated Gases with pure CH_4 shown for reference
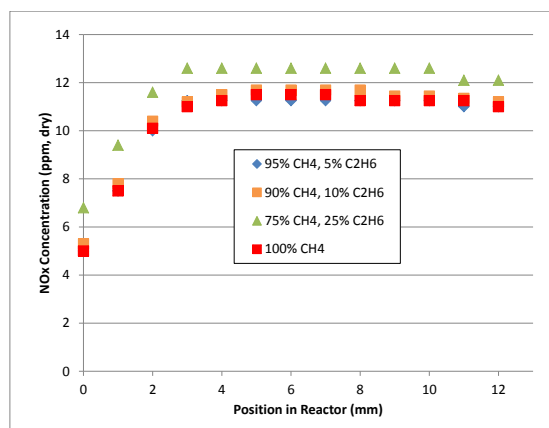
Figure 5.14: NO_X concentration profile across the JSR for the LNG, Shale, and Associated Gases with pure CH_4 shown for reference

5.3 The Effect of Temperature and Residence Time

The formation of NO_X is clearly a function of both combustion temperature and the residence time within the reactor regardless of fuel composition. Figures 5.15 and 5.16 show the variation in NO_X emissions for pure CH_4 combustion for variable residence time and combustion temperature. Consistent with previous studies [54], for LPM CH_4 combustion, NO_X emissions increase exponentially with temperature and linearly with residence time.
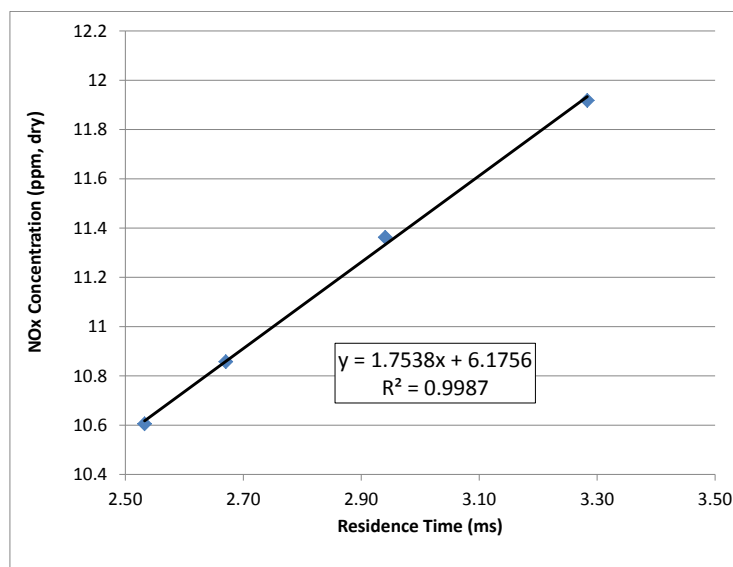
Figure 5.15: Variation of NO$_X$ concentration with reactor residence time for LPM CH$_4$ combustion. Temperature is held constant at 1800 K.
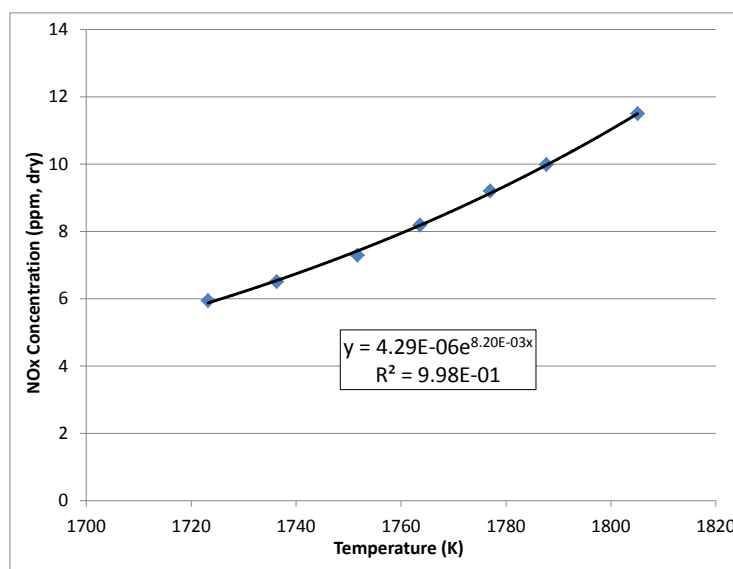
Figure 5.16: Variation of NO$_X$ concentration with reactor temperature for LPM CH$_4$ combustion. The residence time ranges between 2.6 and 2.8 ms for the data shown.

For the temperature variation tests, the mass flow of air is kept constant, while the fuel flow rate is adjusted to achieve a variation in combustion temperature. For the highest combustion temperature studied (1805 K), the fuel flow rate is less than 4% of the total flow, thus assuming an approximately constant residence time is legitimate. A lower combustion temperature will also lead to residence time changes; however this effect is small and the range of residence times calculated for the data shown in Figure 5.16 is between 2.65 and 2.8 ms. The data shown in Figure 5.15 are taken at a constant combustion temperature of 1800 K in the recirculation zone. Here the air flow rate is decreased and the fuel flow is adjusted to maintain a constant temperature.

Figure 5.17 shows the formation of NO_X as a function of temperature and residence time for three additional pure fuels: C_3H_8, C_2H_6, and H_2. As in Figure 5.16, the air flow rate is held constant, while the fuel flow rate is adjusted to vary the combustion temperature. The residence time ranges between 2.55 and 2.8 ms for all data reported.
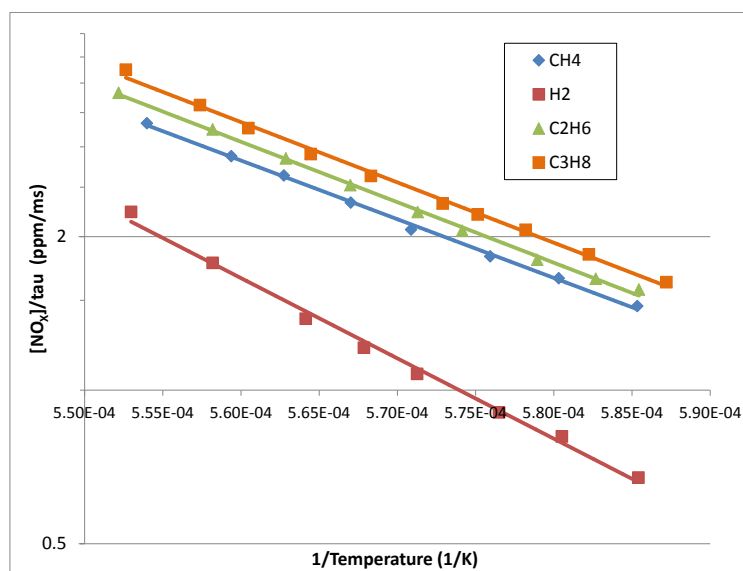
Figure 5.17: Net NO_X production rate for CH_4, C_3H_8, C_2H_6, and H_2 combustion.

Each of these NO_X rates fits an Arrhenius temperature dependance quite well. The least squares fit for the NO_X data from each of the fuels tested is presented in

Equations 5.1 through 5.4, where X is mole fraction in ppm, τ is residence time in ms, and T is combustion temperature in K.

$$X_{\text{NO}_\text{X},\text{CH}_4} = \tau(7.79 \times 10^6) \exp(-26487/\text{T}) \tag{5.1}$$

$$X_{\text{NO}_\text{X},\text{C}_2\text{H}_6} = \tau(1.33 \times 10^7) \exp(-27285/\text{T}) \tag{5.2}$$

$$X_{\text{NO}_\text{X},\text{C}_3\text{H}_8} = \tau(1.4 \times 10^7) \exp(-27220/\text{T}) \tag{5.3}$$

$$X_{\text{NO}_\text{X},\text{H}_2} = \tau(1.07 \times 10^9) \exp(-36235/\text{T}) \tag{5.4}$$

As mentioned above, the residence time for all the data taken in Figure 5.16 is approximately constant. Each of the fuels tested has a lower slope than the global Zeldovich activation temperature of 69,090 K. Since H_2 combustion does not produce prompt NO_X, the Zeldovich pathway is proportionally a larger effect, which causes the NO_X activation temperature to increase for H_2.

While all of the alkanes have similar global activation temperatures, the global activation temperature for H_2 is quite a bit higher. This difference can be partially attributed to the super-equilibrium O-atom concentration for these experiments. The other explanation is that there are other pathways to NO_X formation.

5.4 Blowout

The connection between turbulent flame speed and flow velocity controls the combustion stability under LPM combustion. Flame stability depends both on how well hot recirculating products mix with fresh reactants and the ability to sustain a large enough flame speed relative to the fluid velocity. Lean blowout occurs when the heat release from the primary combustion zone is not high enough to raise the temperature of the reactants to an adequate level to sustain reaction [40].

Since there is limited optical access to the JSR used within this study, flame liftoff cannot be directly verified. However, for most fuels with the exception of CH_4 and the landfill gas blends, there are distinct "popping" or extinction/reignition events

that take place as the mixture approaches blowout in the JSR. These events lead one to believe that the flame is lifting off the nozzle and then reattaching itself until it finally lifts off for good. It is also quite likely is that the flame extinguishes and then is reignited by the hot wall, with cycling between complete blowout and reignition. For CH_4 and the landfill gas blends, the extinction occurs without noticeable "popping".

Blowout tests were conducted for a selected number of the fuel compositions outlined in Table 1.1 with the addition of pure CH_4 for reference. A blowout test can be achieved in a number of different ways: (1) hold the fuel flow constant while increasing the airflow until the flame blows out, (2) increase both the fuel and air flow rate at constant equivalence ratio until the flame blow out, and (3) hold the air flow rate constant while decreasing the fuel flow until a blowout event occurs. Since it is the goal of this study to investigate the difference between a wide variety of fuel blends, it is decided that method (3) is the best experiment to conduct since the fluid dynamics will remain relatively constant for each fuel tested. For all of the blowout experiments conducted, the air flow rate is held constant at 1.08E-3 kg/s and the air inlet temperature is kept at 573 K. The fuel flow rate is gradually decreased until a blowout event occurs.

As mentioned above, the atmospheric pressure JSR is far from adiabatic. Since blowout is highly dependent on the combustion temperature within the reactor, it is important to remove the effect that thermal hysteresis has on the observed blowout temperature. First, the blowout temperature is found by starting at 1800 K and reducing the fuel flow rate so that the reactor temperature decreases by approximately 50 K. This flow rate is then held for 15 minutes and the fuel flow rate is again adjusted to decrease the combustion temperature another 50 K. Eventually the reactor will undergo blowout; however, due to the thermal hysteresis in the system this temperature will be somewhat lower than the actual blowout temperature. That is, the reactor can run at a reduced gas temperature because of the thermal inertia of the reactor solid material. Next, the reactor is heated up to 50 K above the blowout temperature

found in the previous test. The fuel flow rate is then adjusted to achieve a combustion temperature that is 10 K lower than the initial temperature. This flow rate is held for 30 minutes and the process repeated. In between times when the fuel is being adjusted, the temperature in the reactor is falling due to the falling temperature of the solid material; however, it is determined that 30 minutes is a sufficiently long enough time to overcome the thermal inertia of the JSR and the temperature within the reactor stabilizes. Once the new blowout temperature is determined, the test is conducted once more by preheating the reactor to 20 K hotter than the newly determined blowout temperature. The temperature is then decreased in 5 K increments separated by 30 minutes in order to determine a more refined blowout temperature. The composition of fuels tested is shown in Table 5.1 and the results are shown in Figure 5.18.

Table 5.1: Fuel Composition for 16cc reactor Blowout Studies

Mix	Composition (vol %)						
	H_2	CO	CH_4	CO_2	N_2	C_2H_6	C_3H_8
1	100	0	0	0	0	0	0
2-A	25	0	50	0	0	25	0
2-B	55	0	35	0	0	10	0
3	40	50	0	10	0	0	0
4	0	0	50	35	15	0	0
5	0	0	75	0	0	25	0
CH_4	0	0	100	0	0	0	0
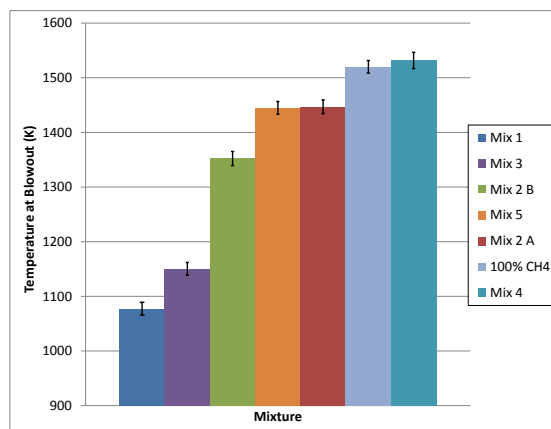
Figure 5.18: Experimentally determined blowout temperature for fuel compositions outlined in Table 5.1.

The results of Figure 5.18 lend themselves to a number of conclusions. First, H_2 blows out about 500 K cooler than pure CH_4. This is not surprising since H_2 is far more reactive than CH_4. When diluent is added to pure CH_4 as in Mix 4, the blowout temperature is somewhat increased, most likely due to the lower reactivity and flame speed due to dilution effects. Mixes 2A and 5 blow out approximately 75 K cooler than pure CH_4. Due to the large C-H bond energy and lack of carbon to carbon (C-C) bonds, CH_4 has a relatively high ignition temperature and in general is less reactive than higher order hydrocarbons such as C_2H_6 [46]. While Mix 5 is 75%/25% CH_4/C_2H_6, Mix 2A contains 25% H_2 in place of some CH_4. It is interesting to note that the H_2 addition does not significantly affect the blowout temperature. Blowout behavior appears to be best represented by the least reactive fuel component in the mixture. This point is further illustrated by comparing blowout temperature between Mixes 3 and 2B. Both mixtures contain about 50% H_2; however, Mix 2B contains hydrocarbon species while the balance of Mix 3 is composed mainly of CO. The difference in blowout temperature is significant (about 200 K). This is thought to be related to the high C-H bond energy of CH_4.

Although it is the goal of this study to determine the emissions and blowout char-

acteristics of actual fuel compositions found in nature and from industrial byproducts, we can learn valuable information by expanding the compositional parameter space beyond that presented by the fuels alone. Figure 5.19 shows that the addition of small amounts H_2 to CH_4 has a relatively small effect and this effect increases as the H_2 mixture fraction gets above 50%. In contrast, the blowout temperature for the CH_4/C_2H_6 follows the CH_4/H_2 mixture up to a 50% mixture fraction and then levels off.
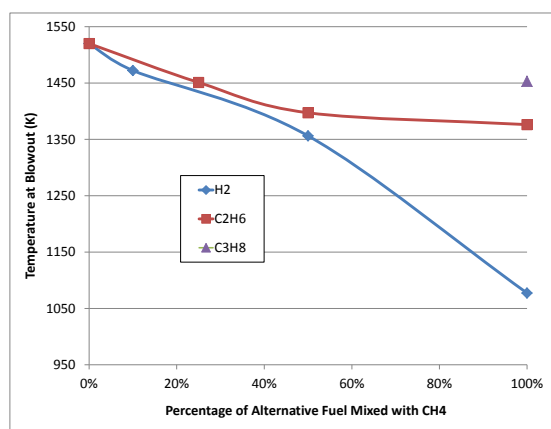
Figure 5.19: Experimentally determined blowout temperature for CH_4 mixed with increasing levels of H_2 and C_2H_6. Blowout for pure C_3H_8 is shown for reference.

5.5 *Available Chemical Mechanisms with NOx Formation Chemistry*

In order to properly model the data, a suitable chemical mechanism must be chosen. The best chemical mechanisms have been developed under conditions similar to those for which the model is to be used. In the case of the present study, the mechanism should be optimized for high temperature oxidation of H_2, CO, and C_1 through C_3 hydrocarbons with NO_X formation. Four mechanisms have been identified that claim to meet or partially meet this description.

GRI-Mech 3.0 was developed under Gas Research Institute support, and was presented in 1999 [73]. The mechanism was developed to model natural gas combustion

with NO_X formation and reburn chemistry. The mechanism was optimized for pre-mixed systems at temperatures between 1000 and 2500 K, pressures between 10 torr and 10 atm, and equivalence ratios between 0.1 and 5. It is composed of 325 reactions including 53 species. C_2H_6 and C_3H_8 kinetics are included, however a cautionary disclaimer states that these species should only be included as minor constituents. Although, the model documentation does not recommend its use to model higher hydrocarbons, we included the mechanism in our study since it should properly model CH_4, H_2, and CO combustion.

Alexander Konnov developed a mechanism for C_1 through C_3 hydrocarbon oxidation, N-H-O chemistry, NO_X formation, and reburn in 2000 [74]. The mechanism is composed of 1200 reactions including 127 species and has been validated for a variety of conditions including shock tubes, laminar flame speeds and laminar flame species profiles; however the validation of the NO_X formation aspect of the mechanism is limited. Nevertheless, Konnov's mechanism is limited since it is said to model C_1 through C_3 oxidation with NO_X formation.

In 2005, UCSD published the latest version of a chemical mechanism that describes high temperature oxidation, ignition, and detonation for H_2, CO, and C_1 through C_3 hydrocarbons [75]. The oxidation mechanism is composed of 235 reactions including 46 species and has been validated through various experimental tests including flame structure and ignition delay. The mechanism does not include NO_X formation chemistry; however, a NO_X mechanism developed by Hewson et al. [76] is provided to be used in conjunction with the combustion mechanism. The resulting mechanism including hydrocarbon oxidation and NO_X formation is 288 reactions including 61 species. Although, the NO_X portion of this mechanism has not been rigorously tested, it is decided to include it since the hydrocarbon portion of the mechanism does include up to C_3 chemistry.

The last mechanism is the C_2-NOx mechanism developed by Reaction Design in 2008 [77]. The mechanism consists of 694 reactions including 100 species. The model

is reportedly good for replicating the oxidation of H_2, CH_4, and C_2H_6 with NO_X formation. The model is a conglomeration of several studies describing oxidation and NO_X formation. Unfortunately it does not include C_3H_8 chemistry.

In addition to the four mechanisms, Konnov et al. [78] recently suggested that there is a non-zero activation energy for the reaction $NNH + O \rightarrow NH + NO$ that is between 3 and 5 kcal/mole. The only modification made to GRI-Mech 3.0 is that the activation energy of this reaction is changed from 0 to 4 kcal/mole. This modification od GRI-Mech 3.0 will be referred to as the Konnov-4 mech for the rest of this document.

Each of these mechanisms is tested against experimental NO_X emissions data from LPM CH_4 combustion going from 1708 to 1805 K. The CRN developed in Chapter 4 is used as the model. The results are shown below in Figure 5.20.
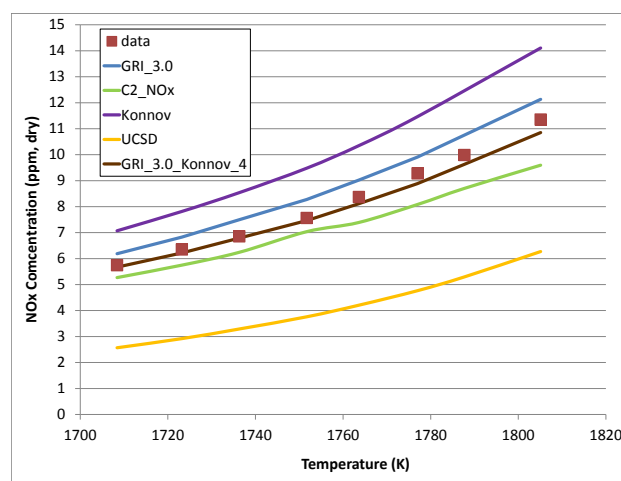
Figure 5.20: Comparison of four different chemical mechanisms against experimental NO_X data going from 1700 to 1800 K for LPM CH_4 combustion.

The modeling results for all of the mechanisms follow the trend of the data with varying levels of accuracy. However, the configuration of the CRN can definitely affect the results. We decided to test how sensitive the CRN is to configuration. In particular, what effect does the volume of the first reactor have on the overall NO_X

prediction from the model? In the 3-element CRN developed in Chapter 4, the size of the first PSR is calculated as the volume of a reactor that is 1% larger than an adiabatic PSR at blowout. This is essentially the size that the reactor will be if there is perfect mixing. The influence that the first reactor volume has on the overall NO_X predictions from the model is shown in Figure 5.21. Using the CRN from Chapter 4,
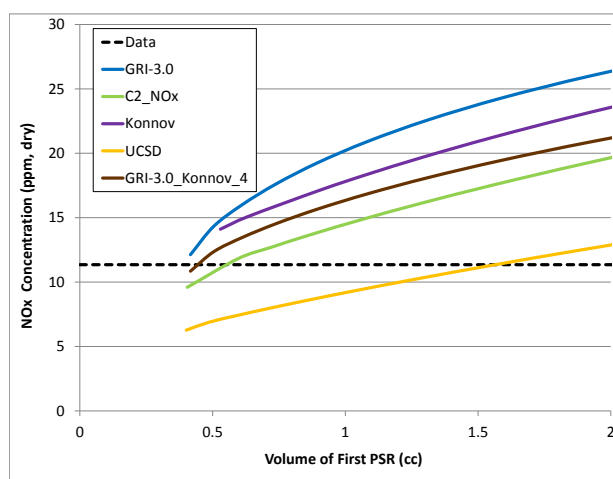
Figure 5.21: Effect that the size of the first PSR has on the overall predicted NO_X emissions using the 3-element CRN. Data is for LPM CH_4 combustion at 1805 K.

the total combustor volume is held constant, the shear reactor volume is held constant, and the volume of the first reactor is increased from the blowout condition with the recirculation zone volume decreasing in size. The data shown in Figure 5.20 are for LPM CH_4 combustion at 1805 K. The temperature of the recirculation zone reactor is run at an assigned temperature of 1805 K. Since the first reactor is an adiabatic PSR, it is expected that the predicted NO_X emissions increase when it gets bigger. Except for the UCSD mechanism, all of the mechanisms indicate that the first PSR is about 0.5 cc. The volume of a PSR at blowout seems to be a reasonable volume for the first PSR; however, is this the correct volume of the first PSR?

ElKady et al. [79] have suggested a different method to determine the size of the first reactor. In a continuation of previous work at GE, researchers studied NO_X

formation in perfectly premixed CH_4/air flames from 1 to 10 atm. They compare their experimental results with results of a chemical reactor network composed of an adiabatic PSR and a PFR in series. They set the overall residence time constant and use a PSR time equal to the chemical time of the first reactor as shown below in Equation 5.5.

$$\tau_{cts} = \frac{(k/C_p)_{T_o}}{\rho_u S_L^2} \tag{5.5}$$

The volume of the first reactor is computed by the chemical time, τ_{cts}. The thermal conductivity, k, and specific heat, C_p, are evaluated at the inner layer temperature, T_o, which is the average temperature of the reactants and products. The unburned density, ρ_u, and the laminar flame speed, S_L, are evaluated and calculated at the unburned mixture properties, respectively. The unburned density, specific heat, and thermal conductivity will be equal for each mechanism; however, the laminar flame speed is certainly mechanism dependant. The computed chemical times and corresponding PSR volumes are shown in Table 5.2. As shown in Figure 5.21, these new volumes will result in an over prediction of the data for both versions of GRI, Konnov, and C_2-NOx. The UCSD mechanism still under-predicts the data.

Table 5.2: The chemical times computed for each mechanism by Equation 5.5 and the corresponding PSR volume.

Mechanism	τ_{cts} (ms)	Volume (cc)
GRI	0.127	0.74
UCSD	0.149	0.88
C2-NOx	0.168	1.01
Konnov	0.162	0.95

Another approach would be to assume that the size of the first reactor volume is controlled by the slowest process, which would be the value of k/ε, or 1.2 ms. This would give a computed volume of the first reactor of 7.8 cc, which is clearly too large.

As mentioned before, each mechanism that has been evaluated predicts the correct trend in the experimental data. The results of the model are definitively dependant on the configuration of the reactor network; in particular, the results are dependant on the size of the first reactor. It appears that this reactor represents a highly turbulent region where the chemistry becomes the controlling time scale. Thus, sizing it to match the PSB or using the approach from ElKady et al. [79] is appropriate. Both of these approaches give qualitatively similar results, and can be thought of as error bounds.

Given the above results, it becomes hard to pick a mechanism winner. Although GRI-Mech 3.0 is over ten years old, it still performs quite well in comparison to the the other mechanisms when it comes to NO_X prediction in our LPM CH_4 system. GRI-Mech 3.0 with the suggested modification by Konnov performs slightly better than GRI without the modification. The C_2-NOx mechanism also performs fairly well for our conditions, which is not surprising since much of its NO_X chemistry is taken from GRI-Mech 3.0. The NO_X chemistry used in conjunction with the UCSD mechanism significantly under-predicts the experimental results. One could propose to use the NO_X chemistry from GRI-Mech 3.0 in place of the chemistry set that UCSD provides. One major problem with doing that is the fact that the UCSD mechanism does not contain certain reactions containing CH, which will affect the prompt pathway. Konnov's mechanism is just as old as GRI-Mech 3.0, it over predicts the data and becomes very unstable near blowout. The numerical instability is most likely due to the size of the mechanism.

Since GRI-Mech 3.0 is quite stable and performs well when predicting NO_X emission data from the LPM CH_4 runs, it will be used for the majority of the modeling shown in this dissertation when CH_4 is the main constituent. The authors of GRI-Mech 3.0 give a disclaimer that it should not be used in systems containing large amounts of C_2H_6 and C_3H_8 [73]; thus, the C_2-NOx mechanism will be used in it's place when applicable. There will be certain situations where Konnov's modification

of GRI-Mech 3.0 will be used, since it probably better reflects NNH chemistry and will become important with fuels and conditions where NNH chemistry plays a large role. The residence time at mixture blowout is essentially a property of the unburnt mixture and using it to compute the size of the first element in the 3-element reactor network appears to best reproduce the experimental NO_X data. For these reasons, the PSB volume/residence time will be used to predict the volume of the first reactor instead of the other methods mentioned above.

5.6 CH_4 Modeling

Good agreement between the modeling results and the experimental data for LPM CH_4 combustion is shown below in Figure 5.22. Both the modeled and experimental NO_X data are divided by residence time and plotted against the inverse of the combustion temperature representing an Arrhenius plot.
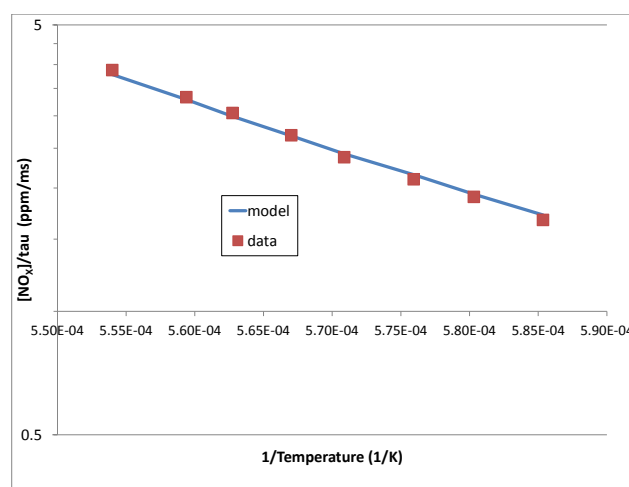
Figure 5.22: Net NO_X production rate for LPM CH_4 combustion showing both experimental and modeling results.

In order to gain better insight on the modeling results, each of the four NO_X production pathways presented in Chapter 2 is isolated using the method outlined

in the next paragraph and the model is rerun. The complete NO_X mechanism for GRI 3.0 is shown below in Table 5.3. It shows each reaction within the GRI 3.0 NO_X mechanism along with the most likely direction of reaction under LPM conditions. The units are as follows: the pre-exponential factor for each reaction is equal to 10^A (mole/cm^3-s), b is the temperature exponent corresponding to $(T/T_o)^b$, T_o is 298 K, and the activation energy, Ea, has units of kcal/mole [68].

The NO_X contribution from each pathway is determined via two independent methods in order to provide a check. The procedure for Method 1 is the following. First we remove all reactions besides the Zeldovich pathway (Reactions 1 - 3). We then run the model, and the computed results are the NO_X production from the Zeldovich pathway only. Next, we add the reactions associated with the NNH pathway (Reactions 10 - 22). We then run the model again and the results give the contributions from the Zeldovich and NNH pathways; thus the difference of the two is the contribution from the NNH pathway alone. Lastly, we add the reactions associated with the prompt mechanism (Reactions 23 - 34). We run the model again to determine the contributions from the Zeldovich, NNH, and prompt pathways. The difference of this result from the previous result is the contribution from the prompt pathway alone. The difference between the entire mechanism and the contributions from the Zeldovich, NNH, and prompt pathways is the contribution from the N_2O pathway.

An important question is whether the appearance of common reactions between the mechanisms lead to synergies and thus non-additive results. Each mechanism is primarily rate controlled by the first step that converts N_2 to a reactive species, , with the subsequent reactions being relatively fast. Thus, a mechanism can be effectively disabled by removing the key initiating reaction from N_2. Instead of removing all the reactions associated with a mechanism, in Method 2 the rate limiting reactions are the only reactions removed, and each reaction path is run separately. For example, to determine the contribution from the Zeldovich pathway only, the initial, rate limiting reactions from the NNH, prompt, and N_2O pathways are removed. In other words,

Table 5.3: Major Reactions of NO_X formation

Zeldovich Mechanism									
Reaction	Reactants			Direction	Products			A	b	Ea
1	N	NO		←	N2	O		13.431	0	0.355
2	N	O2		→	NO	O		9.954	1	6.5
3	N	OH		→	NO	H		13.526	0	0.385
Nitrous oxide mechanism									
	Reactants			Direction	Products			A	b	Ea
4	N2O		M	↔	N2	O	M	10.898	0	56.02
5	N2O	O		→	N2	O2		12.146	0	10.81
6	N2O	O		→	NO	NO		13.462	0	23.15
7	N2O	H		→	N2	OH		14.588	0	18.88
8	N2O	OH		→	N2	HO2		12.301	0	21.06
9	NH	NO		←	N2O	H		14.562	-0.45	0
NNH mechanism									
	Reactants			Direction	Products			A	b	Ea
10	NNH			←	N2	H		8.519	0	0
11	NNH	M		←	N2	H	M	14.114	-0.1	4.98
12	NNH	O2		←	HO2	N2		12.699	0	0
13	NNH	O		←	OH	N2		13.398	0	0
14	NNH	H		←	H2	N2		13.699	0	0
15	NNH	OH		←	H2O	N2		13.301	0	0
16	NNH	CH3		←	CH4	N2		13.398	0	0
17	NNH	O		→	NH	NO		13.845	0	0
18	NH	OH		→	N	H2O		9.301	1.2	0
19	NH	O		→	NO	H		13.602	0	0
20	NH	O2		→	NO	OH		6.107	1.5	0.1
21	N	O2		→	NO	O		9.954	1	6.5
22	N	OH		→	NO	H		13.526	0	0.385
Fenimore prompt (CH) mechanism									
	Reactants			Direction	Products			A	b	Ea
23	CH	N2		→	HCN	N		9.494	0.88	20.13
24	HCN	O		→	NCO	H		4.307	2.64	4.98
25	NCO	O		→	NO	CO		13.371	0	0
26	NCO	OH		→	NO	H	CO	12.398	0	0
27	NCO	O2		→	NO	CO2		12.301	0	20
28	HCN	O		→	NH	CO		3.705	2.64	4.98
29	NCO	H		→	NH	CO		13.732	0	0
30	NH	OH		→	N	H2O		9.301	1.2	0
31	NH	O		→	NO	H		13.602	0	0
32	NH	O2		→	NO	OH		6.107	1.5	0.1
33	N	O2		→	NO	O		9.954	1	6.5
34	N	OH		→	NO	H		13.526	0	0.385

in the Zeldovich only model, Reactions 4, 10, 11, and 23 are removed. In the NNH only model, Reactions 1, 4, and 23 are removed. In the N_2O only model, Reactions 1, 10, 11, and 23 are commented out. Finally, in the prompt only model, Reactions 1, 4, 10, and 11 are commented out. As shown in Figure 5.23, the results between Methods 1 and 2 are nearly identical.
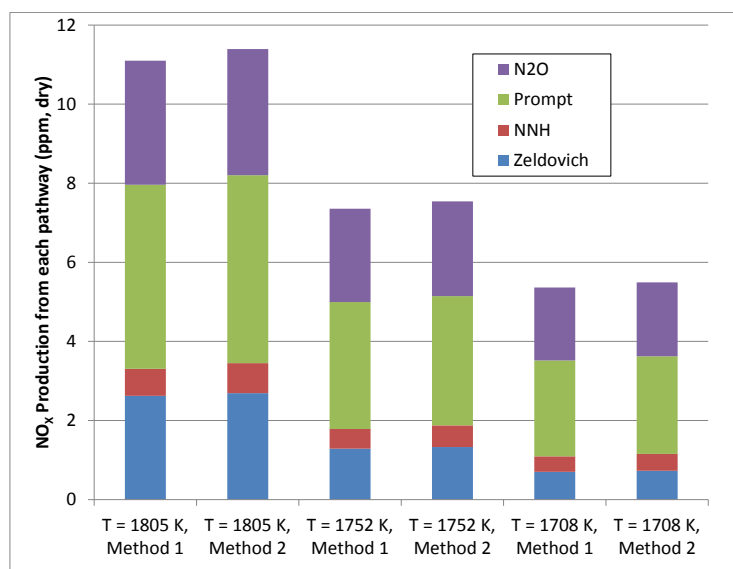
Figure 5.23: NO_X production for LPM CH_4 combustion from each of the four pathways calculated for a series of temperatures from 2 different methods.

We consider Method 2 (only commenting out the key reactions) to be the better of the two algorithms since it only influences a handful of reactions rather than 20 to 30 reactions. Thus, Method 2 is used for the remainder of this study to determine the contribution to NO_X production from each of the four pathways.

The contribution from each of the four pathways is shown in Figure 5.24 in terms of a production rate in moles/s. This figure shows the pathway contribution within the two most important reactors of the CRN for three different combustion temperatures. Due to the small volume and extremely short residence time of the shear reactor (it has approximately three times more mass flow than the flame brush), it does not

significantly contribute to NO_X formation. Thus, attention is focussed on the flame brush and recirculation zone.
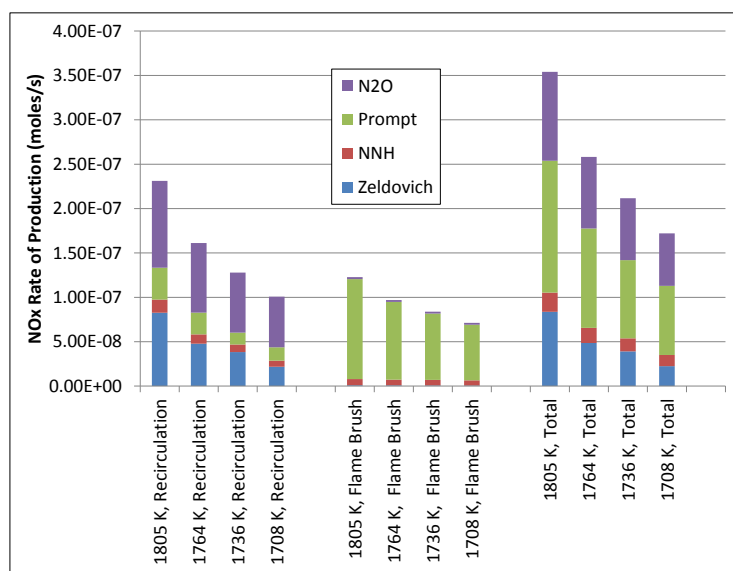
Figure 5.24: NO_X rate of production from each of the four pathways in the recirculation zone and turbulent flame brush elements of the CRN model outlined in Chapter 4.

As shown in Figure 5.24, the total production of NO_X is of equal magnitude in both the turbulent flame brush and the recirculation zone. The majority of the prompt NO_X is formed in the flame brush, while nearly all of the NO_X formed via the Zeldovich and N_2O pathways occurs in the recirculation zone. It is interesting to note that while the NNH and N_2O pathways have approximately equal contributions as the temperature in the recirculation zone falls, both the Zeldovich and prompt pathways decrease in production efficiency. This can be explained by looking at the pertinent radical concentrations in the recirculation zone and flame brush shown in Figure 5.25.
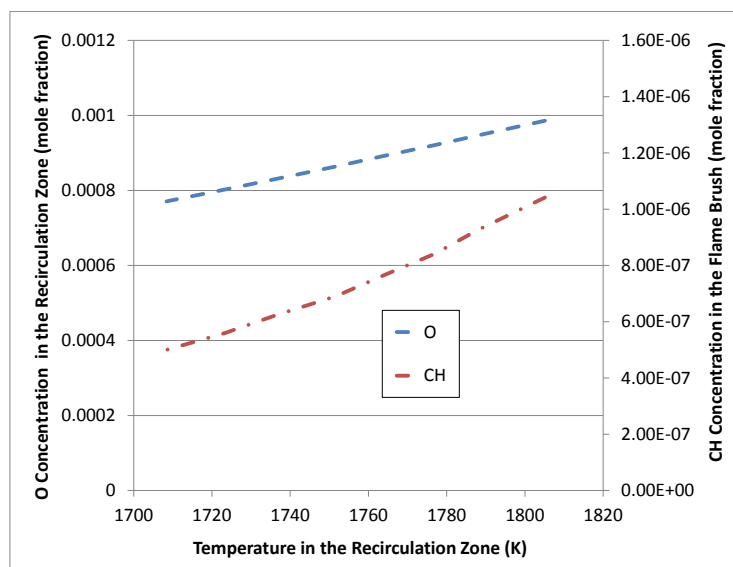
Figure 5.25: O concentration in the Recirculation Zone and CH concentration in the Flame brush for the modeling results shown in Figure 5.22.

Since the air flow is fixed in the above experiments, the equivalence ratio falls from 0.71 to 0.64 as the recirculation zone temperature decreases from 1805 to 1708 K. The CH radical concentration in the flame brush also falls as the flame becomes leaner, which then results in a decrease in NO_X production from the prompt pathway within the flame brush. Also shown is a decrease in O radical in the recirculation zone as the temperature falls. Although this loss of O radical can partially explain the decrease in NO_X from the Zeldovich pathway, the decrease in combustion temperature most likely has a greater effect since the backward rate of Reaction 1 in Table 5.3 is strongly dependent on combustion temperature. In summary, for the experimental results displayed in Figures 5.16 and 5.22, the NO_X concentration falls mostly due to a decrease in the prompt contribution from leaner operation and a decrease in the contribution from the Zeldovich pathway due to a decrease in combustion temperature and a loss of O-atom.

5.7 Parameter Studies

As mentioned before, in addition to investigating specific fuel compositions, it is important to run experiments on a wider parameter space in order to determine more specifically how one or more fuels affect each other. This section describes compositional parameter studies for CH_4 mixed with varying amounts of H_2, C_2H_6, CO, CO_2 and N_2. Additionally, a syngas compositional space is studied with increasing amounts of CO mixed into a stream of H_2. The studies shown in this section simulate a broader variation in Mixtures 2, 3, 4, and 5 than outlined in Table 1.1.

5.7.1 CH_4 mixed with CO_2 and N_2

The experimental results shown below focus on the influence of each diluent on NO_X production in LPM CH_4 combustion. The experiments are designed to hold the temperature constant for all diluent concentrations (N_2 versus CO_2). This is achieved as follows. First, the air flow is held constant. The CH_4 flow is selected to achieve a constant temperature of 1800 K in the recirculation zone. As the diluent loading is increased, the natural tendency of the reactor to run cooler is balanced by increasing the CH_4 flow rate. Thus, as the diluent is increased, the CH_4 flow rate is also increased, and the overall fuel/oxidant ratio approaches stoichiometric.

An important question is how to best present the NO_X data. In the present experiments (1) the stoichiometry varies, and (2) the CO_2 and N_2 dilute the flow. NO_X mole fraction (as ppm) is the normal way to present the emission data. The mole fraction is, however, influenced by dilution effects, in this case both due to stoichiometry and the added N_2 and CO_2. While the stoichiometry effect can be handled by correcting to a common O_2 value, the presence of the N_2 and CO_2 can change mole fraction without any change in chemistry. It is concluded that the most meaningful way to present the data is as a NO_X emission index, i.e., the amount of NO_X formation attributed to each CH_4 molecule entering the reactor. This avoids

mole fraction changes that are due only to dilution (via variable stoichiometry, or N_2 and CO_2 addition). Recently, ElKady et al. [36] have derived a NO_X correction to 15% O_2 that is based on an oxidizer composed of O_2, N_2, and CO_2; however, the derivation presented in Appendix B shows that their method is algebraically equivalent to the emission index, within a constant. For the remainder of this section, the NO_X emissions are expressed as an emission index since it is a more common method of expressing pollutant emissions.

Figure 5.26 shows that the NO_X emission index (grams NO_X/kg CH_4) increases for both N_2 and CO_2 dilution.
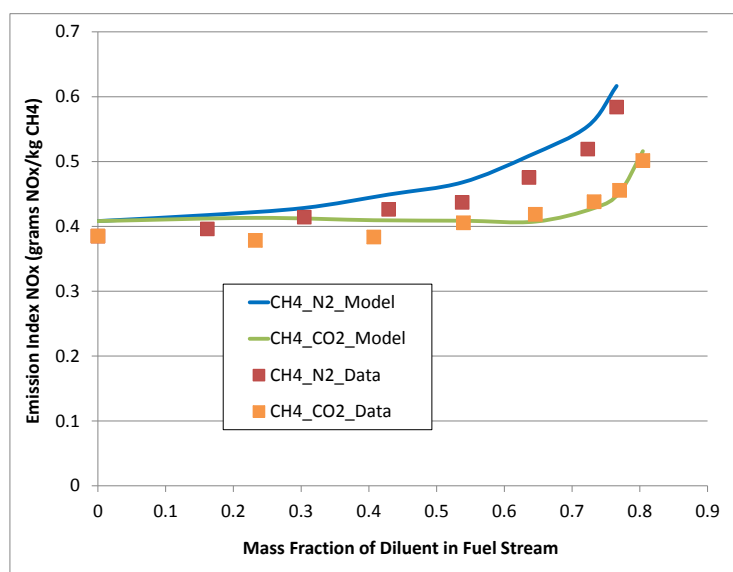
Figure 5.26: Measured NO_X as EI versus mass fraction of N_2 or CO_2 diluent in fuel stream. Temperature is maintained constant at 1800 K

The results also show that dilution with N_2 is more effective at enhancing NO_X formation than CO_2 dilution. There are, however, several ways to correlate the effect of the diluents, e.g., plotting against mass fraction of diluent, mole fraction of diluent, etc. As mentioned above, increasing the diluent flow requires an increase in CH_4 flow

to maintain the 1800 K reactor temperature. This means that the mixture approaches a stoichiometric fuel-air ratio and the O_2 concentration decreases. In examining the various ways to correlate the effect of the diluents on NO_X formation, we selected plotting against O_2 concentration as the most fundamental approach, because the relationship between fuel, O_2, and NO_X is at the core of the chemical behavior.
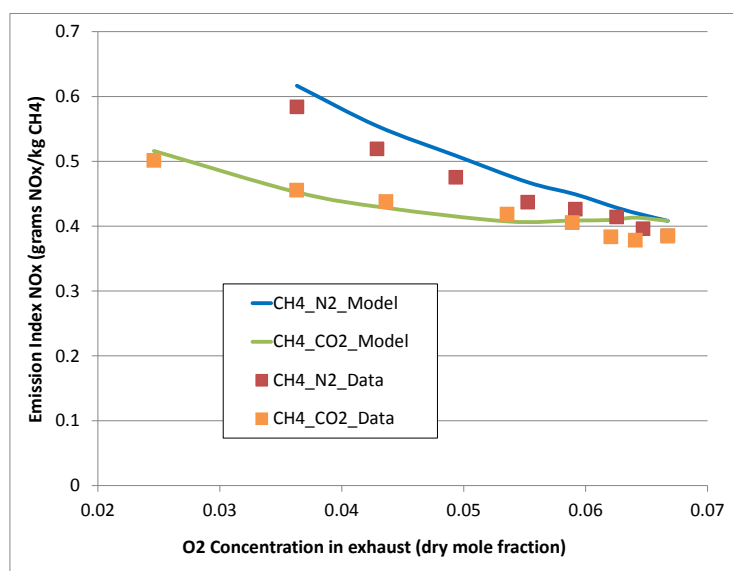
Figure 5.27: Measured NO_X as EI versus exit gas O_2 (mole %, dry). Temperature is maintained constant at 1800 K

Figure 5.27 shows the NO_X emissions index plotted against the O_2 concentration in the exhaust. As in Figure 5.26, the fuel stream diluted with N_2 is more effective at producing NO_X emissions than with CO_2 dilution when compared on a common O_2 basis. Thus, there is evidence to suggest that there may be a chemical kinetic explanation for this phenomenon.

For reference, the measured NO_X (expressed as ppm) is displayed versus exhaust O_2 concentration in Figure 5.28. Note that Figures 5.27 and 5.28 show the same trend. In general, the specific heat of the two additives on a mass basis is sufficiently similar that (1) the tendency of the reactor to cool upon additive addition is nearly
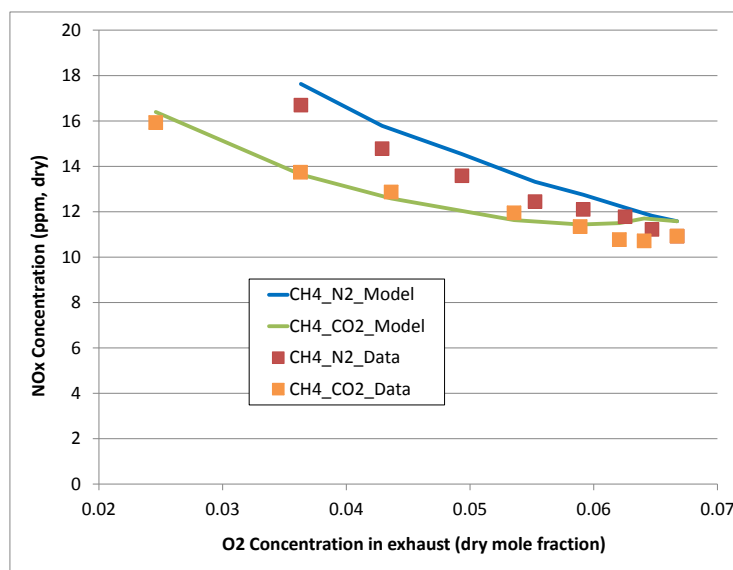
Figure 5.28: Measured NO_X as (ppm, dry) versus exit gas O_2 (mole %, dry). Temperature is maintained constant at 1800 K

the same for the two, and (2) the increase in CH_4 flow needed to maintain the 1800 K flame temperature is similar between the two. Thus, in this case the mole fraction results and the emission index results report similar trends. The other effect that can influence the data on an emission index basis is the increasingly larger molecular weight of the product gas as more CO_2 is added. For N_2 dilution, the molecular weight remains essentially constant throughout the entire range of experiments. As shown in Figures 5.26 through 5.28, the model predicts the data quite well.

These results raise two main questions: 1.) why do NO_X emissions go up when the O_2 in the exhaust decreases/mass fraction of diluent increases? and 2.) why are NO_X emissions higher for fuels diluted with N_2 rather than CO_2?

In an approach similar to the analysis done above in Section 5.3, each of the four NO_X production pathways is isolated and the model is rerun. The contributions of each of the four pathways as a function of dilution are shown in Figures 5.29 and 5.30. Figure 5.31 shows the pathway contribution within each reactor of the

CRN at a common O_2 concentration of 3.6% dry mole fraction in the exhaust. Here the emission index from each of the reactors is normalized by reactor volume and residence time.
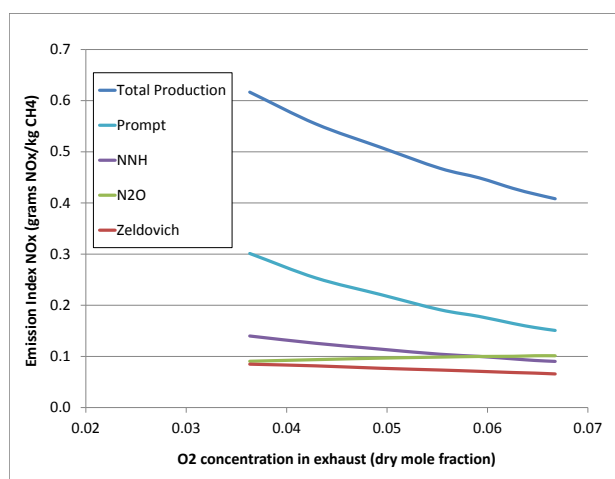
Figure 5.29: NO_X emission index predicted by CRN model: total and by four pathways. CH_4 diluted with N_2
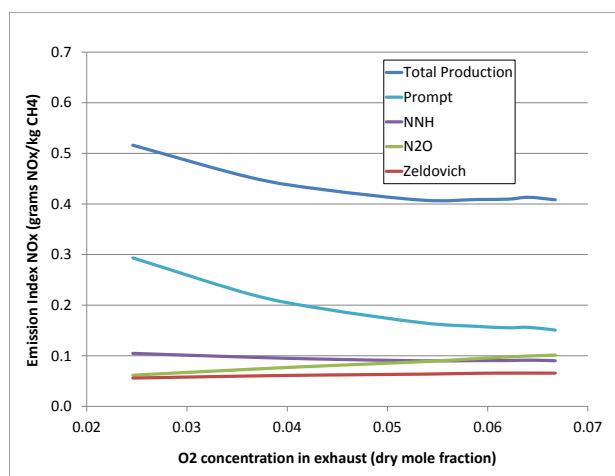
Figure 5.30: NO_X emission index predicted by CRN model: total and by four pathways. CH_4 diluted with CO_2
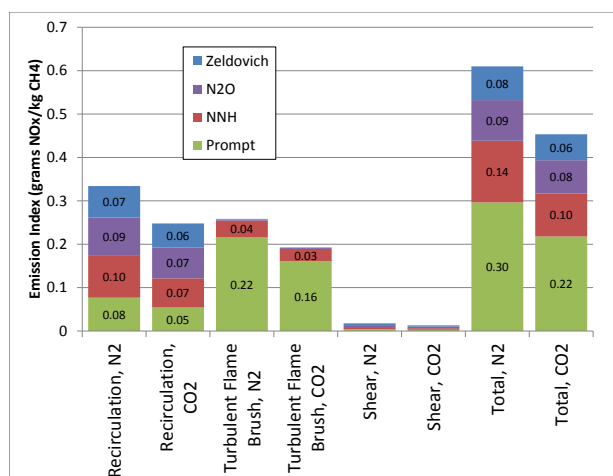
Figure 5.31: NO$_X$ production reported as emission index for each of the four mechanisms in each of the three reactor elements of the CRN model. O$_2$ concentration is 3.6% (dry mole fraction)

Analysis of Figures 5.29, 5.30, and 5.31 show the following trends for NO$_X$ formation in the JSR:

1. Similar to the atmospheric pressure modeling work done by Li et al. [38], prompt NO$_X$ is the major source of NO$_X$ for this experiment, and all three figures support this.

   (a) This may be related to the relatively high CH$_4$-air equivalence ratios used: 0.71-0.86 for N$_2$ dilution and 0.71-0.92 for CO$_2$ dilution. Note that for most LPM combustion devices operating on CH$_4$, the equivalence ratio ranges from 0.45 to 0.65.

   (b) The prompt NO$_X$ increases as the dilution level is increased (i.e. as the exit gas O$_2$ decreases). This is expected because of the increasing amounts of CH$_4$ required as the dilution levels are increased.

   (c) Much of the prompt NO$_X$ is formed in the turbulent flame brush (i.e. flame zone) modeled as an adiabatic PSR operating near blowout condition.

2. NNH contributes a relatively small amount of NO_X and the N_2O and Zeldovich sources of NO_X are negligible within the flame brush as shown in Figure 5.31, because of this reactor's short residence and low temperature. The computed temperature within the flame brush ranges between 1609 and 1612 K for both diluted fuels at all dilution levels.

3. All four sources of NO_X contribute in the recirculation zone, modeled as a PSR at measured temperature (1800K).

4. The sources of NO_X are greater for N_2 dilution than for CO_2 dilution in both the turbulent flame brush and the recirculation zone.

These NO_X trends are supported by the concentrations of free radicals O, H, and CH shown in Figures 5.32, 5.33, and 5.34, as calculated from the CRN modeling.
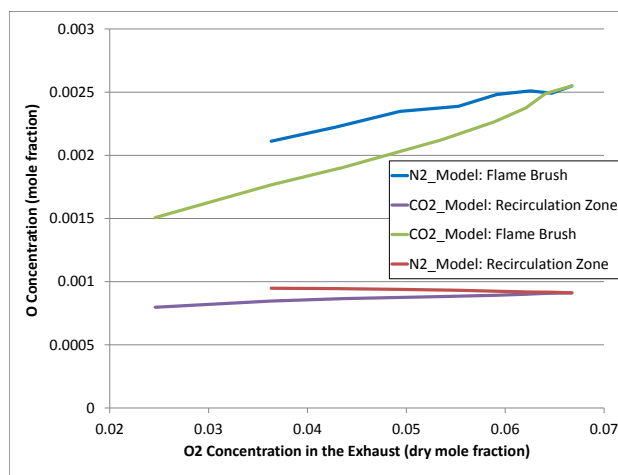
Figure 5.32: O atom concentration in the recirculation zone and PSB for both diluted fuels

When compared to no dilution, the N_2 mole fraction is 5% greater for maximum N_2 dilution and 17% smaller for maximum CO_2 dilution. For small concentrations of NO_X at constant temperature (which is the case here) Zeldovich NO_X forms in
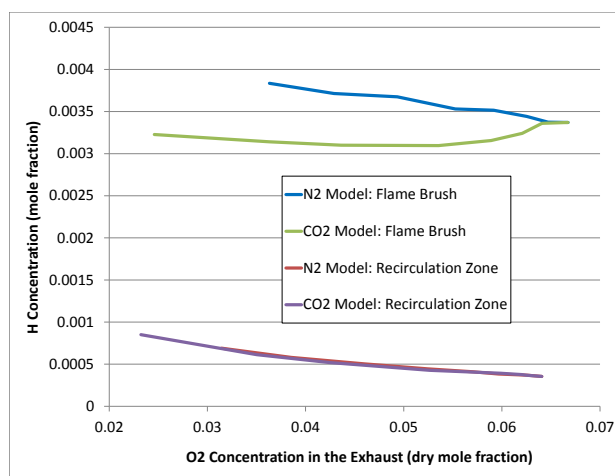
Figure 5.33: H-atom concentration in the recirculation zone and turbulent flame brush for both diluted fuels
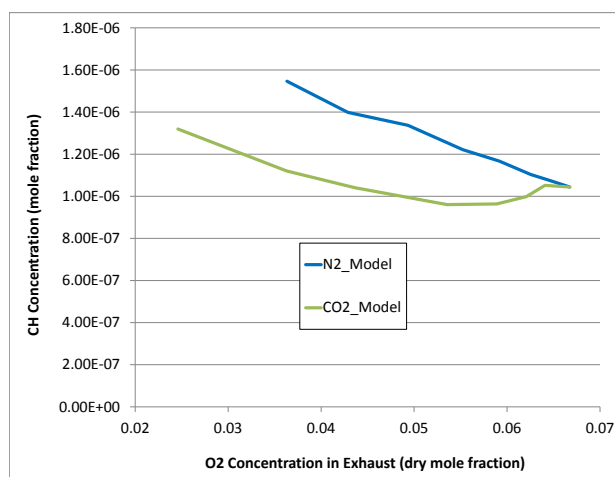
Figure 5.34: CH concentration within the Flame Brush for CH_4 diluted with both N_2 and CO_2

proportion to $[N_2][O]$, where [ ] means moles/vol. Looking at the recirculation zone, for increasing N_2 dilution, O is nearly constant and N_2 increases; thus, Zeldovich NO_X increases with dilution. However, for increasing CO_2 dilution, mole fractions of both O and N_2 decrease: thus, Zeldovich NO_X decreases with dilution.

Nitrous oxide (N_2O) is formed by reaction of N_2 with O and is depleted by reaction with both O and H. As shown above in Figure 5.31 most of the NO_X formed through the N_2O pathway is formed in the recirculation zone. Figure 5.33 shows H-atom increasing as the dilution level of the JSR increases. This trend is the same for both N_2 and CO_2 dilution. Shown in Figure 5.32, the O concentration in the recirculation zone falls slightly for CO_2 dilution and stays flat for dilution with N_2. For N_2 dilution, N_2 and H increase, thus increasing NO. O-atom decreases, which drives NO down. These effects appear to offset each other. For CO_2 dilution, H increases, which promotes NO production; however both N_2 and O decrease, which decreases NO production. The effects of decreased N_2 and O seem to dominate, decreasing the NO production from CO_2 dilution slightly more than for dilution with N_2.

As seen in Figures 5.29 and 5.30, NO formed from NNH increases as the N_2 and CO_2 dilution levels increase. As noted from Figure 5.31, it forms in both reactor zones. NNH is formed by reaction of N_2 with H, and NO is formed by reaction of NNH with O. NNH concentration follows the upward trend shown for H-atom in Figure 5.33, tempered by increasing N_2 concentration for N_2 dilution and decreasing N_2 concentration for CO_2 dilution. The result is a somewhat greater increase in NO with dilution level for N_2 than for CO_2.

Prompt NO forms as CH radical reacts with N_2 to form HCN and N, both of which oxidize to NO. CH has a short lifetime; thus, the prompt NO is produced more significantly in the flame brush than in the recirculation zone. The flame brush concentrations of CH are plotted in Figure 5.34, where they are seen to increase significantly as more N_2 is added to the reactor. Small amounts of CO_2 dilution appear to suppress CH, though as more CO_2 is added, the CH increases.

In addition to the above analysis, both Glarborg et al. [72] and Liu et al. [80] have shown that large concentrations of CO_2 will compete with O_2 for H-atom via the reaction: $H + CO_2 \rightleftarrows CO + OH$. The consumption of H atom will decrease the rate of the most significant chain branching reaction: $H + O_2 \rightleftarrows OH + O$. This suppression

effectively reduces the size of the O/H/OH radical pool, leading to a decrease in NO_X formed by the Zeldovich, N_2O and NNH pathways when CO_2 rather than N_2 is added to the reactor.

5.7.2 CH_4 mixed with H_2

In the experimental studies shown in this section, the air flow rate is held constant, while the flow rates of both CH_4 and H_2 are adjusted to maintain a combustion temperature of 1800 K within the recirculation zone. As shown in Figure 5.35, for a constant recirculation zone temperature of 1800 K the NO_X concentration decreases with increasing H_2 concentration in the fuel stream.
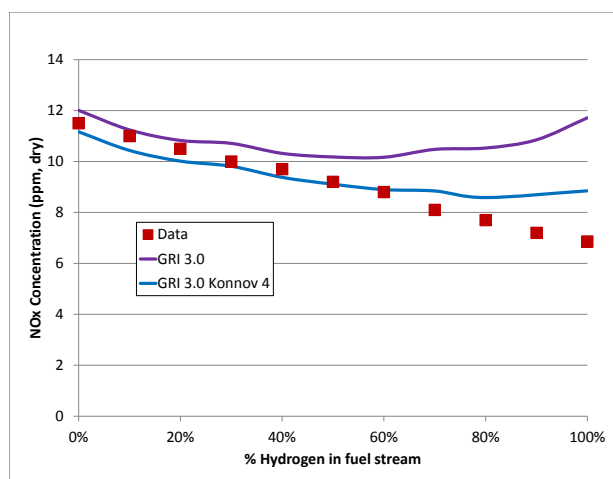
Figure 5.35: NO_X concentration as a function of H_2 concentration in the fuel stream for a fuel mixture of CH_4 and H_2. Combustion temperature is kept constant at 1800 K.

The model is run using the CRN described in Chapter 4 with both GRI Mech 3.0 [73] and GRI Mech 3.0 modified by Konnov [78]. Although the NNH mechanism does not appear to affect NO_X formation from CH_4 combustion significantly, it certainly does affect NO_X formation as a highly reactive, high H radical producing fuel such

as H_2 is mixed into the fuel. Since there is clearly an issue with GRI Mech 3.0 over predicting the data because of the NNH mechanism, GRI 3.0 with the Konnov modification is applied from this point forward to study fuels mixed with H_2.

The model predicts the data fairly well up to about 80% H_2 and then it diverges. At this point, there is not a clear explanation for the model divergence when large levels of H_2 are added to CH_4. It is possible that the CRN configuration needs to be adjusted for fuels with large levels of H_2 since it is far more reactive than hydrocarbon fuels. The model is somewhat self adjusting to changes in chemistry since the blowout volume of the flame brush decreases in size for more reactive chemistry (e.g. higher inlet temperature, larger % H_2, etc.). As shown in Figure 5.36, the computed volume of the flame brush decreases significantly moving from pure CH_4 to pure H_2.
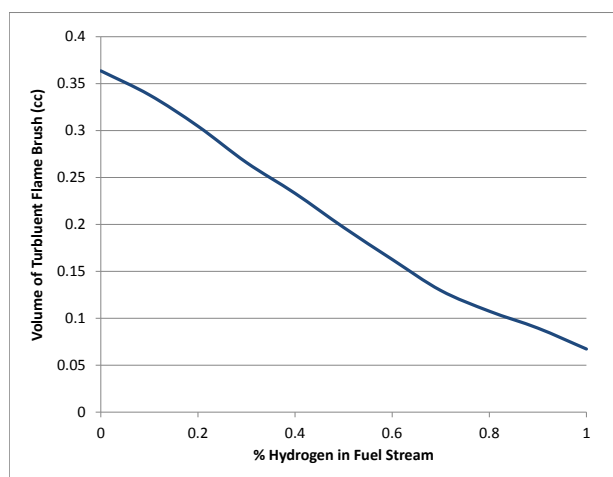
Figure 5.36: Volume of Turbulent Flame Brush as a function of H_2 concentration in the fuel stream. Combustion temperature is kept constant at 1800 K.

As described in Chapter 4, the recirculation zone then occupies the rest of the volume of the JSR minus a very small volume occupied by the shear zone. It is possible that one or more elements need to be added to the current CRN in order to properly capture the physics of a flame with highly reactive chemistry like H_2.

Nevertheless, a similar approach to that taken in Sections 5.3 and 5.7.1 to quantify which pathways are responsible for NO_X formation is also performed on this set of experiments.

The NO_X contribution from each of the four pathways in the turbulent flame brush and the recirculation zone are shown in Figure 5.37 for five varying levels of H_2: 0%, 30%, 50%, 70%, and 100%, respectively. The contribution from the prompt pathway becomes increasingly less significant as the percentage of H_2 increases in the fuel stream. Note that due to of the lack of prompt NO_X, almost all of the NO_X produced for pure H_2 combustion is made in the recirculation zone. Finally, the plot shows that the contributions from Zeldovich, NNH, and N_2O pathways increase as more H_2 is added to the fuel stream.

Figure 5.37: NO_X rate of production from each of the four pathways in the recirculation zone and turbulent flame brush for H_2 mixed with CH_4. Combustion temperature is kept constant at 1800 K.

These results are supported by looking at the computed species concentrations in each reactor. The concentrations of CH and NNH in the turbulent flame brush are shown in Figure 5.38. The concentrations of CH, NNH, and N_2O in the recirculation zone are shown in Figure 5.39. The concentrations of O and H in the recirculation zone are shown in Figure 5.40. The CH and NNH concentrations shown in Figure 5.38 support the decreasing contribution of the prompt pathway and the increasing contribution of the NNH pathway shown in Figure 5.37. It is interesting to note that the CH concentration is relatively flat until there is about 70% H_2 in the fuel stream. The decreasing prompt contribution is due to the decreasing hydrocarbon material within the turbulent flame brush as more H_2 is added to the fuel mixture. The computed N_2O concentration in the recirculation zone remains relatively flat throughout the range of H_2 in the fuel stream and the concentration of O-atom increases, but not significantly. We speculate that the increase in contributions from both the Zeldovich and N_2O pathways within the recirculation zone is largely due to a larger volume and thus longer residence time associated with the addition of H_2.
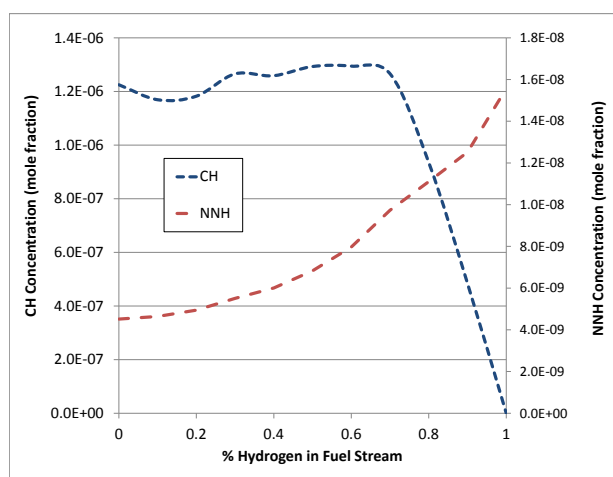
Figure 5.38: CH and NNH concentration in the turbulent flame brush for H_2 mixed with CH_4. Combustion temperature is kept constant at 1800 K.

Figure 5.39: CH, NNH, and N_2O concentration in the recirculation zone for H_2 mixed with CH_4. Combustion temperature is kept constant at 1800 K.
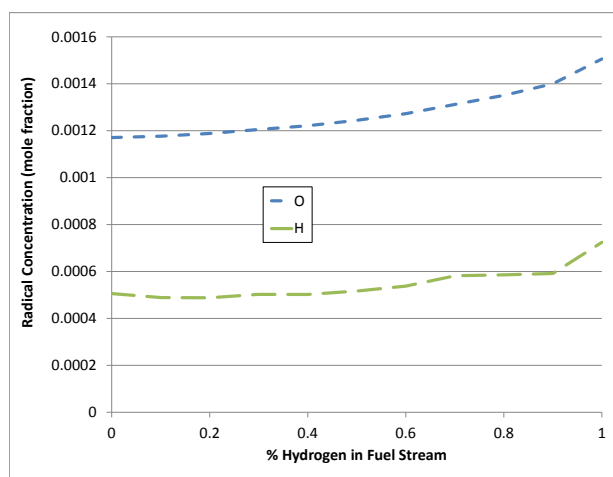
Figure 5.40: O and H concentration in the recirculation zone for H_2 mixed with CH_4. Combustion temperature is kept constant at 1800 K.

Although the CRN model developed for the JSR shows fairly good agreement with the experimental data, the configuration must most likely be modified in order to deal with fuels with increasing levels of H_2. Much of the disagreement is likely due to the

an increasingly large computed recirculation zone associated with large levels of H_2. This large recirculation zone artificially "spreads" the highly reactive H_2 chemistry over a larger volume than what is actually happening within the experiment.

As mentioned above, the CRN that has been successful in modeling CH_4 and landfill gas blends is shown to have some shortcomings when it comes to capturing the physics of H_2 combustion. The question is: how do we construct the CRN in order to capture the physics within our experimental combustor run with increasing levels of H_2? Shown below in Figure 5.7.2 are four possible CRN configurations.

CRN 1 is simply one PSR at assigned (measured) temperature encompassing the entire volume of the reactor. In CRN 2, the reactor is broken up into two volumes in series. The first volume represents the turbulent flame brush, which is modeled as an adiabatic PSR near blowout. The second volume encompasses the rest of the reactor and is modeled as a PSR at measured temperature. CRN 3 is the same configuration that was developed in Chapter 4. The flow from the jet is split with 90% flowing into the turbulent flame brush (as above modeled as an adiabatic PSR near blowout) and 10% of the flow goes into a small adiabatic PSR that is representative of a turbulent premixed strained flame or shear zone, where cold reactants strain against hot recirculated products. The contents of both of these reactors flow into the remaining reactor, which is modeled as a PSR at measured temperature representing the recirculation zone. Three-quarters of the flow leaving the recirculation zone returns to the reactor through the shear zone while one-quarter exhausts. CRN 4 is composed of two elements. The first element is modeled as a turbulent flame brush as in CRN 2 and CRN 3; however, unlike CRN 3, 10% of the jet does not flow into an element representing a turbulent strained flame. The remainder of the reactor volume is composed of a plug flow reactor, PFR, with variable heat loss that is adjusted so that the max temperature within this reactor reaches the measured temperature (1800 K). As in CRN 3, one-quarter of the flow leaving the PFR exhausts while three-quarters return to the reactor where the flow is mixed with the exhaust of the turbulent flame
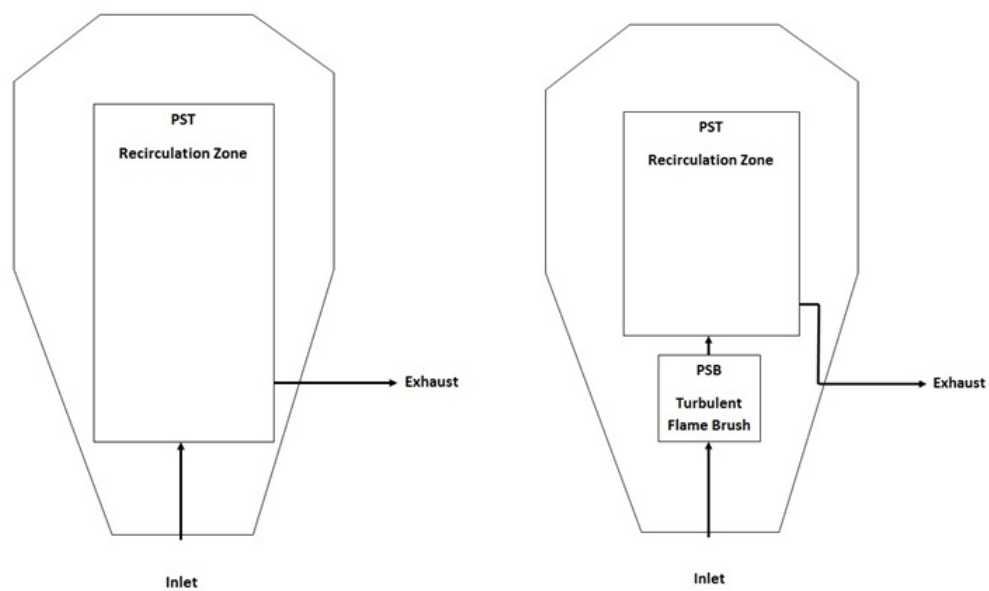
(a) CRN 1: PST

(b) CRN 2: PSB + PST
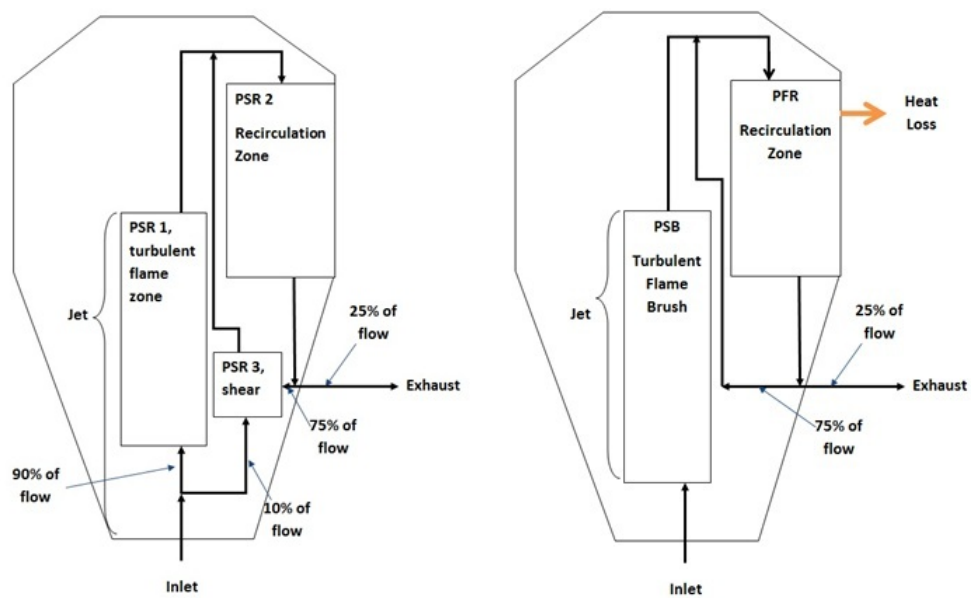
(c) CRN 3: Three-element

(d) CRN 4: PSB + Recirculating PFR

Figure 5.41: Possible CRN configurations

brush before being sent back into the PFR. The recirculating flow fraction that is applied to CRN 3 and 4 has been determined through analyzing CFD data.

The various CRN configurations show differing levels of flow complexity. The multi-zone behavior of the reactor is captured in CRN 2 through 4. The recirculating aspect of the reactor is modeled in CRN 3 and CRN 4. However, in CRN 4 a recirculating PFR with heat loss replaces the shear zone and constant temperature PSR in CRN 3. The modeling results are shown below in Figure 5.42.
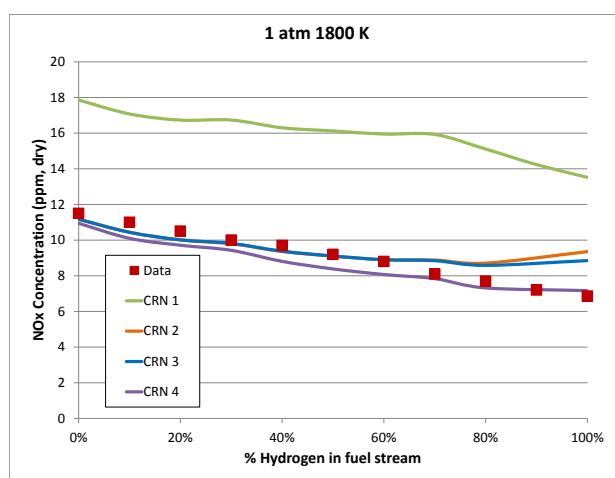
Figure 5.42: NO_X concentration as a function of H_2 concentration in the fuel stream for a fuel mixture of CH_4 and H_2. Combustion temperature is kept constant at 1800 K.

Figure 5.42 shows that CRN 1 does follow the same trend as the data but over predicts it across the entire range of fuel mixtures. Modeling the entire reactor as one PSR, artificially spreads the highly super-equilibrium flame brush over the entire volume of the reactor. Artificially spreading these large radical concentrations over the whole volume causes the model to predict an elevated amount of NO_X. There is very little difference between the predictions of CRN 2 and 3. In fact, both models predict the data fairly well up to about 80% H_2 and then they diverge from the measured NO_X. At this point, there is not a clear explanation for the model divergence when

large levels of H_2 are added to CH_4 other than the fact that H_2 is more reactive than the hydrocarbon material and modeling the recirculation zone as a homogenous PST is still spreading high radical concentrations over too much of the reactor. Note that the predictions of CRN 2 and 3 are nearly identical except CRN 3 doesn't diverge quite as dramatically nearing 100% H_2. CRN 4 does the best job of capturing the downward trend of NO_X production with increasing H_2 concentration especially after 70% H_2. This suggests the need for a PFR in the model. A PFR acts to reduce free radical levels and thus NO_X formation in the recirculation zone. Finally, note that the model predictions of fuels with high CH_4 concentration are fairly insensitive to configuration or recirculation as long as a PSR near blowout is included as the first element in the network.

5.7.3 H_2 mixed with CO

Similar to the parameter studies detailed above, for the LPM combustion of H_2 mixed with CO the air flow rate is held constant, while the flow rates of both H_2 and CO are adjusted to maintain a combustion temperature of 1800 K within the recirculation zone. Unlike the CH_4/H_2 study, the mole fraction of CO in the fuel stream is not increased past 70% by volume since this is thought to be the largest CO concentration that would be normally seen in any practical syngas that is produced in an O_2 blown gasification plant [81]. As shown in Figure 5.43, for a constant recirculation zone temperature of 1800 K the NO_X concentration decreases with increasing H_2 concentration in the fuel stream.
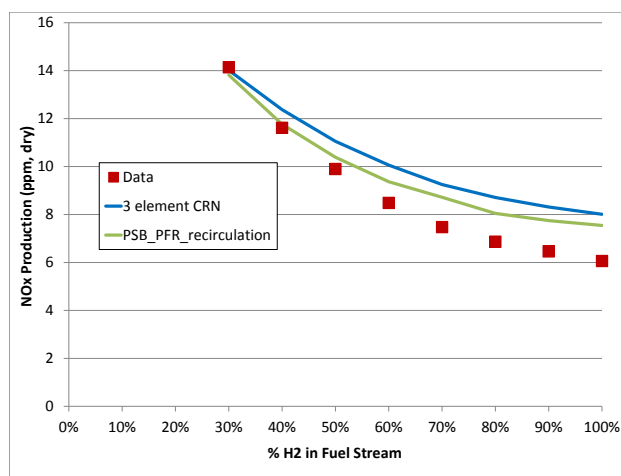
Figure 5.43: NO$_X$ concentration as a function of H$_2$ concentration in the fuel stream for a fuel mixture of H$_2$ and CO. Combustion temperature is kept constant at 1800 K.

Again, the 3-element CRN illustrated in Chapter 4 (CRN 3 in Section 5.7.2) is employed to model the data. The model follows the general trend of the data; however, for large H$_2$ levels the model over predicts the data, and becomes gradually better as the concentration of CO in the fuel stream increases. This discrepancy is most likely due to the same reason that the predictions diverge from the measurements for the CH$_4$/H$_2$ fuel blends. The CRN composed of a PSB with a recirculating PFR (CRN 4 in Section 5.7.2) does a better job at predicting the data at high H$_2$ concentrations.

The breakdown between NO$_X$ produced in both the turbulent flame brush and the recirculation zone is shown below in Figure 5.44 employing CRN 4 from Section 5.7.2.
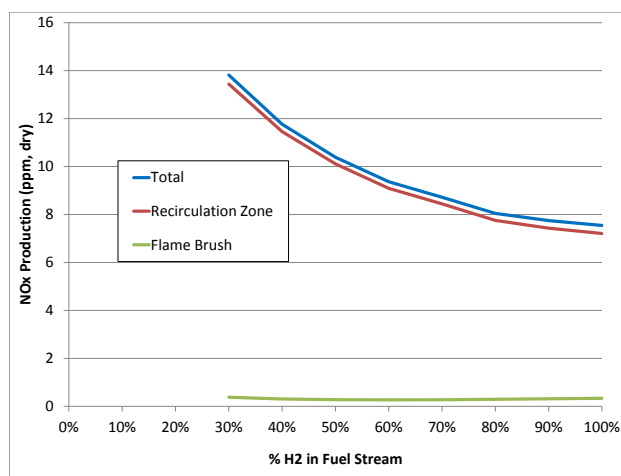
Figure 5.44: NO$_X$ production reported as a function of H$_2$ concentration in the fuel stream in the turbulent flame brush and the recirculation zone. Combustion temperature is kept constant at 1800 K.

The plot shows that the turbulent flame brush produces very little NO$_X$. Figure 5.45 shows the breakdown of NO$_X$ production as a function of H$_2$ concentration in the fuel stream for each of the NO$_X$ formation pathways in the entire reactor, which in this case is essentially the formation from within the recirculation zone. It should also be noted that the prompt pathway has been removed from consideration since there is no hydrocarbon component of this mixture.
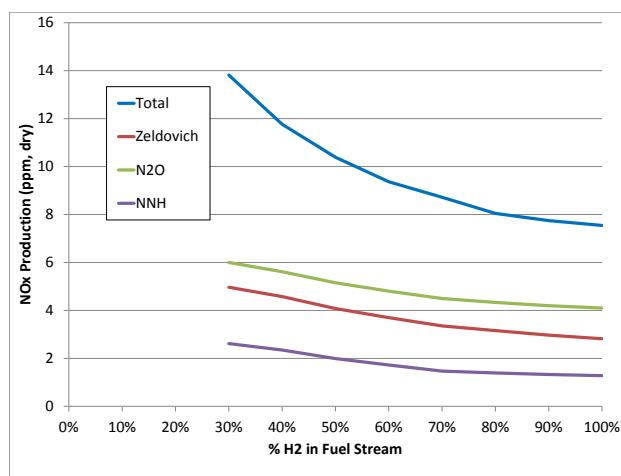
Figure 5.45: NO$_X$ production reported as a function of H$_2$ concentration in the fuel stream for each NO$_X$ formation pathway in the entire reactor. Combustion temperature is kept constant at 1800 K.

This plot clearly shows that the N$_2$O pathway is the highest producer followed by Zeldovich and NNH. Also, as the CO concentration in the fuel stream increases the production from all three mechanisms increases. These trends are supported by looking at the radical concentrations as a function of H$_2$ concentration as shown in Figure 5.46.
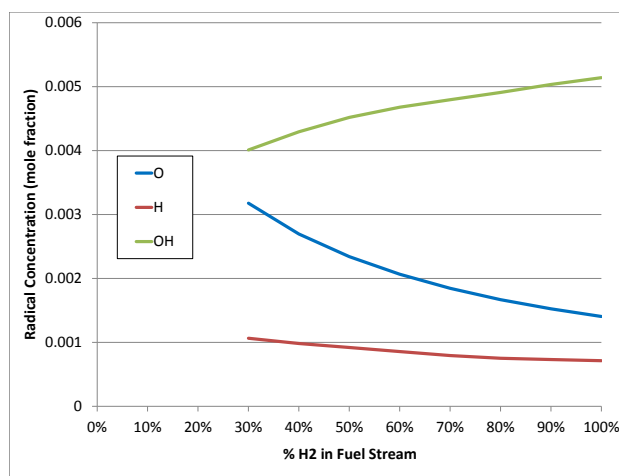
Figure 5.46: Radical concentrations in the recirculation zone reported as a function of H_2 concentration in the fuel stream. Combustion temperature is kept constant at 1800 K.

As expected, the OH concentration falls as the CO concentration in the fuel stream increases. This is an effect of the increased reactivity of the major CO oxidation step: $CO + OH \Leftrightarrow CO_2 + H$. Following the same rationale, the H concentration increases as CO fuel fraction increases. An increase in H concentration increases the production of the NNH pathway and an increase in O concentration increases NO_X production from both the N_2O and Zeldovich pathways.

5.7.4 CH_4 mixed with CO

Although, CH_4 mixed with CO is not one of the fuel blends outlined in Table 1.1, CO is one of the main components of reformed natural gas; thus it is of general interest to study the effect it has on NO_X emissions when blended into a stream of CH_4. Similar to the experiments described above, the air flow rate is held constant, while the flow rates of both CH_4 and CO are adjusted to maintain a combustion temperature of 1800 K within the recirculation zone. As shown in Figure 5.47, for a constant recirculation zone temperature of 1800 K the addition of CO causes the NO_X emissions to remain

relatively flat until about 60% CO, following which the emissions begin to rise steeply. The model captures the data fairly well, it predicts a small initial decrease in emissions before capturing the final rise with larger CO concentration in the fuel stream.
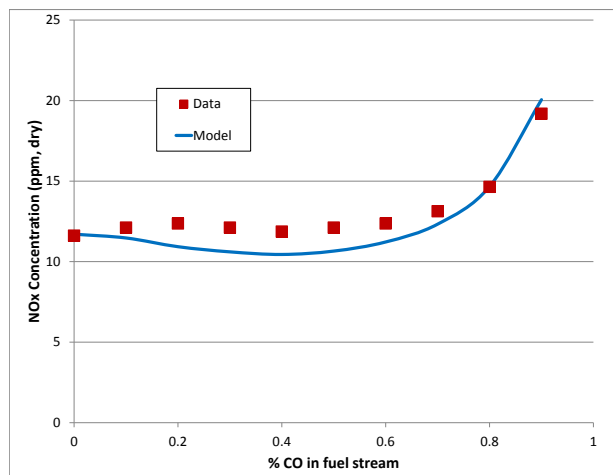
Figure 5.47: NO_X concentration as a function of CO concentration in the fuel stream for a fuel mixture of CH_4 and CO. Combustion temperature is kept constant at 1800 K.

The contribution from each of the four pathways in the turbulent flame brush and the recirculation zone are shown in Figure 5.48 for five varying levels of CO: 0%, 30%, 50%, 70%, and 90%, respectively. The prompt pathway decreases in significance as the CO concentration increases in the fuel stream, since CO combustion does not produce CH. Also, similar to the CH_4/H_2 mixture, fuels with decreasing CH_4 percentage do not produce much NO_X within the flame brush. Although the contribution from the prompt pathway decreases as CO is added, the contributions of the other three pathways increase significantly. This is supported by looking at the radical concentrations within the recirculation zone as shown in Figure 5.49.
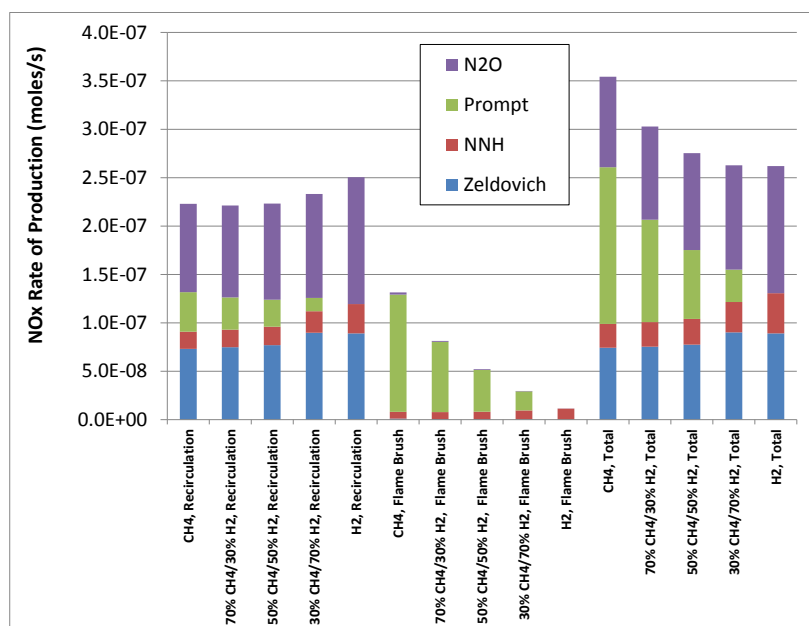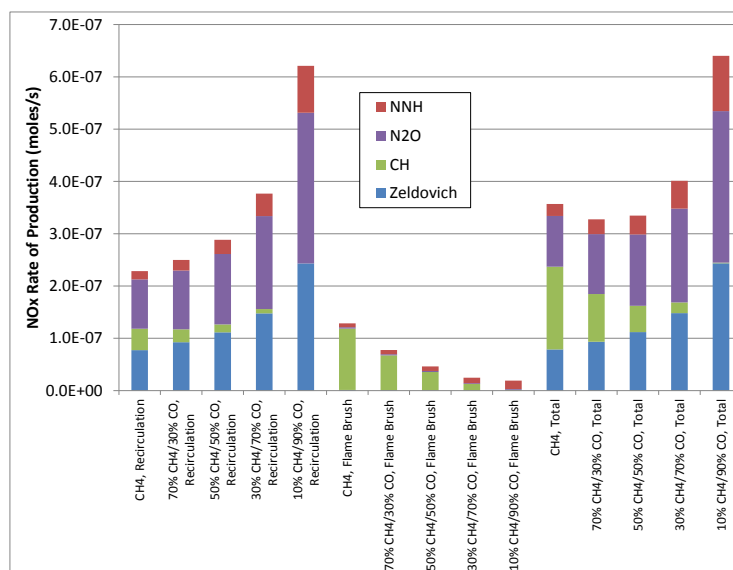
Figure 5.48: NO$_X$ rate of production from each of the four pathways in the recirculation zone and turbulent flame brush for CH$_4$ mixed with CO. Combustion temperature is kept constant at 1800 K.
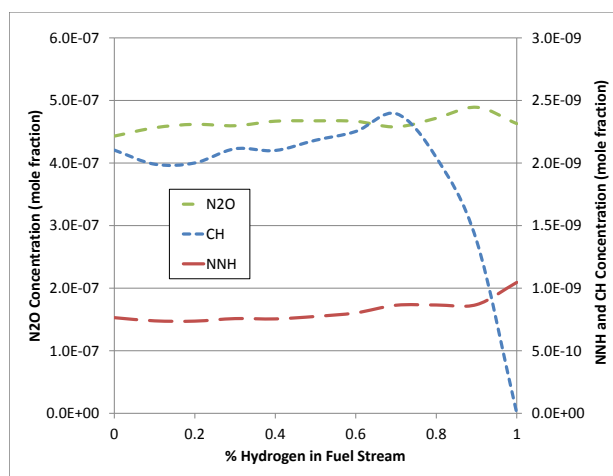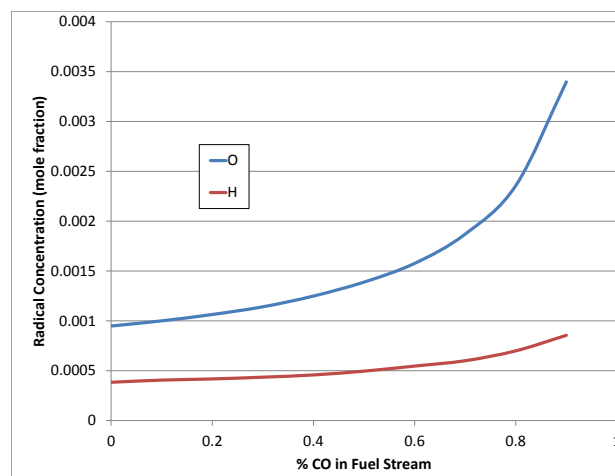

Figure 5.49: O and H concentration in the recirculation zone for CO mixed with CH$_4$. Combustion temperature is kept constant at 1800 K.

CO is a large promoter of radical chain branching, in particular when normalized

to the heating value it brings to the combustor. A large CO concentration increases the forward rate of the key CO oxidation reaction: $CO + OH \Leftrightarrow CO_2 + H$. This effectively increases the H radical pool, which in turn increases the O radical pool due to the prolific reaction $H + O_2 \Leftrightarrow O + OH$. The increase of both O and H radicals promotes NO_X formation via the NNH, N_2O and Zeldovich pathways.

5.7.5 CH_4 mixed with C_2H_6

For the LPM combustion of C_2H_6 mixed with CH_4, the air flow rate is held constant, while the flow rates of both CH_4 and C_2H_6 are adjusted to maintain a combustion temperature of 1800 K within the recirculation zone. As mentioned in Section 5.5, the authors of GRI-Mech 3.0 caution against using the mechanism with fuel mixtures composed of large concentrations of C_2 and C_3 hydrocarbons. Despite this caution, GRI-Mech 3.0 is used in the CRN developed in Chapter 4. In addition, the C_2-NOx mechanism developed by Reaction Design is used in the same CRN. It is found that the C_2-NOx mechanism shows some unstable numerical behavior near blowout. The computed blowout volumes for the first PSR in the 3-element CRN from using both GRI-Mech 3.0 and C_2-NOx are shown below in Figure 5.50. Since the solution computed for the PSB appears to be questionable, it is decided to test the C2-NOx mechanism in conjunction with the PSB volumes computed by GRI-Mech 3.0. The results from all three models are shown below in Figure 5.51.   Figure 5.51 shows that the experimental NO_X concentration rises as the C_2H_6 concentration in the fuel increases. The results of the model with GRI-Mech 3.0 show a very slight increase in emissions with increasing C_2H_6 concentration. The model predictions from the C_2-NOx mechanism with the PSB volume computed using the C_2-NOx mechanism show a rise going from pure CH_4 to pure C_2H_6; however, the model does not show a smooth trend, which is most likely due to the unstable behavior of the model near blowout. The model predictions of the C_2-NOx mechanism using the PSB volumes computed by GRI-Mech 3.0 show the best trend with the data. The curve is smooth,
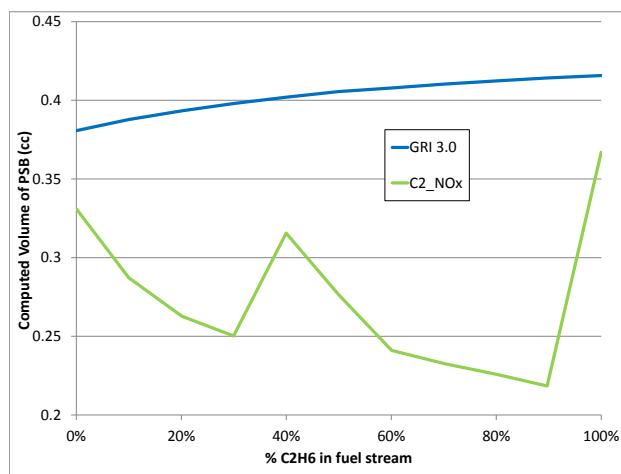
Figure 5.50: The volumes computed for the PSB as a function of C_2H_6 concentration in the fuel stream for a fuel mixture of CH_4 and C_2H_6 from both GRI-Mech 3.0 and C2-NOx. Temperature in the recirculation zone is kept constant at 1800 K.
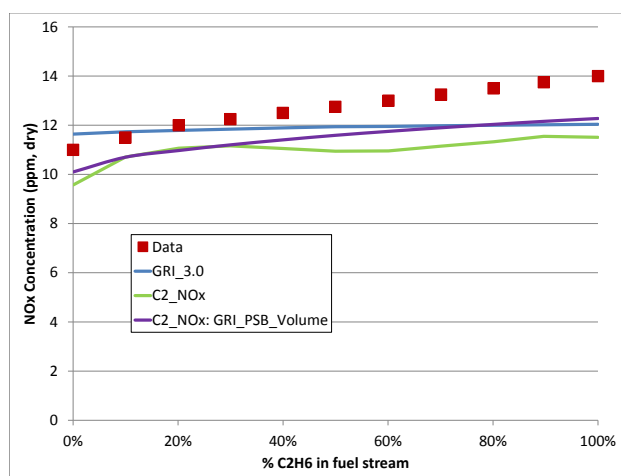
Figure 5.51: NO_X concentration as a function of C_2H_6 concentration in the fuel stream for a fuel mixture of CH_4 and C_2H_6 from experiment and the three element CRN. Temperature in the recirculation zone is kept constant at 1800 K.

which can most likely be attributed to a smooth prediction of PSB volume and the corresponding temperature that goes along with this volume. However, this model under-predicts the NO_X data by 1-2 ppm, though it doea follow the proper trend with respect to C_2H_6 percentage. Since neither mechanism predicts the data very well and the C_2-NOx mechanism does not contain the same oxidation chemistry as GRI-Mech 3.0, a pathway breakdown analysis as outlined in Section 5.3 is not performed. Further work must be put into developing a chemical mechanism that can accurately model the oxidation of C_2 and C_3 hydrocarbons with NO_X formation is clearly indicated.

5.8 NOx Entitlement

As stated in Section 1.4, one of the goals of this research is to develop a set of of Gaseous Fuel Interchangeability Criteria or a methodology to help manufacturers develop and predict the outcome when an alternative fuel to natural gas is used. One of the underlying concepts of the interchangeability criteria from an emissions standpoint is: what fuel or combustor geometry makes the lowest NO_X possible, while still preserving system efficiency?

In 1994, Leonard and Stegmaier published a seminal work addressing this issue for an aeroderivative gas turbine fueled with LPM natural gas [82]. In the paper they present a basic overview of their design of the premixed system, but they mainly discuss the results of their testing. Their study encompasses a wide ranging parameter space including inlet temperatures between 300 and 800 K, operating pressures between 1 and 30 bar, and combustor residence times between 2 and 100 ms. From their tests they concluded that when operating at flame temperatures less than 1900 K, NO_X production is not influenced by inlet temperature, operating pressure, or residence time. The emissions are only influenced by the degree to which the reactants are mixed with emissions increasing with less homogeneous levels of premix. With these findings, they have essentially set an emissions floor that has come to be viewed as the lower limit achievable for practical combustion systems. This is the

lower limit that combustion system designers strive to reach. This floor in NO_X has been termed an entitlement. As mentioned above, they burned natural gas in their combustor. The question now is: what happens if other fuels are burned in its place? Experimental data taken from the 16 cc JSR, a 64 cc JSR of similar geometry, and the correlation adapted from the Leonard and Stegmaier paper is shown in Figure 5.52.
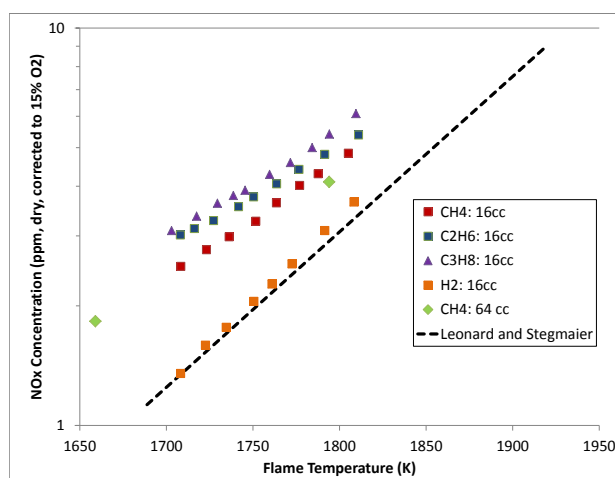
Figure 5.52: NO_X emissions data taken at various temperatures in the JSR and a curve representing the Leonard and Stegmaier data as a function of flame temperature.

The Leonard and Stegmaier data are plotted against adiabatic flame temperature, while the JSR data are plotted against measured flame temperature. The 16cc atmospheric pressure JSR loses a significant amount of heat; thus to maintain a measured flame temperature of 1800 K the equivalence ratio must be increased well above the stoichiometry required to achieve an adiabatic flame temperature of 1800 K. The non-adiabaticity of the present 16cc JSR leads to NO_X for hydrocarbon fuels above the L-S correlation. In earlier research with a high pressure, nearly adiabatic 2cc JSR fired on CH_4, Steele [54] found the JSR-measured NO_X to agree well with the L-S correlation, i.e. Steele's data fell slightly above the L-S line. The NO_X data from LPM CH_4 combustion taken from the 64 cc reactor still lies above the L-S curve, but

not as far as the data taken in the 16cc reactor. This reactor has a smaller surface to volume ratio; thus, the reactor losses less heat and requires a lower equivalence ratio to maintain the same temperature within the recirculation zone.

Figure 5.52 shows NO_X from H_2 combustion in the present 16cc JSR agreeing very closely with the L-S line. It is interesting to explore this finding and well as further explore the behavior for the hydrocarbon fuels. The combustor that was used by Leonard and Stegmaier was a high throughput commercial combustor. They plot their data against adiabatic flame temperature instead of measured temperature, which is a good assumption since their combustor is quite close to adiabatic. The fact that the NO_X emission data from the JSR fall on the Leonard and Stegmaier curve for H_2 combustion and lie above the curve for combustion of hydrocarbon fuels may be attributable to the large heat loss in the experimental JSR. We address this issue below.

5.8.1 Reactor Heat Loss

As reported in Section 1.2.2, there is considerable inconsistency reported in the literature regarding whether replacing H_2 for CH_4 in an LPM flame at constant temperature increases, decreases, or does not affect NO_X formation. Shown above in Section 5.7.2, CH_4 produces more NO_X than H_2 when burned at constant measured temperature in our experimental JSR. Figure 5.53 shows various data sets taken from some of the references discussed in Section 1.2.2. The experimental conditions for the data shown in Figure 5.53 are displayed in Table 5.4.

There are other data in the literature; however, we limited the plot to only H_2/CH_4 blends, or H_2/CH_4 blends with very low concentrations of CO. As shown in Sections 5.7.3 and 5.7.4, CO strongly affects NO_X production through its intense chain branching.

The NO_X trend with H_2 addition appears to depend on the experimental configuration. The combustor used by Delattin et al. [19] is only slightly larger than
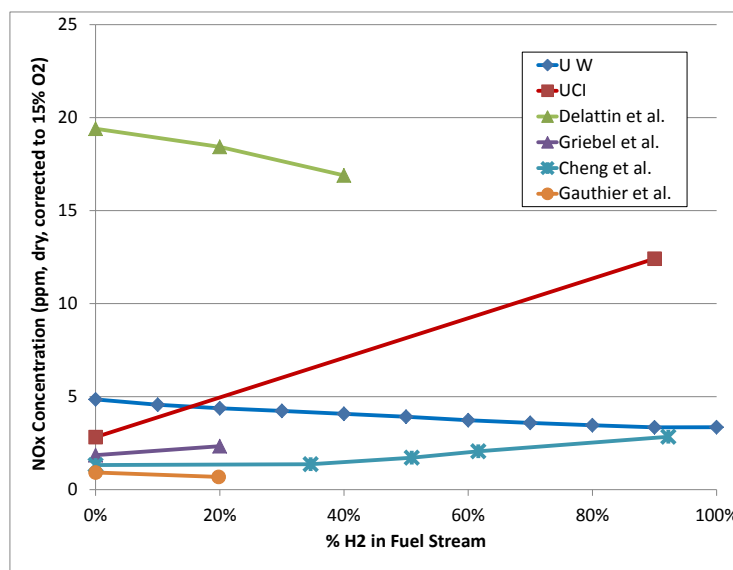
Figure 5.53: Various data showing the effect that H_2 has on NO_X formation in a LPM CH_4 flame at constant temperature. References are given in Table 5.4.

ours and is run at 1 atm, which would definitely promote significant heat loss. The ceramic burners are high heat loss devices (Gauthier et al. [23]). High throughput combustors run at elevated pressure like the dump combustor at UCI [29], Griebel's [33], and the combustor at NETL [28] can be assumed to be very close to adiabatic. Thus, it appears that the burners with higher heat loss tend to yield lower NO_X when replacing CH_4 with H_2, while the more adiabatic burners tend to increase NO_X as H_2 is increased.

As discussed previously, the JSR experiments are generally run to obtain a measured flame temperature of 1800 K in the recirculation zone. The heat loss in the JSR is typically 20% relative to the lower heating value of the input fuel. This means that to achieve 1800 K measured temperature in the JSR the stoichiometry needs to be more fuel rich, and at a higher adiabatic flame temperature than it would need to be if the reactor had no heat loss. A larger or high pressure combustor with little heat loss will run significantly leaner than the JSR to achieve an 1800 K temperature. We

Table 5.4: A summary of experimental conditions for the data shown in Figure 5.53.

Researcher	Experiment	AFT (K)	Measured Flame Temperature (K)	Components other than H_2 and CH_4
U of W [83]	Backmixed JSR at 1 atm (High heat loss)	2039 - 2046 with increasing %H_2	1800	No
UCI [29]	Flare quarl combustor at 3 atm fed with a low swirl injector	1816 - 1822 with increasing %H_2	NA	No
Delattin et al. [19]	Dump combustor at 1 atm fed with a high swirl injector	2029 - 2056 with increasing %H_2	NA	Yes, very small percentages of CO, CO_2, and N_2 (CO < 3% of fuel)
Griebel et al. [33]	Generic turbulent jet burner at 5 bar	1816 - 1811 with increasing %H_2	NA	No
Cheng et al. [28]	Industrial scale dump combustor at 4 atm fed with a low swirl injector	1702 - 1704 with increasing %H_2	NA	No
Gauthier et al. [23]	Porous ceramic burner at 1 atm	1999 - 2009 with increasing %H_2	NA	No

suggest that this difference in equivalence ratio is what leads to the differences in the NO_X emissions trends with CH_4 versus H_2.

Figure 5.54 shows the results of a numerical experiment in which a PSR is set to run at 1800 K and 3 ms, but with the heat loss from the reactor being varied. At high heat loss, the reactor must be run closer to stoichiometric to achieve the 1800 K temperature. At the zero heat loss, adiabatic 1800 K condition, H_2 produces somewhat more NO_X than CH_4. At high heat loss, but still at 1800 K, CH_4 produces more NO_X. The reason for this trend appears in Figure 5.55, which shows the contribution of the various NO_X formation mechanisms for the two fuels: H_2 vs. CH_4, both at adiabatic vs. 20% heat loss.
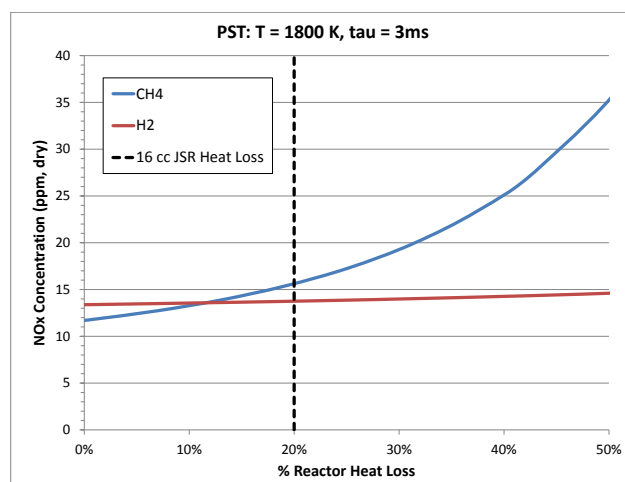
Figure 5.54: The effect of increasing heat loss/ϕ has on NO_X emissions for LPM H_2 and CH_4 combustion. T = 1800 K.
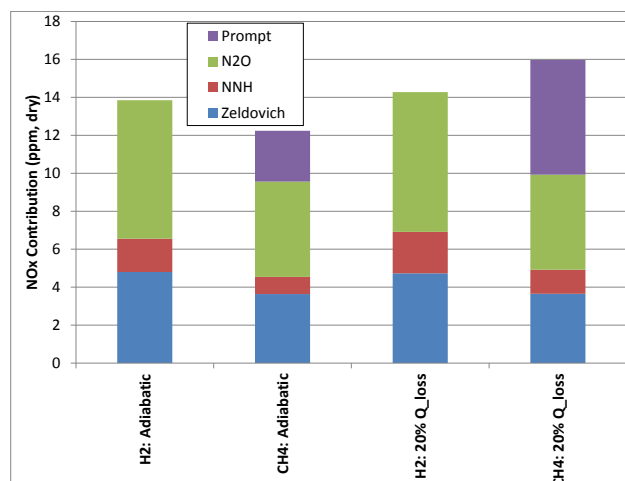
Figure 5.55: Contribution from each pathway to total NO_X production for LPM H_2 and CH_4 at a temperature of 1800 K for both 0 and 20% heat loss.

While the contribution from the Zeldovich and N_2O pathways remain relatively constant when the equivalence ratio is increased at constant temperature, the prompt pathway becomes much important under high heat loss/richer conditions. Although

the NNH contribution to NO_X also increases with heat loss/richer conditions, its overall contribution is secondary. The effect of heat loss on other mixtures is shown in Figure 5.56 with the specific compositions shown in Table 5.5.

Table 5.5: Composition of Fuels shown in Figure 5.56.

Mix	H_2	CH_4	CO_2	CO	N_2
1	1	0	0	0	0
3	0.4	0	0.1	0.5	0
4	0	0.5	0.35	0	0.15
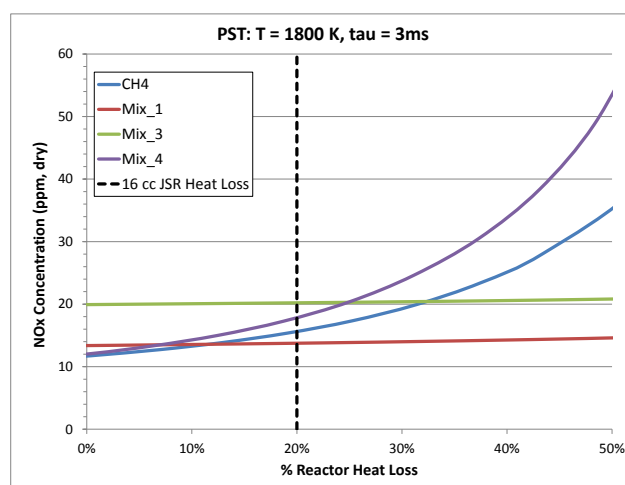
Figure 5.56: The effect of increasing heat loss/ϕ has on NO_X emissions for other mixtures in our study. T = 1800 K.

The effect of the prompt mechanism is also experienced with the landfill blend, showing the same trend here as shown in Section 5.7.1. Mix 3 looks similar to H_2 combustion, because of the absence of the prompt mechanism. From Sections 5.7.3 and 5.7.4, it is not surprising that the syngas produces more NO_X than the other mixes, because CO appears to produce more radicals per unit heat release than the other fuels. The N_2O, Zeldovich and NNH pathways become large contributors when

the CO concentration of a fuel is increased because of the enhanced amounts of O and H-atoms.

Thus, we suggest that the general trend can be explained by whether the prompt mechanism is a significant contributor. In near-adiabatic combustors, the stoichiometry is sufficiently lean that prompt is a relatively small contributor, and the replacement of CH_4 by H_2 leads to no change or an increase in NO_X. For those systems with high heat loss, prompt is a major contributor to NO_X in CH_4 flames, and replacing the CH_4 with H_2 leads to loss of the prompt mechanism and thus a reduction in NO_X emissions.

5.8.2   CRN Configuration in Regards to NOx Entitlement

The issue of entitlement has come up often. In an attempt to address this issue, a simple adiabatic Bragg cell (PSR + PFR) is run for both LPM H_2 and CH_4 combustion at adiabatic flame temperatures (AFT) of 1550, 1800, and 2100 K. The effect that the size of the PSR has on the overall NO_X prediction is shown below in Figures 5.57, 5.58, 5.59. On the left hand side of each curve plotted, the PSR is at its blowout volume. On the right hand side of each curve, the PSR encompasses the entire combustor volume (there is no PFR).
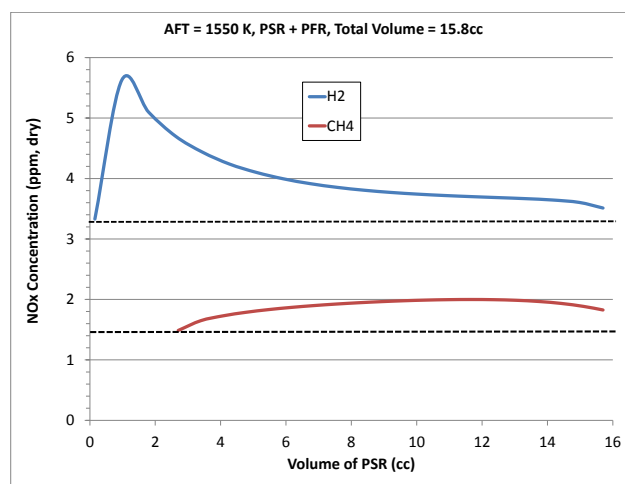
Figure 5.57: The effect that the PSR volume has on NO_X predictions in an adiabatic Bragg cell. AFT for both fuels is 1550 K. The NO_X is reported for the exit of the Bragg cell.
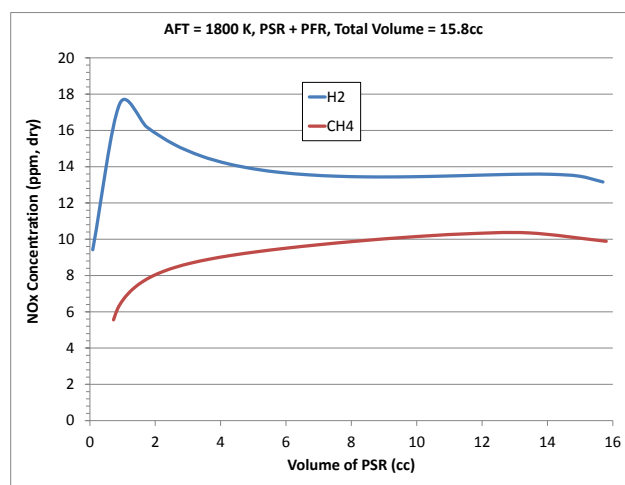
Figure 5.58: The effect that the PSR volume has on NO_X predictions in an adiabatic Bragg cell. AFT for both fuels is 1800 K. The NO_X is reported for the exit of the Bragg cell.
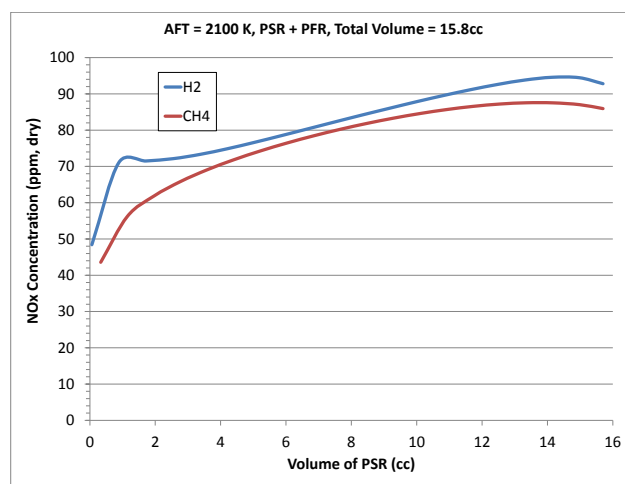
Figure 5.59: The effect that the PSR volume has on NO_X predictions in an adiabatic Bragg cell. AFT for both fuels is 2100 K. The NO_X is reported for the exit of the Bragg cell.

Using Figure 5.57 as an example, H_2 emissions at blowout are small, and they increase because of a large increase in the product of radicals and residence time in the PSR as it relaxes from the blowout point. This is important because the radicals decay quickly after the PSR.

It appears the reason for the peak in NO_X for H_2 combustion is an increase in free radical levels as the flame zone is initially allowed to grow from the blowout point. Figure 5.60 shows the O atom concentration in the PSR as it encompasses more of the combustor volume for an adiabatic flame temperature of 1800 K.
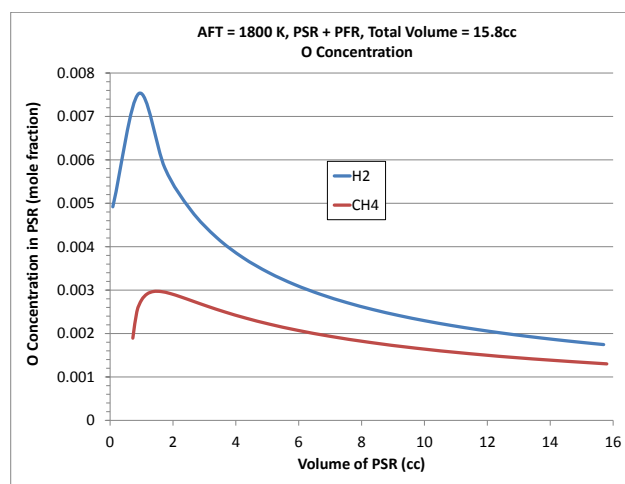
Figure 5.60: Predicted O atom concentration in the PSR as its volume is increased for both LPM H_2 and CH_4 combustion at an AFT of 1800 K.

As the size of the PSR initially increases from the blowout condition, the O atom begins rising sharply for both CH_4 and H_2; however, it is a far more dramatic increase for H_2. By the time the PSR has encompassed the entire combustor, the O concentration from the combustion of both fuels has relaxed considerably. The O-atom rises initially as the flow enters the PFR and then falls significantly as the residence time increases. Figure 5.61 shows the computed O atom concentration vs. residence time in the PFR corresponding to the Bragg cell with the smallest PSR volume (a PSR at the blowout condition).
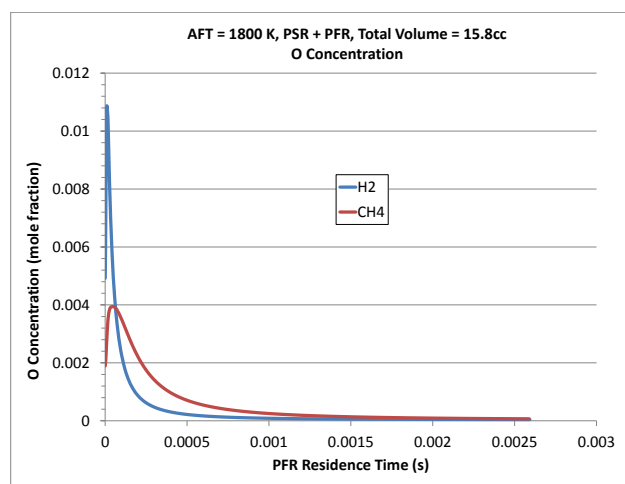
Figure 5.61: Predicted O atom concentration vs. PFR residence time corresponding to the Bragg cell configuration with a PSR sized at blowout for both LPM H_2 and CH_4 combustion at an AFT of 1800 K.

The O atom spike for H_2 combustion in the beginning stages of the PFR is almost an order of magnitude larger than for CH_4 combustion and relaxes far quicker. The O atom spike for CH_4 combustion is most likely broader because of the CO intermediate, which is absent from H_2 combustion. As CO oxidizes, it produces O and H. Figure 5.62 shows NO_X concentration in the PFR vs. residence time. Noting the large sharp O atom spike for H_2 combustion in Figure 5.61, it is not surprising that nearly all of the NO_X made in the Bragg cell combustor is made very early on in the PFR. For H_2 combustion, the PSR at blowout doesn't have a long enough residence time to make a significant amount of NO_X. For CH_4 combustion, the PSR at blowout does have a long enough residence time to make NO_X and is impacted by prompt NO_X as shown throughout this chapter. Once in the PFR, the rate of NO_X production for CH_4 combustion is far slower than for H_2 combustion, most likely due to smaller initial bloom of free radicals.
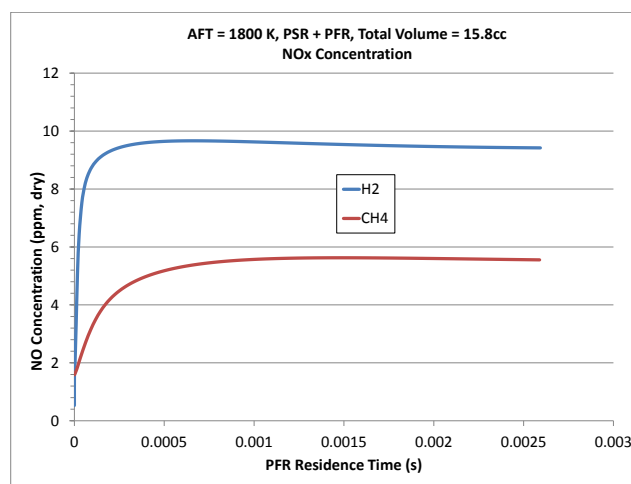
Figure 5.62: Predicted NO$_X$ concentration vs. PFR residence time corresponding to the Bragg cell configuration with a PSR sized at blowout for both LPM H$_2$ and CH$_4$ combustion at an AFT of 1800 K.

The following points can be made about Figures 5.57 through 5.59.

1. At adiabatic conditions H$_2$ makes more NO$_X$ than CH$_4$ independent of the PSR volume (because the prompt mechanism is largely absent).

2. It is interesting to note that the difference between running with a small flame zone/long burn out (PSB + PFR) to running a long lazy flame encompassing the entire combustor (PSR) is the smallest at the lowest temperature.

3. The percentage increase in NO$_X$ emissions between H$_2$ and CH$_4$ is the largest at the lowest temperature. This is most likely due to the fact that the Zeldovich contribution starts to dominate at higher temperatures, which lessens the importance of the other NO$_X$ formation pathways.

4. The best configuration for low NO$_X$ emissions for both H$_2$ and CH$_4$ combustion is a PSR at blowout followed by a PFR. This would imply that it is best to construct a combustor with the smallest flame zone possible.

5. For H_2 combustion, the NO_X emissions rise sharply as the flame zone is initially increased, then they fall off as the flame zone gets larger still. This has two additional implications:

   (a) It may be wise to design combustors burning fuels with high H_2 concentrations to have long lazy flame zones to avoid the peak.

   (b) This peak may be the reason that some researchers with adiabatic combustors see more of a discrepancy in NO_X emissions between H_2 and CH_4 than others.

Chapter 6

CFD MODELLING

This chapter presents results of both two and three dimensional CFD simulations to illustrate the general flow, temperature, and species structure within the reactor. We present CFD results from the LPM combustion of pure H_2, H_2/CO, and pure CH_4. The simulations are run employing chemical mechanisms of increasing levels of complexity.

The computational grid, heat transfer, and turbulence models discussed in Chapter 4 are employed for all models presented in this chapter.

The temperature, flow and major species contours from the two and three dimensional CFD model with simple global chemistry discussed in Chapter 4 are used to initialize all models employing more detailed chemistry. The results shown in this section come reasonably close to experimental measurements; however, there are still many difficulties and concerns to be solved with the models. The most notable issues have to do with the fluid to solid heat transfer coupling, unrealistic reaction rates within the boundary layer, and the ability to handle regions of low Damköhler number.

6.1   The Eddy Dissipation Concept

The chemistry within the reactor is modelled using the Eddy-Dissipation-Concept (EDC) model [84]. The EDC model is an extension of the Eddy-Dissipation-Model that can employ detailed chemistry in turbulent reacting flows [85].

The EDC model assumes that reaction occurs in turbulent structures called fine scales. The volume fraction of these structures is shown below in Equation 6.1, where

γ^* is the length of the fine scales, C_γ is the volume fraction constant, ν is the kinematic viscosity, ε is the turbulent dissipation rate, and k is the turbulent kinetic energy.

$$(\gamma^*)^3 = (C_\gamma)^3 \left(\frac{\nu\varepsilon}{k^2}\right)^{3/4} \tag{6.1}$$

Reaction is supposed to take place within the fine structures over a time scale, τ^*, which is proportional to the Kolmogorov time scale as shown in Equation 6.2, where C_t is the time scale constant. Both the time and volume fraction constants have been determined through energy cascade arguments [86].

$$\tau^* = C_t \left(\frac{\nu}{\varepsilon}\right)^{1/2} \tag{6.2}$$

The species mass fraction in the fine scales, Y_i^*, is the solution of a constant pressure, adiabatic PSR run at a residence time of τ^*. The averaged species mass fraction for a computational cell is shown in Equation 6.3, where, Y_i^o is the species mass fraction in the surrounding fluid.

$$\tilde{Y}_i = (\gamma^*)^3 Y_i^* + (1 - (\gamma^*)^3) Y_i^o \tag{6.3}$$

In Fluent, the species reaction rate with cell averaged values is calculated as shown in Equation 6.4, where $\tilde{\rho}$ is the averaged cell density.

$$\tilde{R}_i = \frac{\tilde{\rho}(\gamma^*)^2}{\tau^*[1 - (\gamma^*)^3]}(Y_i^* - Y_i^o) \tag{6.4}$$

Note that when $(\gamma^*)^3$ gets large, i.e. approaches unity, the solution to Equations 6.3 and 6.4 approach the EDC reaction rate limit. The above equations are derived assuming that the reaction only takes place in the fine scales with the surrounding fluid being chemically inert. For reacting systems with low Damköhler Numbers, the reactions in the surrounding fluid may become important and these rates will need to be added to the reaction rates computed by Equation 6.4 [87]. This approach for low Da combustion is however not implemented in Fluent.

In addition to concern with low Da systems, the EDC model has some problems near the wall. As shown in Karalus et al. [60], k goes to zero within the boundary layer. This causes the volume fraction, $(\gamma^*)^3$, to increase. As the calculation moves into the viscous sublayer, the volume fraction of fine scales quickly becomes larger than 1, which is not physical. In fact, the length fraction of fine scales, γ^*, is limited to 0.75. Although limiting γ^* to 0.75 puts somewhat of a limit on how high the reaction rate can go, the value of τ^* is unregulated. For certain flow conditions like the stagnation point at the top of the reactor, τ^* does get quite small as the flow approaches the wall (ε gets large). Figure 6.1 shows a plot of $1/\tau^*$ from the reactor inlet to the stagnation point along centerline. This value is proportional to the reaction rate given in Equation 6.4 and is shown to increase almost an order of magnitude in about 1 mm as the jet moves close to the top of the reactor.
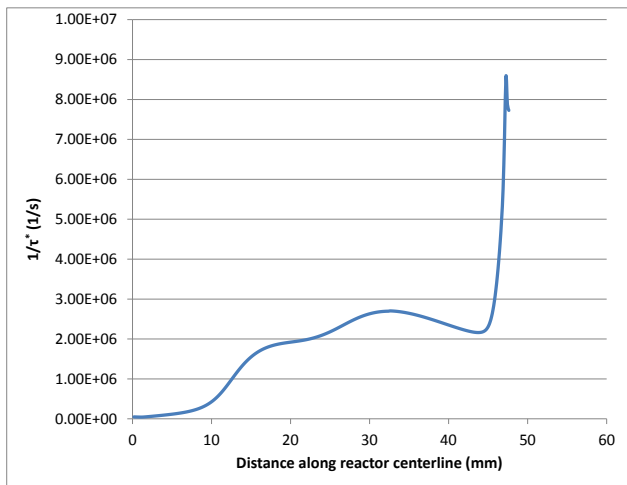
Figure 6.1: $1/\tau^*$ from reactor inlet to ceiling.

Since the EDC model is shown to breakdown in the boundary layer, a User Defined Function (UDF) is employed that eliminates all reactions in the [60]. This boundary layer thickness is defined by a turbulent Reynolds number less than 200 as shown below in Equation 6.5 [65].

$$\mathrm{Re}_y = \frac{\rho \, y \sqrt{k}}{\mu} \le 200 \tag{6.5}$$

This UDF does slightly affect the solution, especially for slow reacting species. Fast reacting species that are consumed before reaching the wall are unaffected by the UDF. For example, the net reaction rates for LPM H_2 and CH_4 are shown below in Figures 6.2 and 6.3.

(a) Without UDF   (b) With UDF
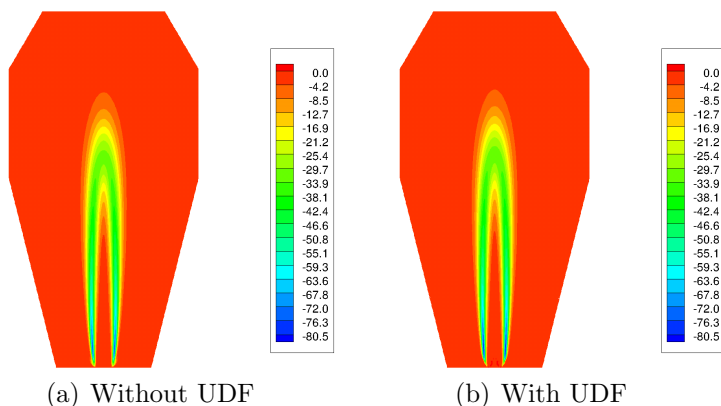
Figure 6.2: H_2 combustion, T = 1800 K. H_2 rate of destruction (kg/m^3-s)

(a) Without UDF.   (b) With UDF
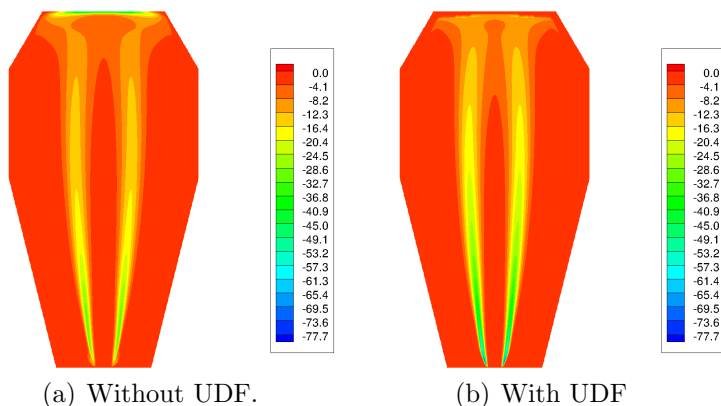
Figure 6.3: CH_4 combustion, T = 1800 K. CH_4 rate of destruction (kg/m^3-s)

Clearly there is little difference in the computed reaction rates for fast reacting

species such as H_2. There is, however, a difference in the computed reaction rates for slower reacting species such as CH_4. In the following sections, we show that the UDF allows some unreacted radicals to flow around through the boundary layer and re-entrain into the jet. This affects the reaction rates of various species; especially species that react over a long time constant. The UDF shifts the geometric positions and maximum values of radical pools, and causes more radicals to be available for entrainment into the jet. However, the varying reaction rates and radical pool locations do not affect the computed values of temperature, NO_X, and CO to a large degree. All of this will be quantified in the following sections.

6.2 H_2 Combustion

The following section describes results from both two and three dimensional CFD simulations that model H_2 combustion with full NO_X chemistry. Since the prompt NO_X mechanism is absent from H_2 combustion, modeling full NO_X chemistry is feasible in both the two and three dimensional models because the mechanism is relatively small. In the following CFD results, the GRI 3.0 mechanism [73] is used without any C containing species. As shown in Section 5.7.2, NO_X formation from H_2 combustion is strongly affected by the NNH pathway. The modification proposed by Konnov [78] has been applied to GRI-Mech 3.0 for this simulation as well, changing the activation energy of $NNH + O \Leftrightarrow NO + NH$ from 0 to 4 kcal/mole. The H_2 oxidation mechanism with NO_X formation is composed of 18 species with 69 reactions.

Although a 3D solution is tractable with a convergence time of about 10 days, the 2D model runs far faster and converges in only 1-2 days. The radial temperature and NO_X predictions are shown for both the two and three dimensional models in Figures 6.4 and 6.5.
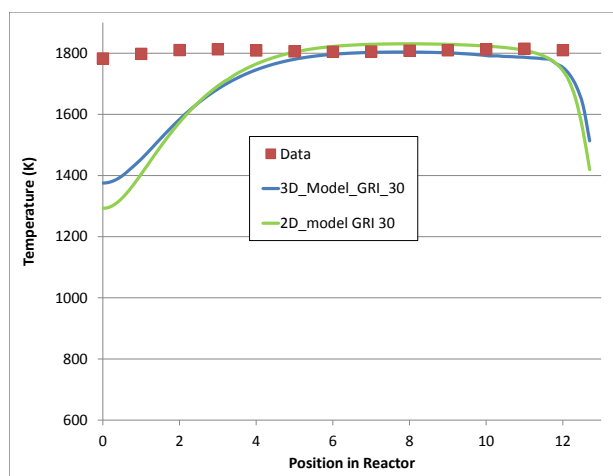
Figure 6.4: Profile of temperature from reactor centerline to wall, measured and predicted by CFD for H_2 combustion with NO_X formation chemistry in two and three dimensions.
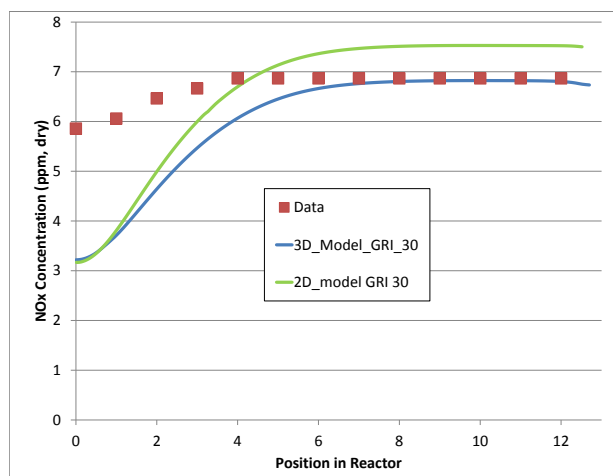
Figure 6.5: Profile of NO_X concentration from reactor centerline to wall, measured and predicted by CFD for H_2 combustion with NO_X formation chemistry in two and three dimensions.

These figures show that both the two and three dimensional models predict the data in the recirculation zone with reasonable accuracy; however, the models un-

der predict temperature in the near jet region. As discussed above, the turbulence/chemistry interaction is not modelled properly within this region. This is a region of very high turbulent kinetic energy, and the turbulence/chemistry coupling via the Eddy Dissipation Concept may not be accurate under these extreme conditions. This highly turbulent jet is a region of low Damköhler Number. The EDC model, as it is implemented in Fluent, does not account for the reaction rates in the fluid surrounding the fine scales. Accounting for these rates would increase the total reaction rate in the jet and bring up both temperature and most likely NO_X predictions on centerline.

The 2D model predicts a slightly higher NO_X concentration and temperature in the recirculation zone than the 3D model. The slightly larger NO_X prediction is likely due to the higher temperature prediction in the 2D model. The difference in temperature is thought to be due to a difference in the manner that heat transfer is handled in the different models. Since the 2D model has a far faster convergence time and still does a reasonable job of predicting both temperature and NO_X concentration in the recirculation zone, all results shown later below are from the 2D model only.

The results shown in Figure 6.2 depicting H_2 rate of destruction with and without the UDF look nearly identical to one another. In order to check the real difference between the models, temperature and NO_X plots from the centerline to the wall are shown for the 2D H_2 combustion model both with and without the UDF. There is a small temperature deficit at the wall for the simulation where the boundary layer reactions are turned off. This model also shows a slight increase in NO_X concentration within the center of the recirculation zone. We will show later in this section that the majority of the NO_X production for the H_2 flame is produced just above the turbulent flame brush.
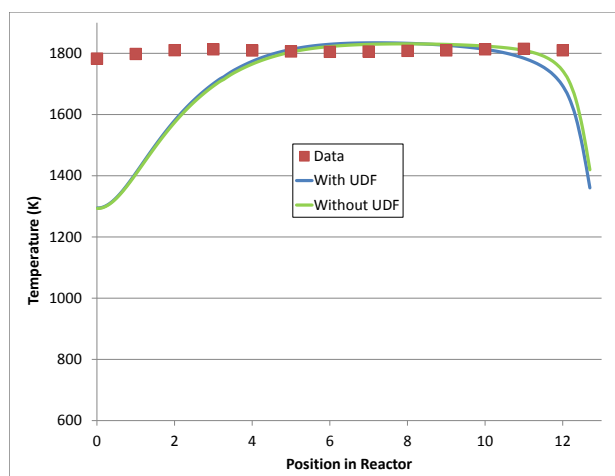
Figure 6.6: Profile of temperature from reactor centerline to wall, measured and predicted by 2D CFD for H_2 combustion with and without a UDF.
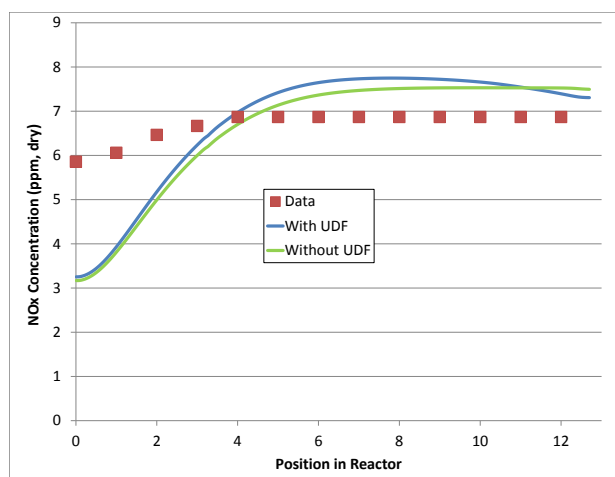
Figure 6.7: Profile of NO_X concentration from reactor centerline to wall, measured and predicted by 2D CFD for H_2 combustion with and without a UDF.

For the case with the UDF (boundary layer reactions are off), some unreacted radicals are carried around through the boundary layer and are entrained back into the jet; thus making slightly more NO_X than if the radicals were consumed in the

boundary layer. The difference in NO_X prediction is small here; however the boundary layer reactions may become more of a concern when simulating fuels with high levels of slow burning fuels such as CO.

Figures 6.8 and 6.9 show the predicted radical fields within the reactor. The highest concentration of radicals is found in and around the jet, and comparing the results with the computed H_2 destruction rates of Figure 6.2, the radical concentrations peak near the region of maximum H_2 destruction. As discussed above, the computed radical concentrations have shifted slightly in location when the UDF is employed.

When the fluid moves into the recirculation zone, these radical concentrations are already starting to relax. This finding supports the results of Figure 5.42, which shows that a PSB followed by a PFR is a more accurate way to build a CRN for a highly reactive fuel such as H_2, as opposed to the 3-element CRN developed in Chapter 4. The region of high radical concentrations for H_2 combustion encompass a quite small volume. Thus, artificially spreading the reactions throughout the entire recirculation zone produces higher average radical concentrations and thus yields higher than measured NO_X concentrations.

(a) Without UDF   (b) With UDF
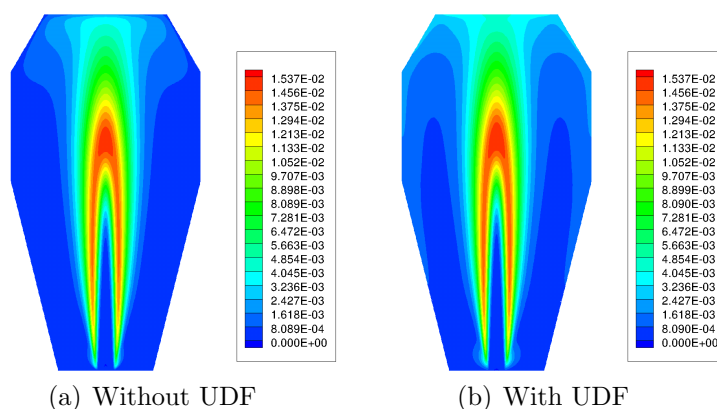
Figure 6.8: Contours of H predicted by CFD for H_2 combustion (mole fraction)

(a) Without UDF   (b) With UDF
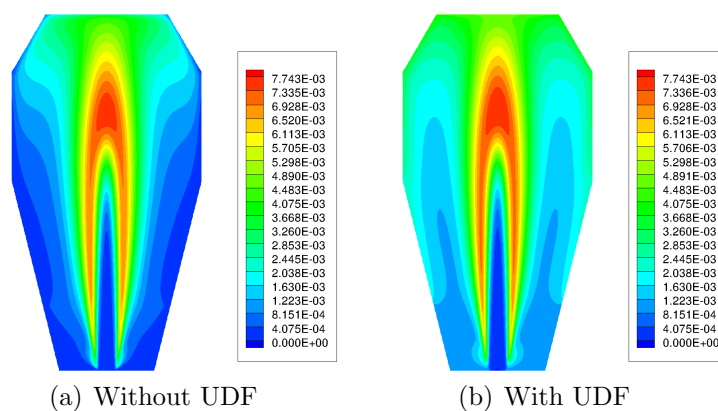
Figure 6.9: Contours of O predicted by CFD for H_2 combustion (mole fraction)

(a) Without UDF   (b) With UDF
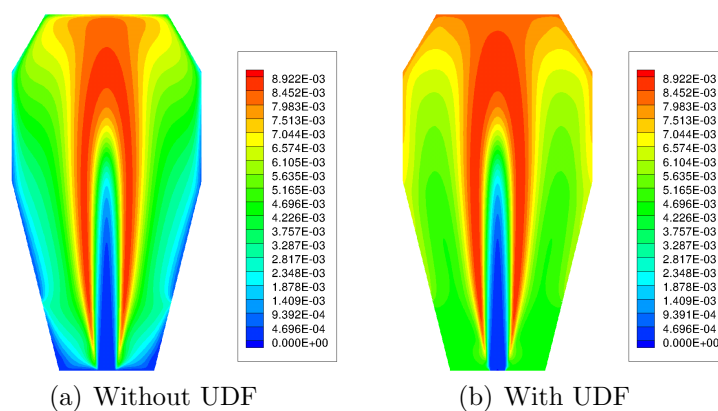
Figure 6.10: Contours of OH predicted by CFD for H_2 combustion (mole fraction)

We used the methodology presented in Section 5.3 to determine the NO_X contribution from each pathway for 2D CFD simulations of H_2 combustion. This is done by removing the rate limiting reactions from two pathways and running the model again. For example, to determine the contribution to NO_X production from only the Zeldovich pathway, the rate limiting reactions for both the NNH and N_2O pathways are removed from the mechanism. The results of isolating the NO_X formation mechanism into the specific pathway contributions are shown in Figure 6.11 for H_2 combustion

with the boundary layer reactions turned off.
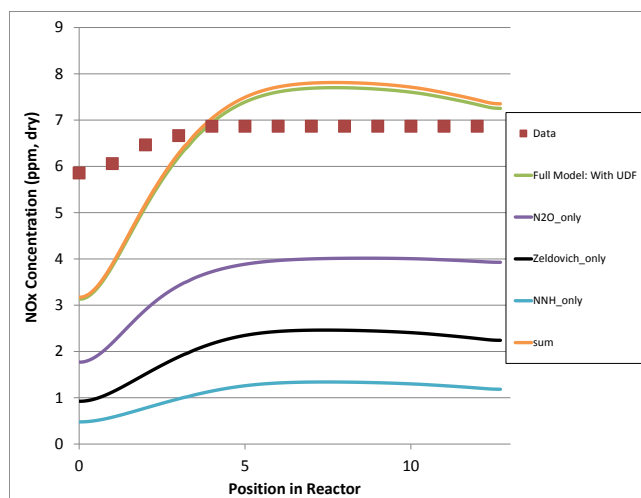
Figure 6.11: Profile of NO_X concentration from reactor centerline to wall, measured and predicted by CFD for H_2 combustion with NO_X formation chemistry in two dimensions for each NO_X pathway.

The figure shows that the N_2O pathway is the the most significant pathway to NO_X formation followed by the Zeldovich and NNH pathways. This is the same result as seen from the CRN modeling shown in Figure 5.37. The rate of NO production from the full mechanism is shown in Figure 6.12. For reference, the rate of NO_X production from the full mechanism with boundary layer reactions turned on is also shown in Figure 6.12. The model with boundary layer reactions turned on (without the UDF) shows very high reaction rates at the wall (particularly at the top of the reactor). However, these high rates near the wall do not cause the plot to look that different than the plot with the boundary layer reactions disabled. When the scale is adjusted to reflect the same scale as the solution with the UDF, the magnitude and position of the rates with and without the UDF look nearly identical. This is expected since the NO_X concentrations along the probe traverse are nearly identical as shown above in Figure 6.7.

(a) With UDF   (b) Without UDF   (c) Without UDF, mod scale
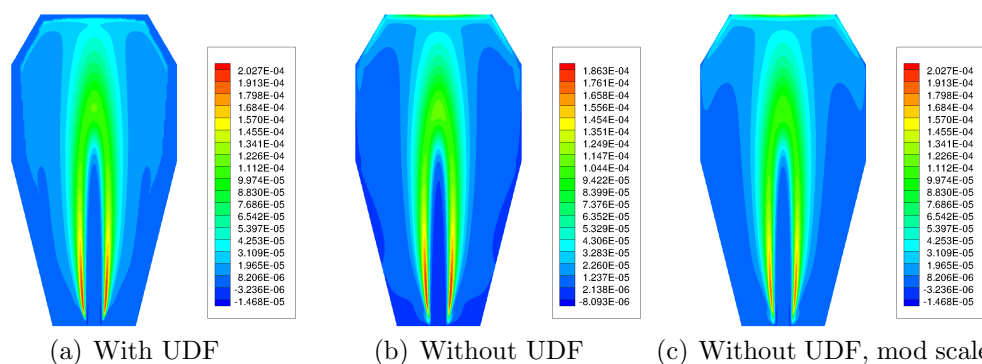
Figure 6.12: Contours of the rate of NO_X production for the full GRI 3.0 mechanism with the Konnov4 modification. (kmole/m^3-s)

A larger version of NO_X formation from the full mechanism as well as NO_X production for each of the three pathways is shown in Figures 6.13 through 6.16.
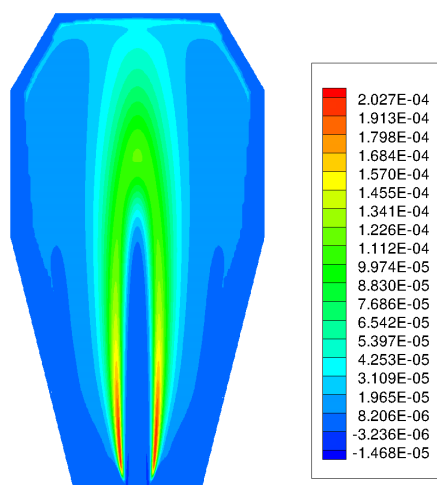
Figure 6.13: Contours of the rate of NO_X production for the full GRI 3.0 mechanism with the Konnov4 modification. (kmoles/m^3-s).
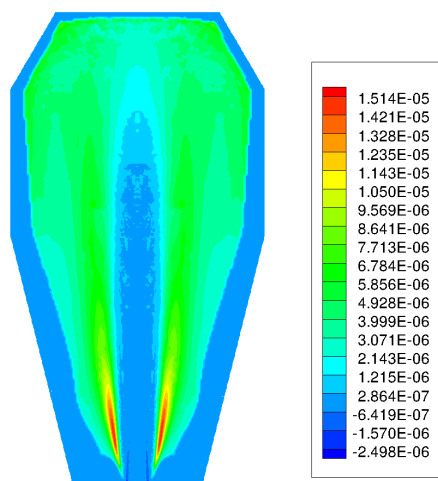
Figure 6.14: Contours of the rate of NO$_X$ production from the Zeldovich pathway only (kmoles/m^3-s).
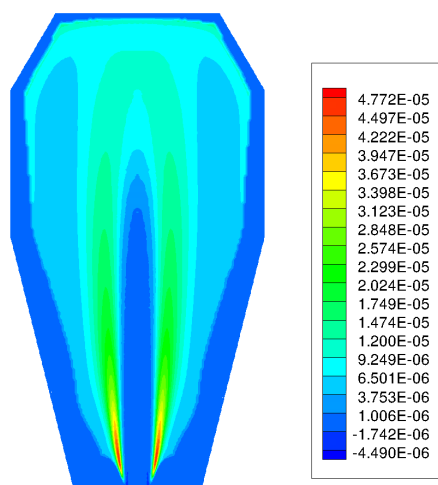
Figure 6.15: Contours of the rate of NO$_X$ production from the N$_2$O pathway only (kmoles/m^3-s).
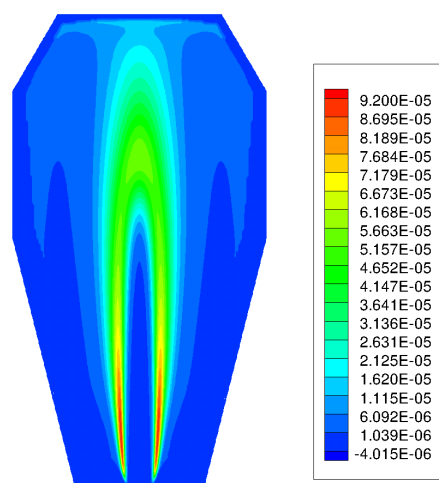
Figure 6.16: Contours of the rate of NO$_X$ production from the NNH pathway only (kmoles/m^3-s).

These figures show that most of the NO$_X$ production occurs in and around the turbulent flame brush with most of the production taking place within the shear layer of the jet just as it enters the reactor. NO$_X$ production from the Zeldovich pathway is the largest in the shear region, but extends well into the high temperature region of the reactor. Peak production from the N$_2$O and NNH pathways is also anchored around the jet shear layer. There is some production in the recirculation zone for the N$_2$O pathway since this pathway is both sensitive to temperature and O radical, which peaks at the top of the jet as shown in Figure 6.9. The NNH pathway has a weak temperature dependance; thus, the contours of peak NO$_X$ production are found around the jet where H radical is the largest. There is almost no production due to the NNH pathway in the recirculation zone.

As mentioned above, the EDC model underpredicts the reaction rate in regions of low Damköhler number (i.e., in the turbulent jet region). Since it does not compute reaction rate in the fluid surrounding the fine scales, we decided to artificially increase the volume of the fine scales; essentially forcing the code to account for reaction taking place in a larger portion of the cell. Fluent limits the quantity $(\gamma^*)^2/(1 - (\gamma^*)^3)$ in

Equation 6.4 to unity; thus limiting the computed quantity of γ^* to 0.75488. One could increase the value of γ^* to 0.75488 everywhere, which would make the quantity $(\gamma^*)^2/(1 - (\gamma^*)^3)$ in Equation 6.4 equal to unity, and the reaction rate would be at EDC limit imposed by Fluent. This however, is not possible, because Fluent does not provide access to this variable, we instead increased the volume fraction constant, C_γ, in Equation 6.1 to achieve the same result. Figures 6.17 and 6.18 show the effect that increasing the reaction rate to the EDC limit has on temperature and NO_X predictions. The results are shown for 2D simulations without the UDF.
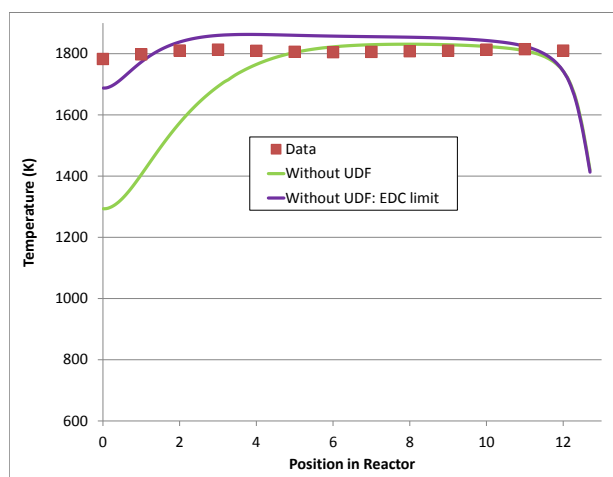
Figure 6.17: Profile of temperature from reactor centerline to wall, measured and predicted by CFD for H_2 combustion with NO_X formation chemistry in 2D. EDC limit is shown for comparison.
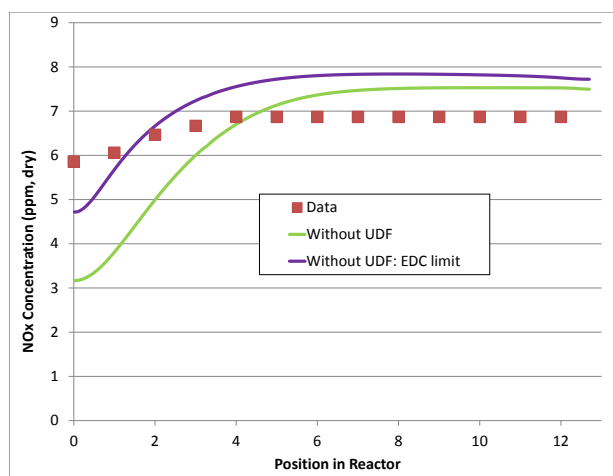
Figure 6.18: Profile of NO_X concentration from reactor centerline to wall, measured and predicted by CFD for H_2 combustion with NO_X formation chemistry in 2D. EDC limit is shown for comparison.

As expected, both the temperature and NO_X concentrations come up on centerline. Temperature and NO_X have, however, also increased within the recirculation zone; albeit by small amounts. Since the EDC model is based on turbulence energy cascade models with the volume fraction, $(\gamma^*)^3$ computed from ν and the turbulence quantities k and ε [86]; it would not be legitimate to increase this reaction rate everywhere. However the above results do show that the reaction rates are too small in the jet, and if the rates were increased the model would better agree with the data within the jet region. This error likely occurs due to limitation on the EDC model in regions of high turbulence intensity (e.g., low Damköhler number).

6.3 H_2/CO Combustion

Since there is no prompt NO_X pathway in CO combustion, the model is only barely more computationally expensive than that of H_2 combustion with NO_X formation. Basic chemical mechanism reduction analysis determines that both HCO and NCO do not need to be included in the mechanism when simulating lean combustion; thus

only two additional species and four reactions are added to describe the CO/H2 system with NO_X formation. This new mechanism includes 20 species with 73 reactions. A fuel composed of 50% H_2/50% CO is chosen for the 2-D CFD simulations.

The temperature and CO profiles from both the experiments and the CFD simulations are shown with and without the UDF in Figures 6.19 and 6.20.
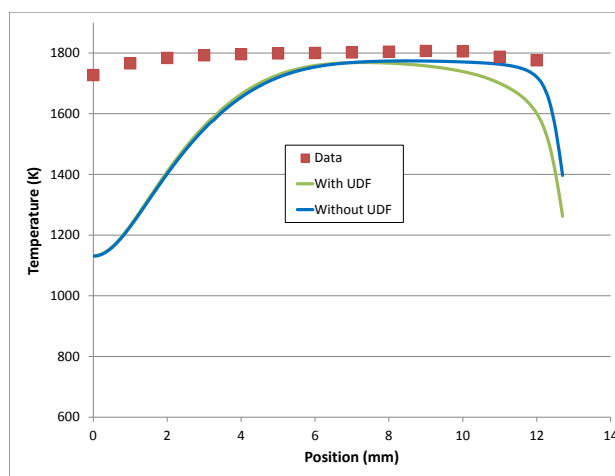
Figure 6.19: Profile of temperature from reactor centerline to wall, measured and predicted by CFD for 50%H_2/50%CO combustion. T = 1800 K.

Figure 6.20: Profile of CO from reactor centerline to wall, measured and predicted by CFD for $50\%H_2/50\%CO$ combustion. T = 1800 K.

Similar to the CFD results shown for H_2 combustion, this model under predicts temperature on centerline, but does better within the recirculation zone. As expected, the model over predicts CO concentration on centerline. This under prediction is one of the factors contributing to a temperature deficit on centerline; some question exists, however, whether the data measured on centerline are correct. As explained in Section 5.1 and Appendix A, a significant amount of CO oxidation probably takes place within the sample probe. Syngas fuels with high concentrations of CO within the fresh mixture may be especially prone to this problem. Also note the large temperature deficit and CO rise shown at the wall for the simulation run with the UDF (where the wall reactions have been turned off in the boundary layer). Section 6.2 shows that the UDF did not significantly affect the results for H_2 combustion. However, since CO is so much slower to react, the reactions in the boundary layer do make a difference. The computed contours of CO, H, O, and OH are shown in Figures 6.21 through 6.24.

(a) Without UDF   (b) With UDF
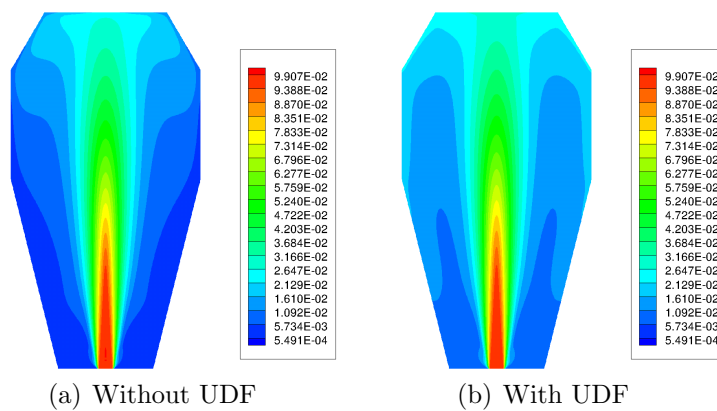
Figure 6.21: Contours of CO predicted by CFD for H_2/CO combustion (mole fraction)

(a) Without UDF   (b) With UDF
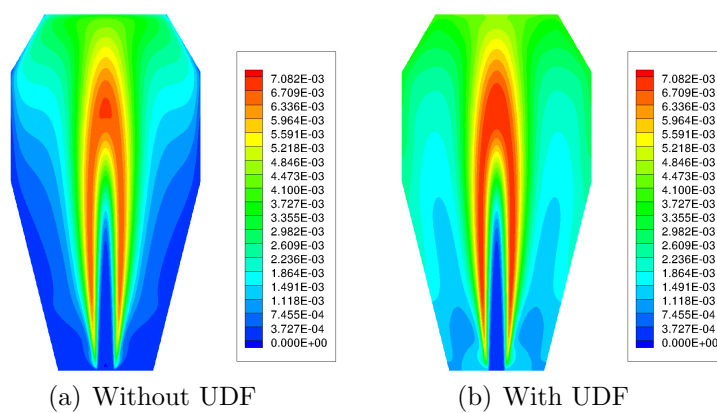
Figure 6.22: Contours of H predicted by CFD for H_2/CO combustion (mole fraction)

(a) Without UDF   (b) With UDF
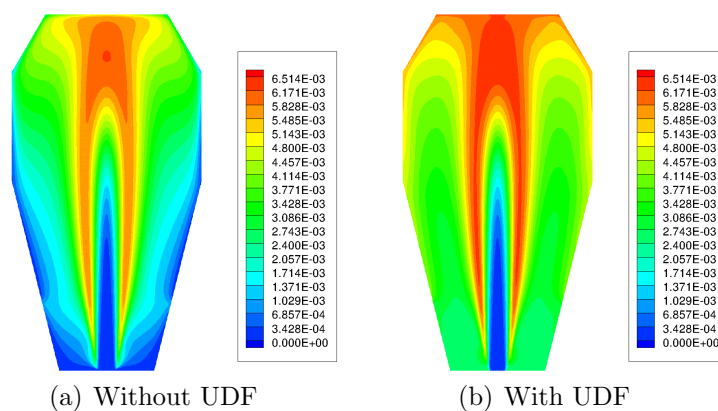
Figure 6.23: Contours of O predicted by CFD for H_2/CO combustion (mole fraction)

(a) Without UDF   (b) With UDF
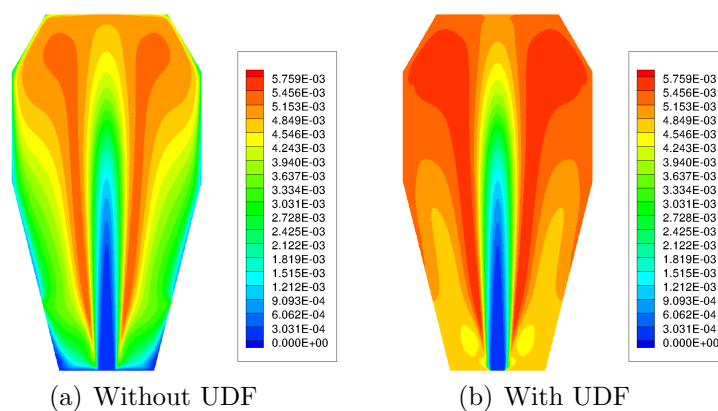
Figure 6.24: Contours of OH predicted by CFD for H_2/CO combustion (mole fraction)

In contrast to H_2 combustion, the CO addition to the fuel causes the free radicals to spread out and push further away from the jet. As expected, the UDF increases the concentrations of the free radicals and prevents CO burnout in the boundary layer. The measured and predicted NO_X concentration along the probe traverse is shown in Figure 6.25.
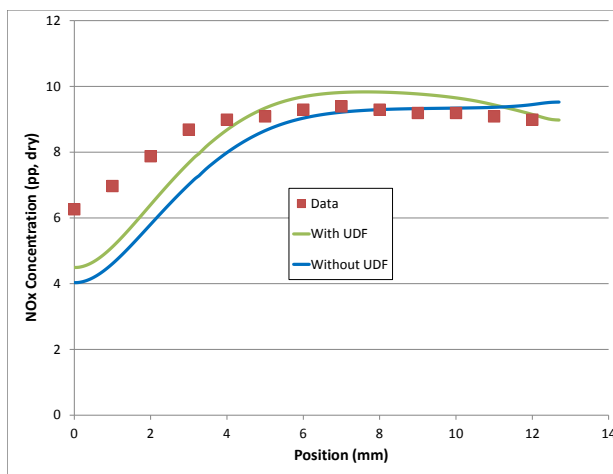
Figure 6.25: Profile of NO_X from reactor centerline to wall, measured and predicted by CFD for $50\%H_2/50\%CO$ combustion. T = 1800 K.

Similar to the results for H_2 combustion shown above, the UDF increases NO_X production in the center of the reactor. The model does follow the data better in this case than in H_2 combustion. We believe this to be largely due to a better prediction of temperature in the recirculation zone.

The rate of NO_X production within the reactor is shown in Figure 6.26. Although the maximum rate of NO_X production shown in Figure 6.26 is less than that in Figure 6.13 for H_2 combustion, the production fills the entire reactor, where the production for H_2 combustion is strong in and around the jet. A pathway analysis was not performed for this mix; however, it can be assumed that the increase in production is largely due to an increase in production from the N_2O and Zeldovich pathways as shown in Figure 5.45 due to the wider distribution of O-atom over the reactor volume for the slower burning CO.

(a) Without UDF   (b) With UDF
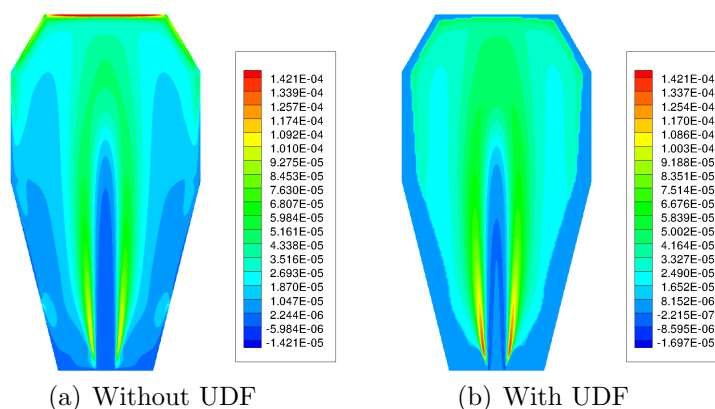
Figure 6.26: Contours of NO_X rate of production predicted by CFD for H_2/CO combustion (kmoles/m^3-s).

6.4 CH_4 Combustion

Since the prompt pathway to NO_X formation is important for CH_4 combustion, especially at the high heat loss conditions in the JSR, this pathway must be included in the chemical mechanism used in the CH_4 CFD model. For CH_4 combustion, the GRI 3.0 mechanism has been systematically reduced by Karalus [88] to capture the major chemistry associated with CH_4 oxidation and NO_X formation. The skeletal mechanism was developed by applying the Direct Relational Graph (DRG) method of Lu and Law [89] to a sample of perfectly stirred reactors (PSRs) using GRI-Mech 3.0. The parameter space was chosen to include a single pressure of 1 atm, equivalence ratios from 0.4 to 1.0, preheat up to 600 K, and mean PSR residence times from near blowout to 3 ms [88]. The resulting mechanism contains 30 species and 177 reactions. A plot similar to Figure 5.20 is shown below in Figure 6.27, where the reduced mechanism is compared to GRI Mech 3.0 [73] and GRI Mech 3.0 with the Konnov modification [78]. All three mechanisms are run in the 3-Element CRN developed in Chapter 4.

The reduced mechanism gives results almost identical to GRI Mech 3.0, computing NO_X predictions only slightly larger than the parent mechanism. This is expected
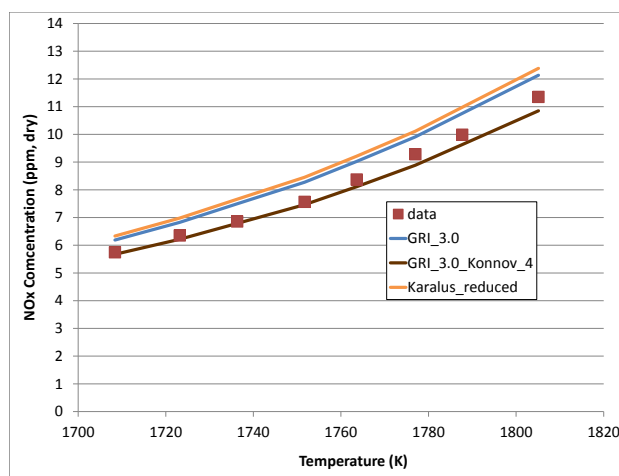
Figure 6.27: Comparison the reduced mechanism against GRI Mech 3.0 and GRI Mech 3.0 with the Konnov modification against experimental NO_X data going from 1708 to 1805 K for LPM CH_4 combustion.

since the mechanism was developed using a parameter space that is well within the experimental data shown in Figure 6.27.

The temperature profiles as both measured and computed by CFD for CH_4 combustion is shown below in Figures 6.28. The reduced mechanism developed by Karalus [88] with and without the UDF, the reduced mechanism at the EDC Limit with and without the UDF, and the 3 step global mechanism developed by Nicol et al. [66] from 3D simulation are shown for comparison. Figure 6.28 shows that the reduced mechanism under predicts the temperature on centerline by about 150 degrees and in the recirculation zone by about 50 degrees. When the UDF is turned on, there is an additional temperature deficit at the wall, which is due to a lack of CO oxidation within the boundary layer. The computed solutions at the EDC limit are nearly identical to each other both with and without the UDF; however, there is a slight decrease in temperature near the wall for the case where wall reactions are disabled.

The reaction rates in the rest of the reactor are fast enough so the boundary layer does not influence the results as much. Note that the EDC model at its reaction limit
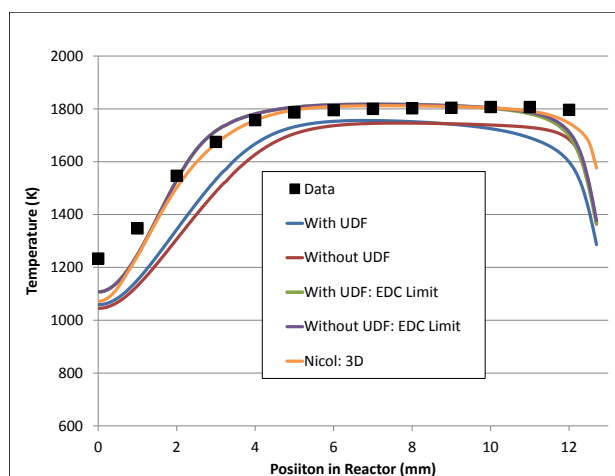
Figure 6.28: Profile of temperature from reactor centerline to wall, measured and predicted by CFD for CH_4 combustion.

accurately predicts the temperature within the recirculation zone; however it under predicts temperature on centerline by about 100 degrees. The 3D model employs 3-step global chemistry and the turbulence-chemistry interaction is modelled with the Finite Rate/Eddy Dissipation model. This model computes both a turbulent rate and a chemical rate of reaction and chooses the smaller of the two. Figure 6.29 shows the rate of destruction of CH_4 in the 3D model computed by turbulence, chemistry, and the resultant reaction rate. Since the reaction describing CH_4 destruction is a globalized reaction, the CH_4 is made into CO in one step rather than many steps with various hydrocarbon intermediates. This global CH_4 oxidation step (shown in Table 4.1) is quite fast, and the resultant reaction rate is clearly controlled by the turbulent rate.

(a) Kinetic Rate   (b) Turbulent Rate   (c) Resultant Rate
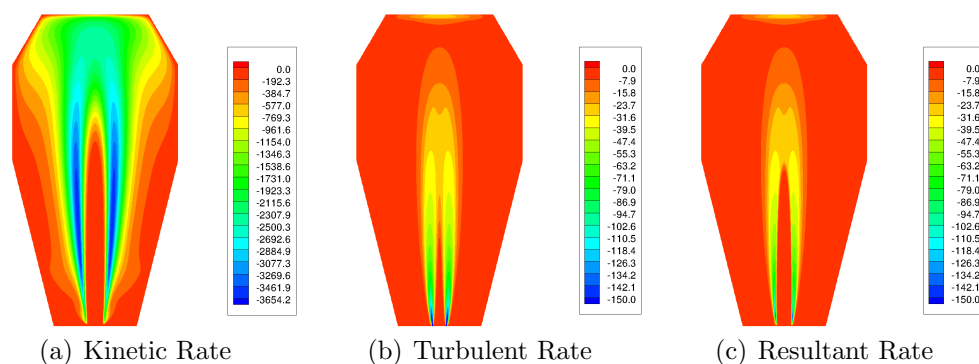
Figure 6.29: Contours of the rate of CH_4 destruction for the 3D finite rate/eddy dissipation model. $(kg/m^3$-s)

Although the turbulent rate is over a magnitude slower than the kinetic rate computed by the global chemistry, it is still far faster on centerline than the rates of CH_4 destruction computed by the EDC model for both the default conditions and at the EDC limit as shown in Figure 6.30 (EDC models are shown with the UDF).

(a) Finite rate/Eddy Dissipation   (b) EDC w/ UDF   (c) EDC w/ UDF: EDC limit
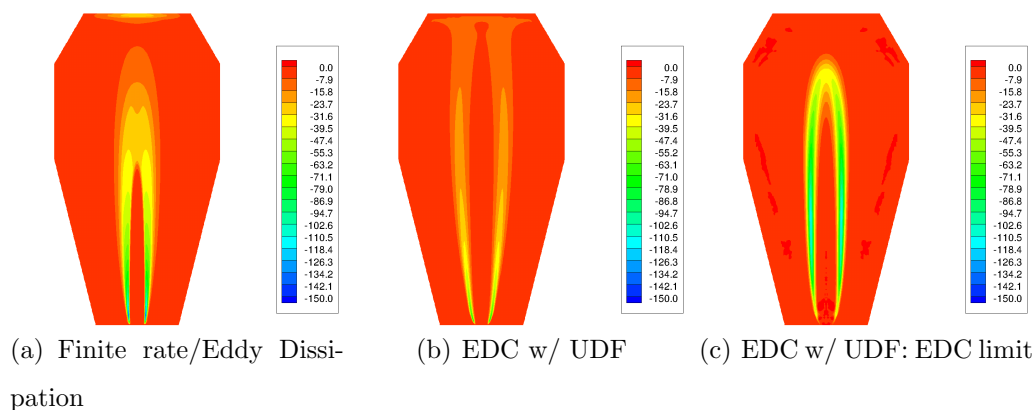
Figure 6.30: Contours of the rate of CH_4 destruction for the EDC model at default conditions and at the EDC limit, and for the 3D finite rate/eddy dissipation model. $(kg/m^3$-s)

Since chemistry is always incorporated into the reaction rate in the EDC model, the computed reaction rates will always be slower than the turbulent rates in the

Eddy Dissipation/Finite Rate model. Setting the volume fraction of EDC model to its limit aids in the destruction of CH_4 within the jet, but it is still slower than the purely turbulent rate. Similar trends are shown in Figure 6.31, where CO profiles are plotted from centerline to the wall, both measured and predicted by CFD.
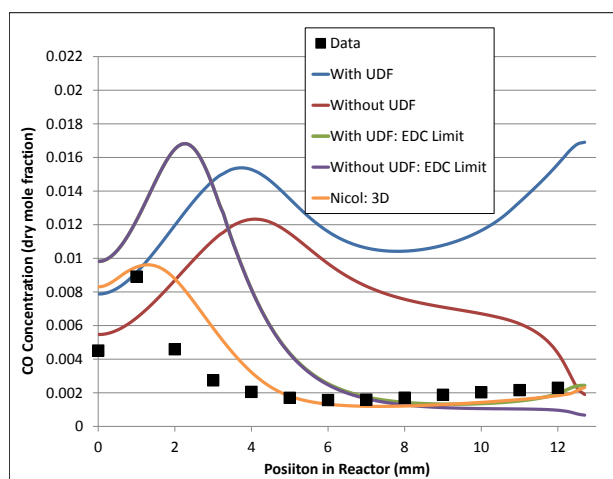
Figure 6.31: Profile of CO from reactor centerline to wall, measured and predicted by CFD for CH_4 combustion.

The EDC model with and without the UDF does not properly predict the position of the CO peak nor the magnitude. As expected, there is a large increase in CO concentration near the wall when wall reactions are disabled. The EDC model at the EDC limit does a better job at predicting position of the CO peak; however, it predicts about double the magnitude of the data. Both EDC models at the EDC limit (with and without the UDF) predict the CO concentration within the recirculation zone with reasonable accuracy; however, as explained above, it is questionable whether the measured data reflects the CO concentrations actually within the reactor due to CO oxidation in the probe. The 3D model with Nicol's 3-step global chemistry does the best job at predicting the CO peak in both position and magnitude. Similar to the EDC model at the EDC limit, it also predicts the CO concentration within the

recirculation zone quite accurately. However, the same question with respect to probe oxidation applies here as well.

The Finite Rate/Eddy Dissipation (FR/RD) model appears to predict temperature and CO better than the EDC model. This can be attributed to its ability to handle reaction rate within regions of low Damköhler number. Unfortunately, the FR/RD model does not have the ability to compute intermediate radicals.

The formation of NO_X can be globalized and has been executed with success for LPM CH_4 combustion [66], [68]. However, since the focus of this study is on the differences in NO_X formation between a wide variety of fuels, it is more useful to compute NO_X using detailed chemistry predicting the formation of free radicals. The computed radical concentrations from the EDC model for 2-D CFD are shown below in Figures 6.32 through 6.34.

(a) Without UDF

(b) With UDF

(c) Without UDF, EDC limit

(d) With UDF, EDC limit
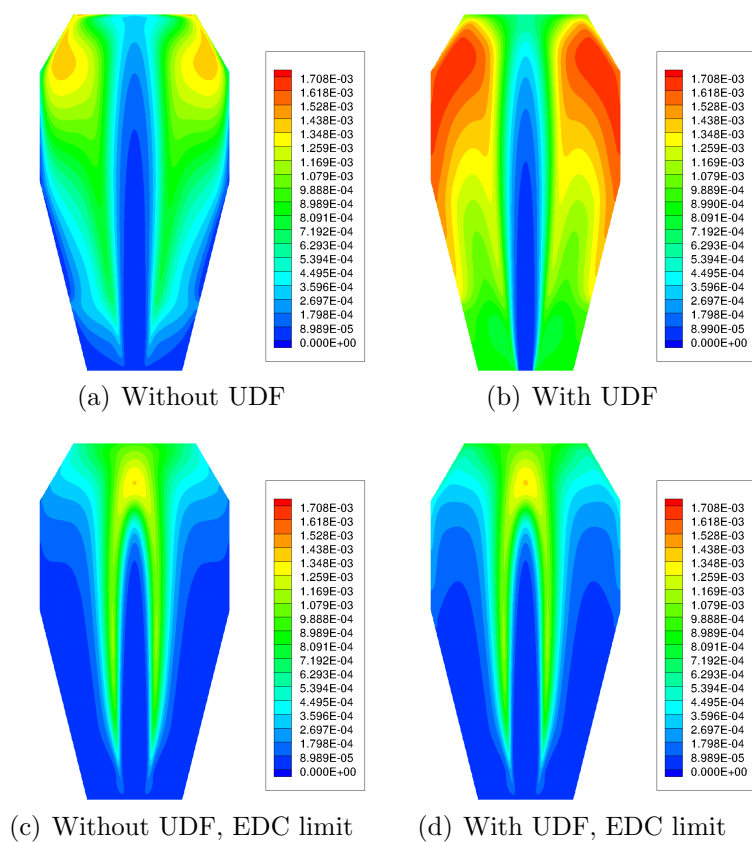
Figure 6.32: Contours of H atom for CH_4 combustion from the reduced GRI 3.0 mechanism both with and without the UDF at the default EDC conditions and at the EDC limit. (mole fraction)

(a) Without UDF   (b) With UDF

(c) Without UDF, EDC limit   (d) With UDF, EDC limit
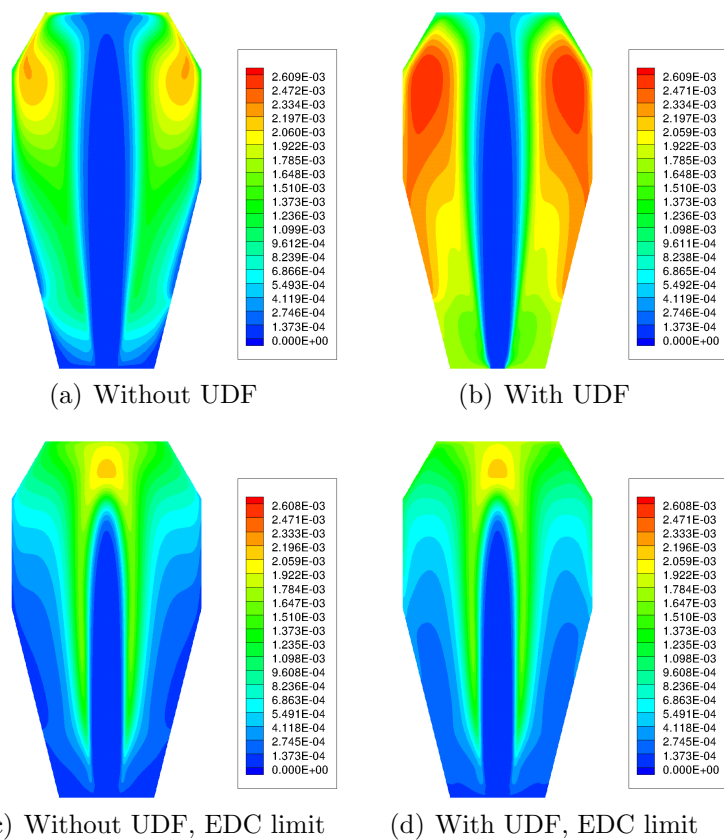
Figure 6.33: Contours of O atom for CH_4 combustion from the reduced GRI 3.0 mechanism both with and without the UDF at the default EDC conditions and at the EDC limit. (mole fraction)

(a) Without UDF   (b) With UDF

(c) Without UDF, EDC limit   (d) With UDF, EDC limit
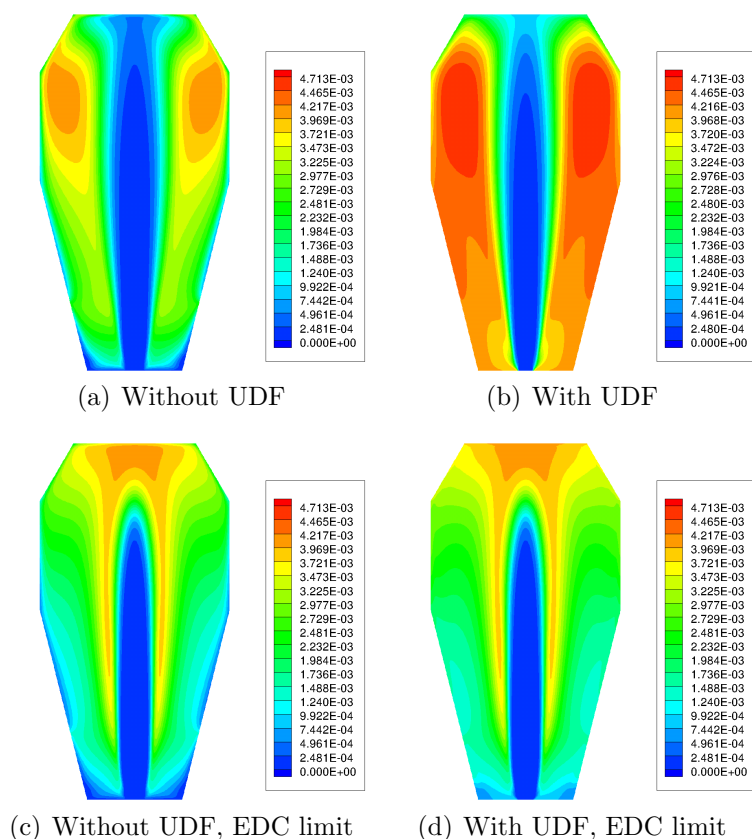
Figure 6.34: Contours of OH atom for CH_4 combustion from the reduced GRI 3.0 mechanism both with and without the UDF at the default EDC conditions and at the EDC limit. (mole fraction)

The scale in the plots has been set to the maximum computed concentration to gain perspective between models. The default EDC model with the UDF has the largest computed radical concentrations. This is expected since CO and radicals are convected around the boundary layer and re-entrained into the jet. The maximum concentration of the radicals for the default EDC model without the UDF and the EDC model at the EDC limit with and without the UDF are about equal. This also is expected since the the radicals are likely to be consumed in the boundary layer for the default EDC model without the UDF and the radicals are consumed soon after leaving the jet for each model at the EDC limit.

Figure 6.35 shows the concentration of OH from the reactor centerline to the wall from each CFD model. The plot also shows measured OH concentrations taken by Malte et al. [90] for LPM CH_4 combustion in a JSR at an equivalence ratio of 0.7, a measured temperature of 1750 K, and a pressure of 0.92 atm. The conditions are almost identical to the experimental conditions in the present work; however, they ran with a reactor loading of $4.03 * 10^{-2} g/cm^3 - s$ and the loading in the present work is $6.25 * 10^{-2} g/cm^3 - s$. The measured data were obtained from integrated absorption measurements and should be thought of as average values throughout the recirculation zone and the downstream region of one of the seven jets. Since these were spectral measurements, there is no effect from probe oxidation as seen in the present study. In fact, the computed OH rotational temperature and measured thermocouple temperatures were virtually identical [90].
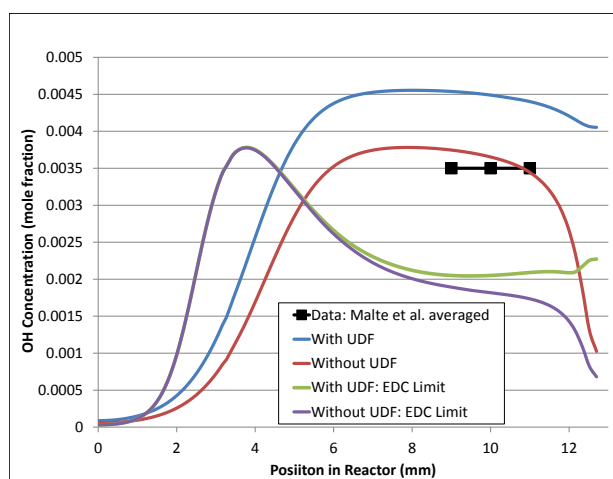
Figure 6.35: Profile of OH from reactor centerline to wall, measured and predicted by CFD for CH_4 combustion.

In their study [90], Malte et al. showed that at constant equivalence ratio, OH concentration increased with increasing reactor loading. We thus expect that if the same measurements were taken in the present JSR, the data would fall somewhere in

between the predictions of the default EDC models with and and without the UDF.

Figure 6.36 shows NO_X profiles for both data and CFD predictions plotted from centerline to the wall. These calculations used the reduced mechanism from Karalus. The default EDC models with and without the UDF show the same trend as above for H_2 and H_2/CO combustion; the UDF causes an increase in NO production in the center of the reactor due to re-entrainment of unreacted radicals. Note that the correction by Konnov to the GRI Mech 3.0 has not been applied here. However, it is shown in Chapter 5 that the Konnov correction does not affect CH_4 combustion to the same extent that it affects fuel blends containing H_2. Both EDC models with the default γ^* under predict temperature by about 50 degrees. We expect that the predicted NO_X concentrations would increase if temperature is predicted properly.
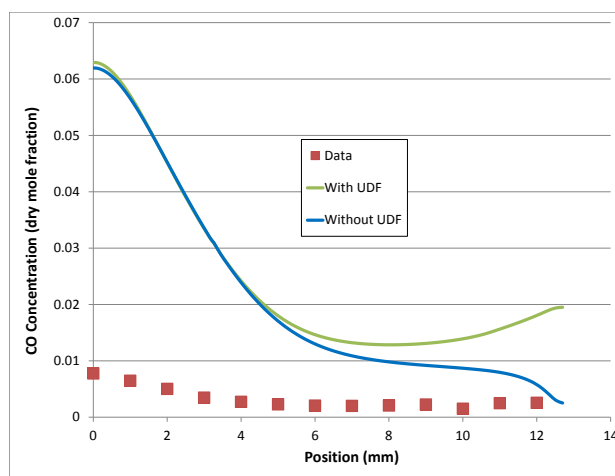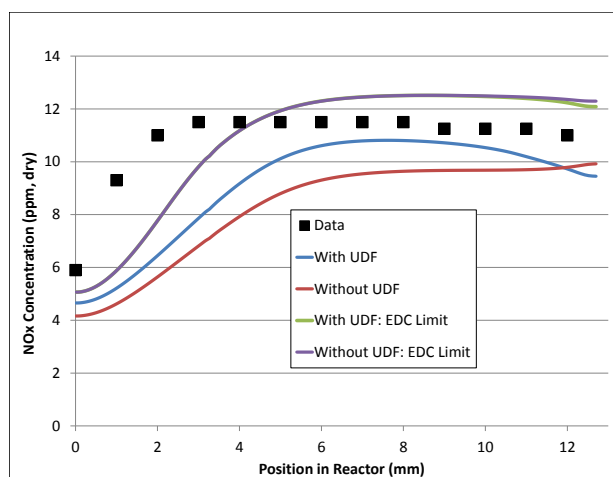

Figure 6.36: Profile of NO_X from reactor centerline to wall, measured and predicted by CFD for CH_4 combustion.

Similar to the analysis shown above in Section 6.2, the NO_X contribution from each pathway is determined by removing the rate limiting reactions from three pathways and repeating the model run. The results shown in Figure 6.37 follow the trends of Chapter 5. The prompt pathway is the largest NO_X producer, followed by N_2O,

Zeldovich, and NNH. The contours of NO_X production for the reduced mechanism [88] as well as each of the pathways are shown below in Figures 6.38 through 6.42.
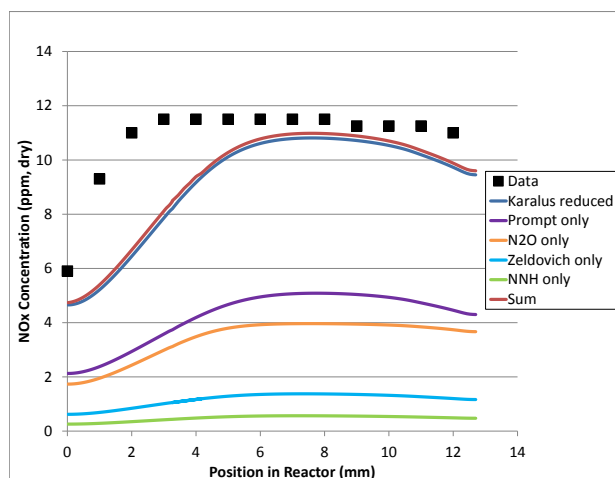
Figure 6.37: Profile of NO_X concentration from reactor centerline to wall, measured and predicted by CFD for CH_4 combustion with NO_X formation chemistry in 2D for each NO_X pathway.
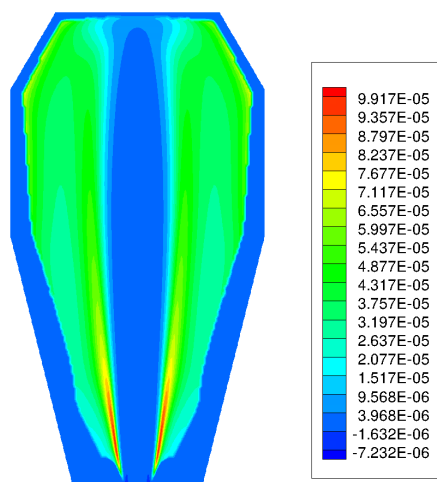
Figure 6.38: Contours of the rate of NO_X production from the reduced GRI 3.0 mechanism (kmoles/m³-s).
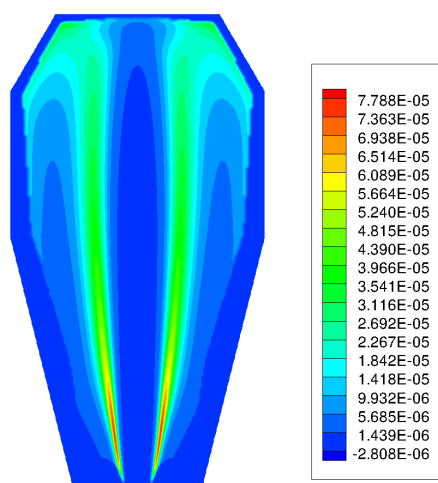
Figure 6.39: Contours of the rate of NO$_X$ production from the prompt pathway only (kmoles/m^3-s).
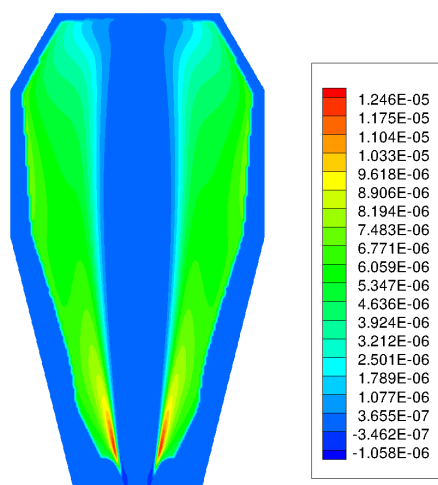
Figure 6.40: Contours of the rate of NO$_X$ production from the N$_2$O pathway only (kmoles/m^3-s).
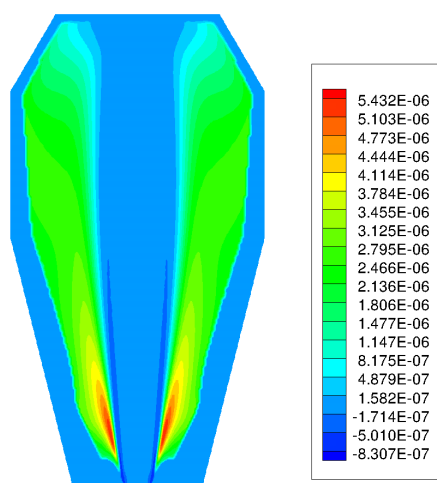
Figure 6.41: Contours of the rate of NO$_X$ production from the Zeldovich pathway only (kmoles/m^3-s).
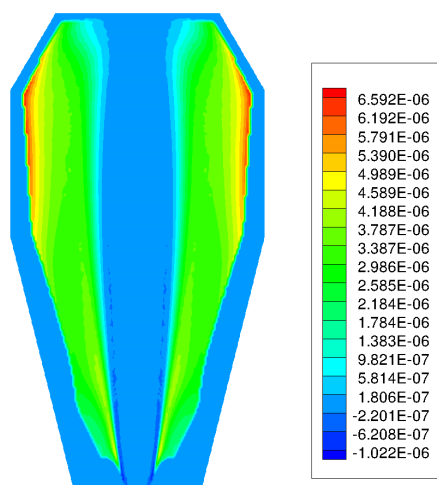
Figure 6.42: Contours of the rate of NO$_X$ production from the NNH pathway only (kmoles/m^3-s).

The computed contours of CH, N$_2$O, N, and NNH are shown below in Figure 6.43 to help explain the trends shown in Figures 6.38 through 6.42.

(a) CH

(b) N$_2$O

(c) N

(d) NNH
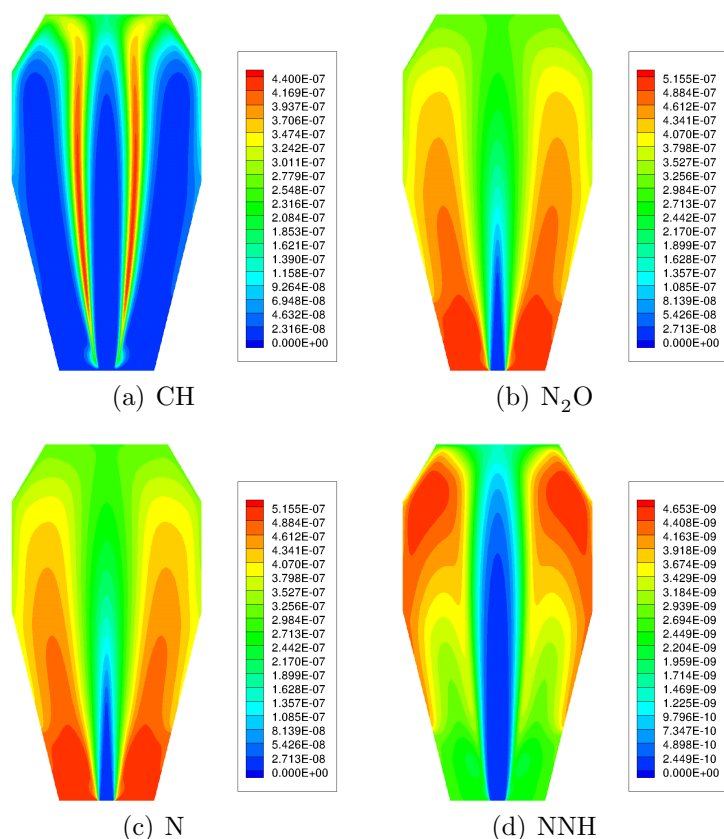
Figure 6.43: Contours of NO$_X$ producing species within the JSR for CH$_4$ combustion from the reduced GRI 3.0 mechanism. (mole fraction)

The most important mechanism is the prompt, which peaks just on the outside of the jet. Almost no prompt production is active in the recirculation zone, which makes sense since the CH radical is fully consumed right at the jet boundary. The N radical and N$_2$O molecule extend well into the entire reactor volume. Since O atom is also shown to extend into the recirculation zone, it makes sense that the production from the N$_2$O and Zeldovich pathways are fairly uniform throughout the recirculation zone. The contours of H atom peak in the upper portion of the recirculation zone, thus it follows that NNH also peaks in the same region. Since O atom also peaks in this region, it is expected that the fastest NO$_X$ production from the NNH pathway is in the upper portion of the recirculation zone. We note that if the reactions were turned

on within the boundary layer, the NNH pathway may become a stronger contributor.

Chapter 7

SUMMARY AND CONCLUSIONS

A high intensity, single-jet stirred reactor, JSR, is used to study both pollutant formation and resistance to blowout for CH_4 and the variety of gaseous fuel alternatives to CH_4 listed in Table 1.1. The JSR is intended to act as an idealized lean, premixed combustor. NO_X measurements are taken at a nominal combustion temperature of 1800 K, atmospheric pressure, and a reactor residence time of 3 ms. This ensures that the results focus on the effect of fuel chemistry by removing temperature, residence time, and pressure as variables. Additionally, the effects of changing temperature and residence time are investigated for selected fuels.

7.1 Experiments

At the nominal temperature and residence time, the experimental results show the following trends for NO_X emissions as a function of fuel category:

1. NO_X emissions decrease for combustion of CH_4/H_2 blends with increasing H_2 fuel fraction.

2. For category 3 (the O_2 blown gasified coal/petcoke), NO_X emissions decrease with increasing H_2 fuel fraction.

3. For category 2 (the process and refinery blend) and category 5 (the LNG, shale, and associated gases), NO_X emissions increase with the addition of C_2 and C_3 hydrocarbons.

4. For category 4 (the landfill gas) the addition of diluents such as CO_2 and N_2 at constant air flow produces more NO_X per kg of CH_4 consumed, and N_2 is more effective than CO_2 in increasing the NO_X emission index.

At temperatures and residence times other than the nominal conditions, the experimental results show the following trends:

1. The NO_X emissions from LPM combustion of pure CH_4, H_2, C_2H_6, and C_3H_8 are shown to be linear with residence time and exponential with temperature.

2. The addition of both H_2 and C_2H_6 to a LPM CH_4 flame is effective at extending its lean blowout limit.

7.2 Modelling

Both computational fluid dynamics (CFD) and chemical reactor network (CRN) models are used to predict, illustrate, and isolate the underlying chemical kinetic reasons for differences in emissions between selected fuel blends. In general, the modelling results have correlated well with measured data.

7.2.1 CRN Modelling

A 3-element CRN is constructed using insight from detailed spatial measurements of the reactor, the results of CFD simulations, and classical fluid dynamic correlations. Several chemical mechanisms are tested in the CRN, and GRI-Mech 3.0, a modification of GRI-Mech 3.0, and the C2-NOx mechanism prove to model the experimental data best within the CRN configuration. The CRN model performs well in predicting NO_X emissions for LPM CH_4 flames at constant air flow rate and combustion temperatures between 1700 and 1800 K. As the combustion temperature/equivalence ratio increases, the model indicates that NO_X formation increases mainly due to an

increase in the Zeldovich and prompt pathways. The CRN is employed to predict experimental trends observed when the composition of a mixture is varied.

For a LPM CH_4 flame diluted with N_2 and CO_2 held at a constant combustion temperature of 1800 K, the CRN model indicates that the increase in NO_X emissions with increased dilution is due to an enhancement of the prompt NO_X pathway. This is resulting from an increase in the CH radical concentration as the mixture moves towards stoichiometric. The model also suggests that both a smaller N_2 concentration and a preferential loss of free radicals due to CO_2 enhanced radical recombination, results in decreased NO_X emissions for CO_2 dilution compared to N_2 dilution.

The CRN model predicts NO_X emissions for a LPM CH_4/H_2 flame with reasonable accuracy. The model follows the data up to about 80% H_2 in the fuel stream, then the model over predicts NO_X as H_2 approaches 100%. The modelling suggests that a decrease in prompt NO_X is the main reason for the decrease in NO_X formation as the mixture moves from pure CH_4 to pure H_2. The model also predicts an increase in NO_X formation as the mixture nears 100% H_2 due to both the Zeldovich and N_2O pathways. Mixtures with high concentrations of H_2 have been shown to be better represented by an alternative CRN composed of a PSB followed by a recirculating PFR with heat loss, than by the 3-element CRN. The modeling results from CH_4 combustion appear relatively insensitive to CRN configuration as long as the first element is a PSB. As the H_2 concentration in the fuel increases above 80%, artificially spreading the super-equilibrium flame zone around the entire reactor appears to cause the model to increase its NO_X prediction. The CFD model for H_2 combustion shown in Chapter 6 suggests this alternative CRN as well.

Similar to the CH_4/H_2 mix, for H_2/CO combustion the alternative CRN predicts the NO_X emissions for high H_2 mixes better than the 3-element CRN. The CRN configuration also becomes less sensitive to configuration when the CO concentration of the fuel is increased. For H_2/CO combustion there is no prompt NO_X due to the lack of hydrocarbon material. The model predicts that there is almost no NO_X

production within the turbulent flame brush. The model predicts that as the volume fraction of CO in the fuel stream increases, the contributions of the N_2O, Zeldovich, and NNH pathways increase due to an increase in the concentration of O and H radicals. CO appears to produce more radicals per unit heat release than the other fuels studied.

As the CO concentration is increased in CH_4/CO fuel blends, NO_X emissions initially stay constant but then rise steeply after the CO concentration reaches about 60%. The 3-element CRN is used to model these data. The model indicates that with increasing CO concentration, prompt NO_X decreases and the other three mechanisms increase to maintain emissions. After 60% CO, the N_2O and Zeldovich pathways increase considerably due to a large increase in O atom.

Although the experiments indicate that NO_X emissions increase when C_2H_6 replaces CH_4 at the same combustion temperature, the model is not able to reproduce this trend. This may be due to inadequacies in the ability of the chemical kinetic model to replicate C_2 and C_3 behavior.

7.2.2   CFD Modelling

The two dimensional CFD simulations can spatially resolve both concentration fields and chemical production rates for free radicals and NO_X formation within the reactor. The results indicate that for H_2 combustion, NO_X is primarily formed in and around the jet. CO addition to H_2 causes radical fields to be pushed out further into the recirculation zone, which causes NO_X to be formed in a larger portion of the reactor; thus, increasing emissions. For CH_4 combustion, the radical fields encompass a large portion of the reactor like the H_2/CO mix; however, there is an additional component of NO_X formation from the prompt pathway, which causes further increases in NO_X formation and emission. This largely appears near the jet, suggesting that in CH_4 combustion, NO_X formation is a complex process involving both multiple mechanism and multiple locations in the reactor. Although the CFD simulations employing

the EDC model do a reasonably satisfactory job of predicting free radical and NO_X formation, there are some shortcomings to the model. In particular, it predicts unrealistically high reaction rates in the near wall region, and it does not account for reaction rate in the fluid surrounding the fine scales in regions of low Damköhler number, resulting in an underprediction of reaction rates in the turbulent jet..

7.2.3   Reactor Heat Loss

The experimental JSR used in this study experiences about a 20% heat loss based on the LHV of the inlet fuel. We have shown that when burning fuels containing high concentrations of hydrocarbons in a high heat loss device, the prompt pathway becomes increasingly important because of the higher equivalence ratios necessary to maintain flame temperature. This effect is not observed for fuel mixes lacking hydrocarbons.

7.2.4   NOx Entitlement

CRN modeling shows that the combustor configuration that produces the lowest NO_X emissions at a given flame temperature is a Bragg Cell with the initial PSR at blowout followed by a PFR. This indicates that the best combustor design has the smallest flame zone possible, regardless of fuel composition. The modeling results also show that for H_2 combustion, a flame zone that is slightly larger than blowout may produce significantly more NO_X than if the flame zone is enlarged further. Since it is quite difficult to design a combustor with such a tight flame zone, it may be wise to design combustors that burn high H_2 fuels to have long, lazy flames. Also note that this may explain why there is more scatter in the H_2 literature than in the CH_4 literature. The flame is more sensitive to the primary zone turbulent mixing intensity.

7.3   Final Conclusions

Final conclusions from this study are:

1. For LPM combustion of fuels containing no fuel bound N_2, NO_X is formed through four distinct mechanisms.

2. These mechanisms have different responses to temperature and stoichiometry, depending on fuel composition

3. Fuel interchangeability depends on fuel properties, combustor configuration, and combustion environment.

4. For LPM combustion, the main divisions in NO_X emissions lie in the following categories:

   (a) Fuels containing hydrocarbons and fuels composed of H_2 and CO that do not.

   (b) Fuels without and with diluents such as N_2 and CO_2.

   (c) Near adiabatic combustors versus combustors with high heat loss.

5. Appropriate CFD and CRN methodologies are shown to capture these effects.

BIBLIOGRAPHY

[1] R. M. Flores, V. G. McDonell, and G. S. Samuelsen. Impact of ethane and propane variation in natural gas on the performance of a model gas turbine combustor. *Journal of Engineering for Gas Turbines and Power*, 125:701–708, 2003.

[2] P. C. Malte, J. C. Kramlich, K. D. Spitzer, D. Yee, and S. Singh. Behavior of OH and NO_X in a mixing-influenced jet-stirred reactor, AIAA Paper No. 80-0209. In *AIAA 18th Aerospace Sciences Meeting, Pasadena, CA*, 1980.

[3] S. T. Marks and B. S. Cheyney. The effects of gas composiiton on emissions measurements. *Journal of the Institute of Energy*, 74:18–23, 2001.

[4] O. Spangelo, T. Slungaard, T. Engebretsen, and O.K. Snju. Development of a low-nox swirl burner for gaseous fuels. *Clean Air*, 2:555–563, 2006.

[5] R. A. Corr, P. C. Malte, and N. M. N. M. Marinov. Evaluation of NO_X mechanisms for lean, premixed combustion. *Journal of Engineering for Gas Turbines and Power*, 114:425–434, 1992.

[6] D. Littlejohn and R. K. Cheng. Fuel effects on a low-swirl injector for lean premixed gas turbines. *Proceedings of the Combustion Institute*, 31:31553162, 2007.

[7] M. R. Johnson, D. Littlejohn, W. A. Nazeer, K. O. Smith, and R. K. Cheng. A comparison of the flowfields and emissions of high-swirl injectors and low-swirl injectors for lean premixed gas turbines. *Proceedings of the Combustion Institute*, 30:2867–2874, 2005.

[8] J. C. Y. Lee. *Reduction of NO_X Emission for Lean Prevaporized-Premixed Combustors*. PhD thesis, University of Washington, 2000.

[9] T. Rutar, J. C. Y. Lee, P. Dagaut, P. C. Malte, and A A Byrne. NO_X formation pathways in lean-premixed-prevaporized combustion of fuels with carbon-to-hydrogen ratio between 0.25 and 0.88. *Proceedings of the IMechE. Part A: Journal of Power and Energy*, 221:387–398, 2007.

[10] H. S. Kim, V. K. Arghode, M. B. Linck, and A. K. Gupta. Hydrogen addition effects in a confined swirl-stabilized methane-air flame. *International Journal of Hydrogen Energy*, 34:1054–1062, 2009.

[11] G. S. Jackson, R. Sai, J. M. Plaia, C. M. Boggs, and K. T. Kiger. Influence of H_2 on the response of lean premixed CH_4 flames to high strained flows. *Combustion and Flame*, 132:503–511, 2003.

[12] R. W. Schefer. Reduced turbine emissions using hydrogen-enriched fuels. In *Proceedings of the 2002 U.S. DOE Hydrogen Program Review*, 2002.

[13] P. Griebel, E. Boschek, and P. Jansohn. Flame stability and NO_X emission improvements due to H_2 enrichment of turbulent, lean premixed, high pressure, methane/air flames. In *The Future of Gas Turbine Technology: 3rd International Conference*, 2006.

[14] R. W. Schefer, D. M. Wicksall, and A. K Agrawal. Combustion of hydrogen-enriched methane in a lean premixed swirl-stabilized burner. *Proceedings of the Combustion Institute*, 29:843–851, 2002.

[15] L. Xie, S. Hayashi, and K. Hirose. NO_X formation in turbulent lean-premixed combustion with minimum heat losses. In *Twenty-Sixth Symposium (International) on Combustion, The Combustion Institute*, 1996.

[16] J. Y. Ren, F. N. Egolfopoulos, and T. T. Tsotsis. NO_X emission control of lean methane-air combustion with addition of methane reforming products. *Combustion Science and Technology*, 174:181–205, 2002.

[17] D. Sequera and A. K. Agrawal. Effect of fuel composition on emissions from a low-swirl burner, GT2007-28044. In *Proceedings of ASME Turbo Expo 2007 Power for Land, Sea, and Air*, 2007.

[18] J. D. Morris, R. A. Symonds, F. L. Ballard, and A. Banti. Combustion aspects of application of hydrogen and natural gas fuel mixtures to MS9001E DLN-1 gas turbines at Elsta Plant, Terneuzen, The Netherlands, ASME Paper 98-GT-359. In *The International Gas Turbine & Aeroengine Congress & Exhibition*, 1998.

[19] F. Delattin, A. Rabhiou, S. Bram, J. De Ruyck, R. Orbay, J. Klingmann, and A. A. Konnov. A comparison between the combustion of natural gas and partially reformed natural gas in an atmospheric lean premixed turbine-type combustor. *Combustion Science and Technology*, 180:1478–1501, 2008.

[20] D. N. Anderson. Effect of hydrogen injection on the stability and emissions of an experimental premixed prevaporized propane burner. Technical report, NASA TM X-3301, 1975.

[21] V.S. Engleman, W. Bartok, J.P. Longwell, and R.B. Edelman. Experimental and theoretical studies of NO_X formation in a jet-stirred combustor. *Syposium (International) on Combustion*, 14:755–765, 1973.

[22] G. J. Rortveit, K. Zepter, O. Skreiberg, M. Fossum, and J. E. Hustad. A comparison of low-NO_X burners for combustion of methane and hydrogen mixtures. *Proceedings of the Combustion Institute*, 29:1123–1129, 2002.

[23] S. Gauthier, A. Nicolle, and D. Baillis. Investigation of the flame structure and nitrogen oxides formation in lean porous premixed combustion of natural

gas/hydrogen blends. *International Journal of Hydrogen Energy*, 33:4893–4905, 2008.

[24] S. K. Alavandi and A. K. Agrawal. Experimental study of combustion of hydrogen-syngas methane fuel mixtures in a porous burner. *International Journal of Hydrogen Energy*, 33:1407–1415, 2008.

[25] M. C. Lee, S. B. Seo, J. H. Chung, S. M. Kim, Y. J. Joo, and D. H. Ahn. Gas turbine combustion performance test of hydrogen and carbon monoxide synthetic gas. *Fuel*, 89:1485–1491, 2010.

[26] P. Therkelsen, T. Werts, V. G. McDonell, and G. S. Samuelsen. Analysis of nox formation in a hydrogen-fueled gas turbine engine. *Journal of Engineering for Gas Turbines and Power*, 131:031507, 2009.

[27] S. Daniele, P. Jansohn, and K. Boulouchos. Lean premixed combustion of undiluted syngas at gas turbine relevant conditions: Nox emissions and lean operational limits, gt2008-50265. In *Proceedings of ASME Turbo Expo 2008: Power for Land, Sea and Air, Berlin, Germany*, 2008.

[28] R. K. Cheng, D. Littlejohn, P. A. Strakey, and T. Sidwell. Laboratory investigations of a low-swirl injector with H_2 and CH_4 at gas turbine conditions. *Proceedings of the Combustion Institute*, 32:3001–3009, 2009.

[29] D. J. Beerer. Combustion characteristics and performance of alternative gaseous fuels at gas turbine engine conditions. Dissertation Prospectus for the Qualifying Examination.

[30] F. H. V. Coppens, J. De Ruyck, and A. A. Konnov. Effects of hydrogen enrichment on adiabatic burning velocity and NO formation in methane + air flames. *Experimental Thermal and Fluid Science*, 31:437–444, 2007.

[31] E. Hu, Z. Huang, J. Zheng, Q. Li, and J. He. Numerical study on laminar burning velocity and no formation of premixed methanehydrogenair flames. *International Journal of Hydrogen Energy*, 34:6545–6557, 2009.

[32] H. Guo, G. J. Smallwood, F. Liu, Y. Ju, and O. L. Gulder. The effect of reformate gas enrichment on extinction limits and NO_X formation in counterflow CH_4/air premixed flames. *Proceedings of the Combustion Institute*, 31:11971204, 2007.

[33] P. Griebel, E. Boschek, and P. Jansohn. Lean blowout limits and NO_X emissions of turbulent, lean premixed, hydrogen-enriched methane/air flames at high pressure. *Journal of Engineering for Gas Turbines and Power*, 129:404–410, 2007.

[34] M. Mintz, J. Han, M. Wang, and C. Saricks. Well-to-wheels analysis of landfill gas-based pathways and their addition to the greet model. Technical report, Argonne National Laboratory, 2010.

[35] W. Qin, F. N. Egolfopoulos, and T. T. Tsotsis. Fundamental and environmental aspects of landfill gas utilization for power generation. *Chemical Engineering Journal*, 82:157–172, 2001.

[36] A. M. ElKady, A. Evulet, A. Brand, T. P. Ursin, and A. Lynghjem. Application of exhaust gas recirculation in a DLN F-class combustion system for postcombustion carbon capture. *Journal of Engineering for Gas Turbines and Power*, 131, 2009.

[37] P. E. Røkke and J. E. Hustad. Exhaust gas recirculation in gas turbines for reduction of CO_2 emissions; combustion testing with focus on stability and emissions. *International Journal of Thermodynamics*, 8:167–173, 2005.

[38] H. Li, A. M. ElKady, and A. T. Evulet. Effect of exhaust gas recirculation on NO_X formation in premixed combustion system. In *47th AIAA Aerospace Sciences Meeting Including The New Horizons Forum and Aerospace Exposition*, 2009.

[39] D. Unger and H. Herzog. Comparative study on energy r&d performance: Gas turbine case study. Technical report, Massachusetts Institute of Technology Energy Laboratory, 1998.

[40] A. H. Lefebvre and D. R. Ballal. *Gas turbine combustion: alternative fuels and emissions.* Taylor & Francis: Boca Raton, 2010.

[41] Y. B. Zeldovich. The oxidation of nitrogen in combustion and explosions. *Acta Physicochemica USSR*, 21:577–628, 1946.

[42] P. C. Malte and D. T. Pratt. The role of energy-realeasing kinetics in NO_X formation: Fuel-lean, jet-stirred CO-air combustion. *Combustion Science and Technology*, 9:221–231, 1974.

[43] J. W. Bozzelli and A. M. Dean. O + NNH: A possible new route for NO_X formation in flames. *International Journal of Chemical Kinetics*, 27:1097–1109, 1995.

[44] C. P. Fenimore. Formation of nitric oxide in premixed hydrocarbon flames. In *Thirteenth Symposium (International) on Combustion, The Combustion Institute*, 1971.

[45] I. Glassman and R. A. Yetter. *Combustion: Fourth Edition.* Elsevier Inc., 2008.

[46] S. R. Turns. *An Introduction to Combustion, 2nd Edition.* McGraw-Hill Inc. New York, NY, 2000.

[47] URL `http://www.arb.ca.gov/energy/dg/dg.htm`.

[48] W. S. Y. Hung. Accurate method of predicting the effect of humidity or injected water on NO_X emissions from industrial gas turbines. In *ASME Paper 74-WA/ GT-6*, 1974.

[49] D. J. White, A. Batakis, R. T. Le Cren, and H. G. Yacabucci. Low NO_X combustion systems for burning heavy residual fuels and high fuel-bound nitrogen fuels. *Journal of Engineering for Gas Turbines and Power*, 104:377–385, 1982.

[50] J. P. Longwell and M. A. Weiss. High temperature reaction rates in hydrocarbon combustion. *Industrial & Engineering Chemistry*, 47:1634–1643, 1955.

[51] J. Zelina. *Combustion Studies in a Well-Stirred Reactor*. PhD thesis, University of Dayton, 1995.

[52] M. M. Thornton, P. C. Malte, and A. L. Crittenden. A well-stirred reactor for the study of pyrolysis and oxidation kinetics: Carbon monoxide and n-pentane oxidation. *Combustion Science and Technology*, 54:275–297, 1987.

[53] S. Singh. *A Study of Methanol Combustion and Oxides of Nitrogen Formation In A Jet-Stirred Reactor*. PhD thesis, Washington State University, 1978.

[54] R. C. Steele. *NO_X and N_2O Formation in Lean-Premixed Jet-Stirred Reactors Operated from 1 to 7 atm*. PhD thesis, University of Washington, 1995.

[55] T. R. Shuman. *NO_X and CO Formation For Lean-Premixed Methane-Air Combustion in a Jet-Stirred Reactor Operated at Elevated Pressure*. PhD thesis, University of Washington, 2000.

[56] W. M. Kays, M. E. Crawford, and B. Weigand. *Convective Heat and Mass Transfer*. McGraw-Hill Inc. New York, NY, 2005.

[57] F. P. Incropera, D. P. Dewitt, T. L. Bergman, and A. S. Lavine. *Introduction to Heat Transfer*. John Wiley & Sons, 2007.

[58] M. F. Modest. *Radiative Heat Transfer*. McGraw-Hill Inc. New York, NY, 1993.

[59] Greencast-94 plus product data sheet.

[60] M. F. Karalus, K. B. Fackler, I. V. Novosselov, J. C. Kramlich, and P. C. Malte. Characterizing the mechanism of lean blowout for a recirculation-stabilized premixed hydrogen flame: GT2012-68060. In *ASME Turbo Expo 2012, June 11-15, 2012, Copenhagen, Denmark.*

[61] B. E. Launder and D. B. Spalding. *Lectures in Mathematical Models of Turbulence.* Lectures in Mathematical Models of Turbulence, 1972.

[62] T. H. Shih, W. W. Liou, A. Shabbir, Z. Yang, and J. Zhu. A new k-ϵ eddy-viscosity model for high reynolds number turbulent flows - model development and validation. *Computers Fluids*, 24:227–238, 1995.

[63] B. E. Launder. Second-moment closure: Present... and future? *International Journal of of Heat and Fluid Flow*, 10:282–300, 1989.

[64] G. D. Raithby and E. H. Chui. A finite-volume method for predicting a radiant heat transfer in enclosures with participating media. *Journal of Heat Transfer*, 112:415–423, 1990.

[65] *ANSYS Fluent, Academic Research, Release 12.0.*

[66] D. G. Nicol, P. C. Malte, A. J. Hamer, R. J. Roby, and R. C. Steele. Development of a five-step global methane oxidation-NO formation mechanism for lean-premixed gas turbine combustion. In *Proceedings of the International Gas Turbine and Aeroengine Congress and Exhibition: Stockholm, Sweden*, 1998.

[67] B. F. Magnussen and B. H. Hjertager. On mathematical models of turbulent combustion with special emphasis on soot formation and combustion. In *Proceedings of the 16th International Symposium on Combustion.* The Combustion Institute, 1976.

[68] I. V. Novosselov. *Chemical Reactor Networks for Combustion Systems Modeling.* PhD thesis, University of Washington, 2006.

[69] D. T. Pratt, N. M. Marinov, and P. C. Malte. Chemical conversions within gas sampling probes. Technical report, University of Washington, 1992.

[70] J. C. Kramlich and P. C. Malte. Modeling and measurement of sample probe effects on pollutant gases drawn from flame zones. *Combustion Science and Technology*, 18:91–104, 1978.

[71] R. L. Hack and V. G. McDonell. Impact of ethane, propane, and diluent content in natural gas on the performance of a commercial microturbine combustor. *Journal of Engineering for Gas Turbines and Power*, 130, 2008.

[72] P. Glarborg and L. L. B. Bentzen. Chemical effects of a high CO_2 concentration in oxy-fuel combustion of methane. *Energy & Fuels*, 22:291–296, 2008.

[73] G. P. Smith, D. M. Golden, M. Frenklach, N. W. Moriarty, B. Eiteneer, M. Goldenberg, C. T. Bowman, R. K. Hanson, Jr. Song, S., W. C. Gardiner, V. V. Lissianski, and Z. Qin. GRI-Mech 3.0. URL `http://www.me.berkeley.edu/grimech/`.

[74] A. A. Konnov. Development and validation of a detailed reaction mechanism for the combustion of small hydrocarbons. *Syposium (International) on Combustion*, 28:317, 2000.

[75] Chemical-kinetic mechanisms for combustion applications, San Diego Mechanism web page, Mechanical and Aerospace Engineering (Combustion Research), University of California at San Diego. URL `http://web.eng.ucsd.edu/mae/groups/combustion/mechanism.html`.

[76] J. C. Hewson and M. Bollig. Reduced mechanisms for NO_X emissions from hydrocarbon diffusion flames. *26th Syposium (International) on Combustion*, 2: 2171–2179, 1996.

[77] C. V. Naik, K. V. Puduppakkam, A. Modak, E. Meeks, Y. L. Wang, Q. Feng, and T. T. Tsotsis. Detailed chemical kinetic mechanism for surrogates of alternative jet fuels. *Combustion and Flame*, 158:434–445, 2011.

[78] A. A. Konnov and J. De Ruyck. Temperature dependent rate constant for the reaction NNH + O → NH + NO. *Combustion and Flame*, 125:1258–1264, 2001.

[79] A. M. Elkady, D. M. Kalitan, J. Herbon, G. Leonard, R. Akula, H. Karim, and M. Hadley. Gas turbine emission characteristics in perfectly premixed combustion: Gt2011-46470. In *Proceedings of ASME Turbo Expo 2011, June 6-10, 2011, Vancouver, British Columbia, Canada.*

[80] F. Liu, H. Guo, and G. J. Smallwood. The chemical effect of CO_2 replacement of N_2 in air on the burning velocity of CH_4 and H_2 premixed flames. *Combustion and Flame*, 133:495–497, 2003.

[81] D. Dunn-Rankin, editor. *Lean Combustion: Technology and Control.* Elsevier Inc., 2008.

[82] G. Leonard and J. Stegmaier. Development of an aeroderivitive gas turbine dry low emissions combustion system. *Journal of Engineering for Gas Turbines and Power*, 116:542–546, 1994.

[83] K. B. Fackler. A study of pollutant formation from the lean premixed combustion of gaseous fuel alternatives to natural gas. General Exam.

[84] B. F. Magnussen. On the structure of turbulence and a generalized eddy dissipation concept for chemical reaction in turbulent flow. In *Nineteeth AIAA Meeting, St Louis*, 1981.

[85] I. R. Gran and B. F. Magnussen. A numerical study of a bluff-body stabilized diffusion flame. part 2. influence of combustion modeling and finite-rate chemistry. *Combustion Science and Technology*, 119, 1996.

[86] I. S. Ertesvag and B. F. Magnussen. The eddy dissipation turbulence energy cascade model. *Combustion Science and Technology*, 159:213–235, 2000.

[87] L. Kjäldman, A. Brink, and M. Hupa. Micro mixing time in the eddy dissipation concept. *Combustion Science and Technology*, 154:207–227, 2000.

[88] M. F. Karalus. Skeletal mechanism development for alternative gaseous fuels in lean-premixed combustion.

[89] T. F. Lu and C. K. Law. A directed relation graph method for mechanism reduction. *Proceedings of the Combustion Institute*, 30:1333–1341, 2005.

[90] P. C. Malte, S. C. Schmidt, and D. T. Pratt. Hydroxyl radical and atomic oxygen concentrations in high-intensity turbulent combustion. *Syposium (International) on Combustion*, 16:145–155, 1977.

[91] W. H. McAdams. *Heat Transmission, 3rd edition*. McGraw-Hill Inc. New York, NY, 1954.

Appendix A

CO OXIDATION IN THE SAMPLE PROBE

As discussed in Chapter 6, a significant amount of CO oxidation may take place in the sample probe. In this section the modelled CO results are compared to experimental results for 4 different cases: the variable temperature CH_4 data presented in Section 5.3, CH_4 mixed with both CO_2 and N_2 as presented in Section 5.7.1, and CH_4 mixed H_2 as presented in Section 5.7.2. All of the data for the above mentioned studies is from the nominal sampling location (2 mm inside the wall) within the recirculation zone; thus, it should be reasonable to apply the 62% correction that was done in Chapter 6.

A.1 Variable temperature CH_4 Combustion

The modelled and measured data for the temperature study performed on CH_4 is shown below in Figure A.1.
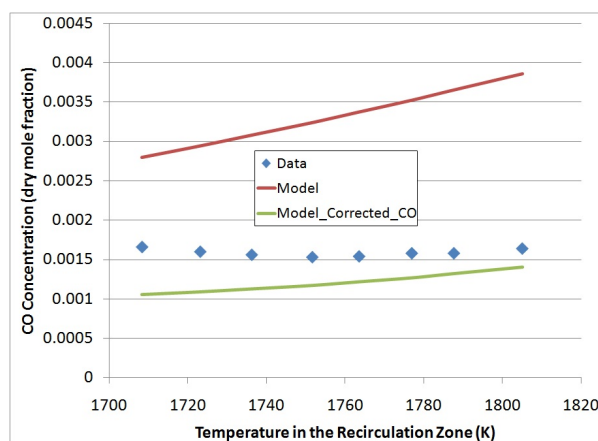
Figure A.1: CO concentrations as a function of temperature for CH_4 combustion

As shown above, the correction is fairly accurate for higher temperatures, but it diverges at lower temperatures. This is potentially due to a lower OH concentration at low temperature.

A.2 CH_4 mixed with N_2

The modelled and measured data for CH_4 mixed with N_2 is shown below in Figure A.2.
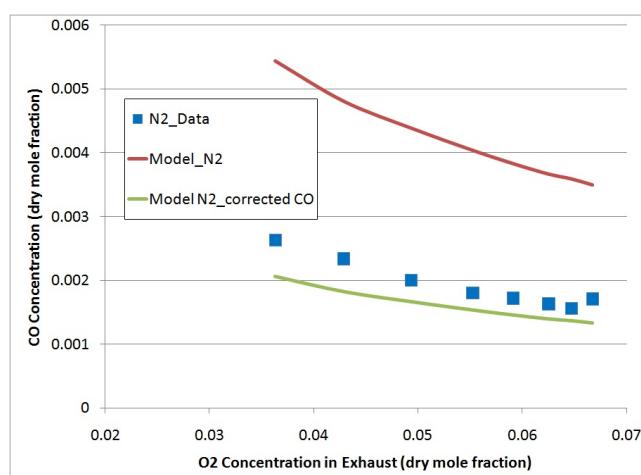
Figure A.2: CO concentrations as a function of O_2 concentration in the exhaust for CH_4 mixed with N_2 combustion

Similar to the results shown for pure CH_4 combustion, the 62% correction does a reasonably good job at predicting the measured CO data. It does a better job with pure CH_4 than it does at the highest level of N_2 dilution.

A.3 CH_4 mixed with CO_2

The modelled and measured data for CH_4 mixed with CO_2 is shown below in Figure A.3. Unlike the previous two corrections, the 62% correction for the modelled CO considerably under predicts the data. In spite of this, the uncorrected model barely over predicts the data. We believe that the same chemical effect that is responsible for

less NO_X production in the current study is responsible for this phenomena. Essentially, the high CO_2 concentration is balancing out the tendency for CO oxidation in the probe, which in turn causes the modelled and measured CO data to look similar. Note that the corrected model predicts pure CH_4 CO emission well, and this model diverges as more CO_2 is added to the system.
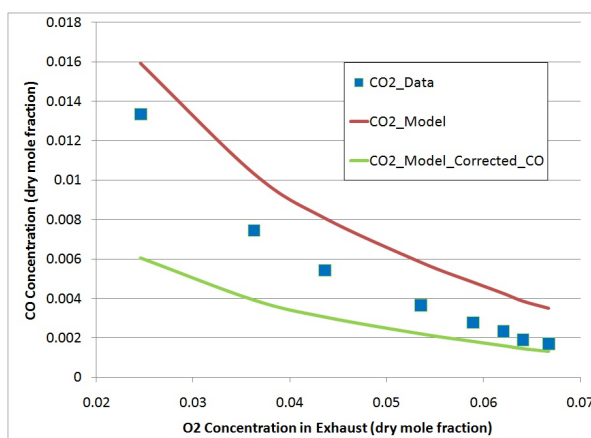
Figure A.3: CO concentrations as a function of O_2 concentration in the exhaust for CH_4 mixed with CO_2 combustion

A.4 CH_4 mixed with H_2

The modelled and measured data for CH_4 mixed with CO_2 is shown below in Figure A.4. Like the variable temperature CH_4 data and the data shown for CH_4 mixed with N_2, the corrected CO model predicts the data quite well. Similar to the results shown above, the correction does a better job at pure CH_4 than it does as H_2 is added to the system with the exception of pure H_2 of course.
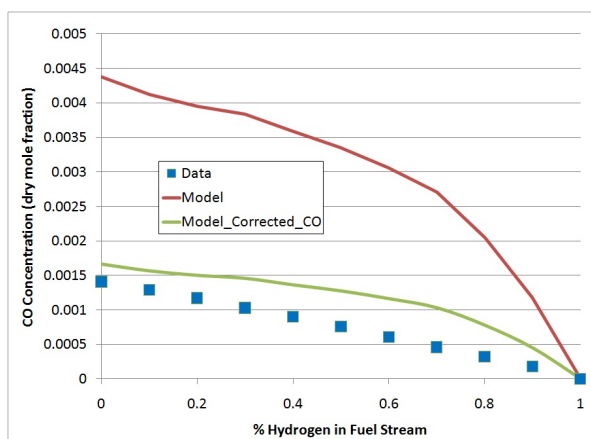
Figure A.4: CO concentrations as a function of $H_2\%$ in the fuel stream for CH_4 mixed with H_2 combustion

The results shown above as well as the CFD results shown in Chapter 6 strongly suggest that there is a fairly significant amount of CO oxidation occurring in the sample probe. This most definitely needs to be further investigated.

Appendix B

EMISSION INDEX VS. CORRECTION TO 15% O_2

When comparing emissions between fuels with large diluent composition, it is decided to express the emissions as an emission index since it removes ambiguity associated with O_2 content in the exhaust. However, it has been suggested that emission index may not be the best way to express the data [36]. The emissions index can be written as in Equation B.1, where: EI_{NO_X} is the Emission Index of NO_X in (grams NO_X/ kg fuel), $X_{i,dry}$ is the measured dry mole fraction of species i, $N_{mix,dry}$ is the number of moles in a mixture, and MW_i is the molecular weight of species i in kg/kmole.

$$EI_{NO_X} = \frac{X_{NO_X} MW_{NO_2} N_{mix,dry}}{MW_{fuel}} \tag{B.1}$$

Recently, Elkady et al. have derived a NO_X correction to 15% O_2 that is based on an oxidizer composed of O_2, N_2, and CO_2 as shown in Equation B.2, where x and y are the number of carbon and hydrogen moles in a hydrocarbon fuel C_xH_y and α, β, γ are the mole fractions of O_2, N_2, and CO_2, respectively [36]. This procedure in essence corrects the NO_X concentration for both stoichiometry (to a common 15% O_2) and for dilution (to 21% O_2 in the oxidant).

$$C_xH_y + a(O_2 + \tfrac{\beta}{\alpha}N_2 + \tfrac{\gamma}{\alpha}CO_2) \rightarrow (x + a\tfrac{\gamma}{\alpha})CO_2 + \tfrac{y}{2}H_2O$$
$$+bO_2 + a\tfrac{\beta}{\alpha}N_2 \tag{B.2}$$
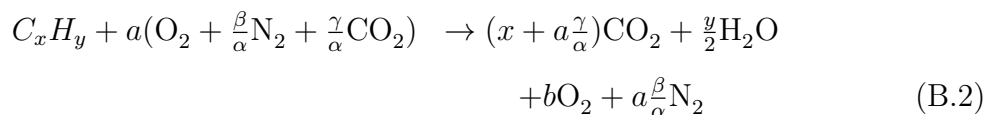
For CH_4 as the fuel, the revised NO_X concentration corrected to 15% O_2 is given in Equation B.3 [36].

$$X_{NO_X,15\%O_2} = X_{NO_X}(0.033231)(\frac{2-\alpha}{\alpha - X_{O_2}}) \tag{B.3}$$

From Equation B.2, the number of moles in the dry product stream can be derived, which is shown in Equation B.4.

$$N_{mix,dry} = \frac{x + \frac{y}{4}(1 - X_{O_2,dry})}{\alpha - X_{O_2,dry}} - \frac{y}{4} \tag{B.4}$$

For CH_4 as the fuel, Equations B.1 and B.4 can be combined as shown in Equation B.5, which is clearly a multiple of Equation B.3. Thus, the two approaches are equivalent in expressing NO_X emissions, while removing the effects of both stoichiometry and dilution.

$$EI_{NO_X} = \frac{X_{NO_X} MW_{NO_2}}{MW_{fuel}} \left(\frac{2 - \alpha}{\alpha - X_{O_2}} \right) \tag{B.5}$$

The above derivation was made possible after realizing that there is an error in Equation 2 in reference: [36]. The equation is multiplied by a factor of 0.0595 that should not be there.

Appendix C

THERMOCOUPLE CORRECTIONS

An R-type thermocouple (TC) has been used for all temperature measurements within the combustion chamber. Shown in the TC analysis by Lee [8], the measured TC temperature is less than the gas temperature mainly due to radiative losses to the colder reactor wall and reactor cold spots (the jet and drain holes). As shown in Equation C.1, heat can be transferred to the TC bead by the hot combustion gases and from the catalytic oxidation of CO at the Pt/Rh interface. Heat can be transferred away from the TC bead by conduction through the wires and sheath and radiation to the reactor wall and cold spots [8].

$$Q_{conv} + Q_{cat} = Q_{rad} + Q_{cond} \tag{C.1}$$

Lee shows that catalytic effects are negligible when a thin ceramic coating is applied to the bead [8]. Singh shows that conduction effects are negligible when small (< 0.12 in. diameter) TC wires are used. The R-type TC wires used in the present study were manufactured by Omega Engineering Inc., have a diameter of 0.01 in. and the specific part numbers are shown below in Table C.1.

Table C.1: R-Type TC wires used in the present study.

Material	Diameter (in)	Part Number
100% Pt	0.01	SPPL-010
87% Pt/13% Rh	0.01	SP13RH-010

The TC bead is coated with a non-catalytic ceramic coating: Ceramabond 569. Both catalytic and conduction effects are neglected and the resulting heat transfer

balance is composed of convection and radiation only as shown in Equation C.2.

$$Q_{conv} = Q_{rad} \qquad (C.2)$$

C.1 Convection

The convective term in Equation C.2 is given by Equation C.3, where:

- A_{tip} is the surface area of the TC bead, which is approximated as a sphere and is nominally 1 mm in diameter.

- h_{tip} is the convective heat transfer coefficient to the TC bead

- T_{gas} is the actual gas temperature.

- T_{tip} is the measured TC temperature.

$$Q_{conv} = A_{tip} * h_{tip} * (T_{gas} - T_{tip}) \qquad (C.3)$$

The convective heat transfer coefficient, h_{tip}, is given by Equation C.4, where:

- Nu_D is the Nusselt number for flow around a sphere.

- k_{air} is the thermal conductivity of air at the combustion gas temperature, T_{gas}.

- D is diameter of the TC bead (nominally 1 mm).

$$h_{tip} = Nu_D * \frac{k_{air}}{D} \qquad (C.4)$$

The Nusselt number is given by Equation C.5 for flow around a sphere at Reynolds numbers between 17 and 70,000 [91], where:

- V is the bulk fluid velocity flowing over the TC bead, which is determined by CFD. It is 65 m/s at the nominal temperature measurement location.

- ν_{air} is the viscosity of air at the combustion gas temperature, T_{gas}.

$$Nu_D = 0.37 * \left(\frac{V * D}{\nu_{air}} \right)^{0.6} \tag{C.5}$$

C.2 Radiation

Following an analysis by Lee [8], the three-body radiation interaction between the TC bead, the reactor wall, and the reactor cold spots is given in Equation C.6, where:

- σ is the Stefan-Boltzmann constant (5.67E-8 W/m^2 − K^4),

- ε_{tip} is the emissivity of the TC tip.

- $F_{tip-wall,hot}$ and $F_{tip-wall,cold}$ are the view factors of the TC bead to the hot and cold portions of the reactor wall, respectively,

- $\varepsilon_{wall,hot}$ and $\varepsilon_{wall,cold}$ are the emissivities of the hot and cold portions of the reactor wall, respectively,

- $T_{wall,hot}$ and $T_{wall,cold}$ are the temperatures of the hot and cold portions of the reactor wall, respectively.

$$
\begin{aligned}
Q_{rad} \quad = \quad & \sigma * A_{tip} * \varepsilon_{tip} * [T_{tip}^4 - \\
& (F_{tip-wall,hot} * \varepsilon_{wall,hot} * T_{wall,hot}^4 + \\
& F_{tip-wall,cold} * \varepsilon_{wall,cold} * T_{wall,cold}^4)]
\end{aligned}
\tag{C.6}
$$

From Lee [8], the estimated view factor of the TC bead to the cold reactor wall, $F_{tip-wall,cold}$, is 0.05; thus $F_{tip-wall,hot}$ is 0.95. The TC bead is assumed to be a small body in a large enclosure; thus both $\varepsilon_{wall,hot}$ and $\varepsilon_{wall,cold}$ are assumed to be unity. The average temperature of the cold spots on the reactor wall, $T_{wall,cold}$, is assumed to be 1000 K [8]. The average temperature of the reactor wall is calculated by 3D CFD to be between 1550 and 1475 K. The 2D CFD simulations calculate the wall temperature to be about 1400 K. When running at similar conditions (temperatures/pressures) to the experiments in this study, other JSR researchers measured the temperature of the 16cc JSR wall with an optical pyrometer to be 1563 K [54] and 1608 K [8], respectively. Given the wide range of measured and calculated wall temperatures and the uncertanties associated with both measuring the wall temperature with an optical pyrometer and calculating the wall temperature with CFD, it is decided to use a nominal value of $T_{wall,hot}$ equal to 1500 K. Lee measured the value of ε_{tip} by varying the emissivity setting on the optical pyrometer until the measured temperature by the TC was equal to the temperature measured by the pyrometer [8]. The measured value of ε_{tip} was 0.258, and this value is used in this study.

Appendix D

16 CC REACTOR SCANS

Table D.1: 100% CH$_4$

Date	1/22/2010	Composition											
Phi	0.720	H2	CO	CH4	CO2	N2	C2H6	C3H8					
		0	0	1	0	0	0	0					
position (mm)	0	1	2	3	4	5	6	7	8	9	10	11	12
T (K)	1427.2	1568.5	1625.1	1719.2	1763	1785.1	1796.9	1801.5	1806	1809.1	1808.9	1799.9	1767.8
O2 (vol%)	13.13	8.82	6.72	6.52	6.47	6.42	6.42	6.42	6.42	6.42	6.42	6.37	6.37
CO (vol%)	0.47	0.95	0.62	0.36	0.26	0.21	0.19	0.19	0.2	0.22	0.23	0.25	0.26
CO2 (vol%)	3.3	5.02	7.26	7.67	7.78	7.85	7.86	7.85	7.84	7.8	7.78	7.76	7.74
NOx (ppm)	5.05	7.58	10.2	11.11	11.36	11.62	11.62	11.62	11.36	11.36	11.36	11.36	11.11

Table D.2: Mix 1

Date	1/24/2010	Composition											
Phi	0.607	H2	CO	CH4	CO2	N2	C2H6	C3H8					
		1	0	0	0	0	0	0					
position (mm)	0	1	2	3	4	5	6	7	8	9	10	11	12
T (K)	1782.6	1797.9	1810.3	1812.9	1809.1	1806.2	1804.7	1805.7	1808	1809.7	1813	1814.7	1809.9
O2 (vol%)	9.47	9.47	9.47	9.42	9.42	9.42	9.42	9.42	9.42	9.42	9.42	9.42	9.42
CO (vol%)	0	0	0	0	0	0	0	0	0	0	0	0	0
CO2 (vol%)	0	0	0	0	0	0	0	0	0	0	0	0	0
NOx (ppm)	5.86	6.06	6.46	6.67	6.87	6.87	7.07	7.07	7.07	7.07	7.17	7.07	7.07

Table D.3: Mix 2A

Date	3/5/2010	Composition											
Phi	0.685	H2	CO	CH4	CO2	N2	C2H6	C3H8					
		0.25	0	0.5	0	0	0.25	0					
position (mm)	0	1	2	3	4	5	6	7	8	9	10	11	12
T (K)	1360.5	1515.4	1643.4	1732	1786.2	1801.7	1806.6	1809.4	1810.5	1812.2	1814.2	1814.3	1808
O2 (vol%)	7.10	7.10	7.05	7.00	7.00	7.00	7.00	7.00	7.00	7.00	7.00	7.00	7.00
CO (vol%)	0.99	0.52	0.35	0.25	0.19	0.16	0.15	0.15	0.16	0.18	0.19	0.20	0.21
CO2 (vol%)	6.67	7.20	7.38	7.48	7.54	7.58	7.60	7.60	7.58	7.57	7.55	7.53	7.53
NOx (ppm)	7.88	9.90	10.86	10.86	11.11	11.11	11.36	11.36	11.11	11.11	11.11	10.86	10.86

Table D.4: Mix 2B

Date	3/8/2010	Composition											
Phi	0.685	H2	CO	CH4	CO2	N2	C2H6	C3H8					
		0.25	0	0.65	0	0	0.1	0					
position (mm)	0	1	2	3	4	5	6	7	8	9	10	11	12
T (K)	1465.6	1553.1	1668.9	1739.9	1780.6	1794.7	1802.2	1804.7	1806.7	1808.9	1811.6	1810.5	1800.4
O2 (vol%)	7.02	7.10	7.10	7.09	7.04	7.05	7.07	7.03	7.02	7.08	7.09	7.05	7.02
CO (vol%)	0.33	0.25	0.19	0.15	0.13	0.11	0.11	0.11	0.12	0.12	0.13	0.13	0.14
CO2 (vol%)	7.18	7.18	7.23	7.27	7.30	7.29	7.29	7.31	7.30	7.25	7.26	7.26	7.29
NOx (ppm)	8.91	9.01	9.31	9.51	9.51	9.31	9.21	9.21	9.11	8.91	8.91	8.91	8.91

Table D.5: Mix 2C

Date	3/1/2010	Composition											
Phi	0.668	H2	CO	CH4	CO2	N2	C2H6	C3H8					
		0.55	0	0.35	0	0	0.1	0					
position (mm)	0	1	2	3	4	5	6	7	8	9	10	11	12
T (K)	1665.7	1693.3	1748.2	1782.7	1797.7	1802.2	1803.6	1804.1	1804.2	1805.4	1807.2	1805.9	1783.6
O2 (vol%)	7.54	7.52	7.57	7.55	7.56	7.58	7.56	7.56	7.52	7.54	7.56	7.54	7.52
CO (vol%)	0.25	0.19	0.14	0.11	0.09	0.08	0.07	0.08	0.08	0.09	0.09	0.1	0.1
CO2 (vol%)	6.11	6.15	6.15	6.2	6.19	6.18	6.19	6.2	6.19	6.18	6.18	6.18	6.18
NOx (ppm)	7.98	8.48	8.48	8.48	8.48	8.38	8.38	8.38	8.28	8.18	8.08	8.08	8.08

Table D.6: Mix 3

Date	2/3/2010	Composition											
Phi	0.57	H2	CO	CH4	CO2	N2	C2H6	C3H8					
		0.4	0.5	0	0.1	0	0	0					
position (mm)	0	1	2	3	4	5	6	7	8	9	10	11	12
T (K)	1727.4	1766.3	1783.8	1792.6	1796.2	1798.7	1800.1	1802.1	1804.4	1806.7	1805.4	1787.6	1776
O2 (vol%)	9.02	9.02	9.02	9.02	8.97	8.97	8.92	8.92	8.92	8.92	8.92	8.92	8.92
CO (vol%)	0.78	0.65	0.50	0.35	0.27	0.23	0.21	0.20	0.21	0.22	0.24	0.25	0.26
CO2 (vol%)	10.98	11.09	11.23	11.39	11.42	11.47	11.51	11.51	11.51	11.47	11.45	11.43	11.41
NOx (ppm)	6.26	6.97	7.88	8.69	8.99	9.09	9.29	9.39	9.29	9.19	9.19	9.09	8.99

Table D.7: Mix 4A

Date	2/10/2010	Composition											
Phi	0.816	H2	CO	CH4	CO2	N2	C2H6	C3H8					
		0	0	0.5	0.35	0.15	0	0					
position (mm)	0	1	2	3	4	5	6	7	8	9	10	11	12
T (K)	1257.3	1334.5	1432.4	1552.2	1665.4	1744.2	1779.4	1793.4	1800.2	1804.1	1807	1808.3	1806.2
O2 (vol%)	12.23	9.82	4.81	4.21	4.11	4.06	4.01	4.01	4.01	4.06	4.06	4.06	4.11
CO (vol%)	0.51	0.87	1.15	0.72	0.55	0.48	0.45	0.45	0.47	0.50	0.54	0.56	0.59
CO2 (vol%)	8.53	9.64	12.65	13.73	13.96	14.08	14.09	14.12	14.05	14.00	13.63	13.62	13.60
NOx (ppm)	5.25	7.27	10.61	12.12	12.63	12.63	12.63	12.63	12.63	12.63	12.63	12.37	12.12

Table D.8: Mix 4B

Date	1/22/2010	Composition											
Phi	0.838	H2	CO	CH4	CO2	N2	C2H6	C3H8					
		0	0	0.5	0.5	0	0	0					
position (mm)	0	1	2	3	4	5	6	7	8	9	10	11	12
T (K)	1437.9	1584.2	1677.5	1745.4	1780	1796.1	1802.2	1804.2	1805.5	1806.6	1800.6	1777.1	1760.3
O2 (vol%)	11.83	7.52	4.41	3.91	3.81	3.81	3.76	3.76	3.76	3.76	3.76	3.76	3.76
CO (vol%)	0.60	1.24	1.18	0.86	0.69	0.61	0.57	0.57	0.60	0.65	0.68	0.72	0.75
CO2 (vol%)	10.96	12.80	15.00	15.76	16.00	16.08	16.10	16.10	16.02	15.97	15.93	15.89	15.85
NOx (ppm)	5.25	8.18	11.11	12.12	12.63	12.63	12.63	12.37	12.37	12.37	12.12	12.12	12.12

Table D.9: Mix 4C

Date	1/31/2010	Composition											
Phi	0.816	H2	CO	CH4	CO2	N2	C2H6	C3H8					
		0	0	0.5	0	0.5	0	0					
position (mm)	0	1	2	3	4	5	6	7	8	9	10	11	12
T (K)	1287.8	1431.6	1573.4	1681.4	1745.4	1782.5	1795.5	1798.1	1803.8	1806.7	1808.7	1807.2	1799.4
O2 (vol%)	11.37	8.78	4.29	3.79	3.69	3.69	3.69	3.69	3.69	3.69	3.69	3.69	3.79
CO (vol%)	0.42	0.76	0.92	0.53	0.38	0.32	0.29	0.29	0.30	0.33	0.35	0.38	0.40
CO2 (vol%)	2.95	3.90	6.67	7.45	7.67	7.70	7.74	7.75	7.71	7.67	7.64	7.62	7.59
NOx (ppm)	6.44	8.91	11.88	12.87	13.37	13.62	13.86	13.86	13.62	13.62	13.62	13.37	13.37

Table D.10: Mix 5A

Date	3/5/2010	Composition											
Phi	0.710	H2	CO	CH4	CO2	N2	C2H6	C3H8					
		0	0	0.95	0	0	0.05	0					
position (mm)	0	1	2	3	4	5	6	7	8	9	10	11	12
T (K)	1282.5	1433.5	1611.2	1699.4	1768.3	1793.7	1803.4	1807.7	1809.3	1810.9	1812.7	1812.9	1806.8
O2 (vol%)	12.10	7.00	6.90	6.80	6.80	6.80	6.80	6.80	6.80	6.80	6.80	6.80	6.80
CO (vol%)	0.61	0.92	0.46	0.31	0.23	0.19	0.18	0.18	0.20	0.21	0.23	0.24	0.25
CO2 (vol%)	3.22	6.68	7.51	7.68	7.79	7.82	7.84	7.84	7.84	7.83	7.81	7.79	7.77
NOx (ppm)	5.25	9.19	10.61	11.11	11.36	11.36	11.36	11.36	11.36	11.36	11.36	11.11	11.11

Table D.11: Mix 5B

Date	4/7/2010	Composition											
Phi	0.713	H2	CO	CH4	CO2	N2	C2H6	C3H8					
		0	0	0.85	0	0	0.15	0					
position (mm)	0	1	2	3	4	5	6	7	8	9	10	11	12
T (K)	1237.2	1376.5	1568.6	1697.3	1767.3	1792	1801	1803.4	1805.6	1807.2	1809.6	1811	1804.5
O2 (vol%)	7.58	6.98	6.88	6.78	6.78	6.78	6.78	6.78	6.78	6.78	6.78	6.78	6.78
CO (vol%)	0.92	0.78	0.43	0.29	0.23	0.20	0.18	0.18	0.19	0.21	0.22	0.23	0.24
CO2 (vol%)	3.62	7.21	7.65	7.79	7.88	7.90	7.92	7.92	7.89	7.87	7.88	7.85	7.84
NOx (ppm)	5.30	7.80	10.40	11.20	11.50	11.70	11.70	11.70	11.70	11.45	11.45	11.35	11.20

Table D.12: Mix 5C

Date	3/7/2010	Composition											
Phi	0.702	H2	CO	CH4	CO2	N2	C2H6	C3H8					
		0	0	0.75	0	0	0.25	0					
position (mm)	0	1	2	3	4	5	6	7	8	9	10	11	12
T (K)	1293.5	1434.4	1592.5	1706.3	1768.1	1788.8	1796.3	1800.3	1801.6	1803.3	1805.9	1805.4	1796.8
O2 (vol%)	7.1	7	7	6.9	6.9	6.9	6.9	6.9	6.9	6.9	6.9	6.9	6.9
CO (vol%)	1.26	0.69	0.41	0.29	0.22	0.19	0.18	0.18	0.19	0.21	0.22	0.24	0.25
CO2 (vol%)	3.85	7.41	7.75	7.85	7.93	7.98	7.98	7.98	7.95	7.93	7.93	7.89	7.87
NOx (ppm)	6.26	10.1	11.11	12.12	12.12	12.12	12.12	12.12	12.12	11.62	11.62	11.11	11.11

Appendix E

PARAMETER STUDIES

Table E.1: Parameter Studies

% CH4	% CO2	Phi	Temperature (K)	CO (vol%)	CO2 (vol%)	O2 (vol%)	NOx (ppm)
100.0%	0.0%	0.71	1800.3	0.171	7.82	6.4	11.25
90.1%	9.9%	0.72	1799.96	0.19	8.66	6.24	11
80.0%	20.0%	0.73	1800.64	0.232	9.72	6.2	11
70.1%	29.9%	0.74	1800.84	0.278	11.05	5.98	11.5
60.1%	39.9%	0.76	1800.42	0.366	13	5.26	12
50.0%	50.0%	0.81	1800.9	0.542	15.74	4.24	12.75
45.0%	55.0%	0.85	1801.11	0.744	17.85	3.5	13.5
40.0%	60.0%	0.92	1801.24	1.334	20.97	2.32	15.5
% CH4	% N2	Phi	Temperature (K)	CO (vol%)	CO2 (vol%)	O2 (vol%)	NOx (ppm)
100.0%	0.0%	0.71	1800.43	0.171	7.82	6.4	11.25
90.1%	9.9%	0.72	1799.73	0.156	7.84	6.25	11.5
79.9%	20.1%	0.73	1800.92	0.163	7.87	5.96	12
69.9%	30.1%	0.74	1801.3	0.172	7.87	5.7	12.25
60.0%	40.0%	0.75	1799.88	0.18	7.86	5.24	12.5
50.0%	50.0%	0.77	1801.3	0.2	7.83	4.6	13.5
40.1%	59.9%	0.8	1801.61	0.234	7.78	3.85	14.5
34.8%	65.2%	0.83	1801.11	0.263	7.76	3.14	16.25
% CH4	% H2	Phi	Temperature (K)	CO (vol%)	CO2 (vol%)	O2 (vol%)	NOx (ppm)
100.0%	0.0%	0.71	1801.1	0.141	7.66	6.68	11.5
89.9%	10.1%	0.74	1800.3	0.129	7.43	6.77	11
80.1%	19.9%	0.73	1800.3	0.117	7.18	6.86	10.5
70.1%	29.9%	0.72	1800.5	0.103	6.84	7.02	10
60.1%	39.9%	0.71	1800.4	0.09	6.48	7.18	9.7
50.0%	50.0%	0.7	1800.3	0.076	6	7.4	9.2
40.0%	60.0%	0.69	1800.2	0.061	5.36	7.68	8.8
29.9%	70.1%	0.69	1800.5	0.046	4.52	7.99	8.1
19.9%	80.1%	0.63	1800.4	0.032	3.66	8.44	7.7
10.0%	90.0%	0.59	1800.4	0.018	2.4	8.91	7.2
0.0%	100.0%	0.59	1800.4	0	0	9.82	6.86
% CH4	% CO	Phi	Temperature (K)	CO (vol%)	CO2 (vol%)	O2 (vol%)	NOx (ppm)
100.0%	0.0%	0.72	1801.2	0.203	7.7	6.56	11.5
90.1%	9.9%	0.72	1801.5	0.218	8.16	6.62	12
79.9%	20.1%	0.71	1801.6	0.236	8.73	6.73	12.25
70.2%	29.8%	0.7	1801.2	0.257	9.34	6.87	12
59.6%	40.4%	0.68	1801.8	0.288	10.11	6.94	11.75
49.6%	50.4%	0.67	1801.7	0.324	10.96	7.06	12
40.1%	59.9%	0.66	1801.6	0.373	11.92	7.23	12.25
29.9%	70.1%	0.64	1801.4	0.452	13.17	7.42	13
20.0%	80.0%	0.62	1801.7	0.61	14.79	7.51	14.5
9.9%	90.1%	0.6	1801.5	0.924	16.93	7.72	19
% CH4	% C2H6	Phi	Temperature (K)	CO (vol%)	CO2 (vol%)	O2 (vol%)	NOx (ppm)
100.0%	0.0%	0.7	1799	0.197	7.41	6.98	11
90.0%	10.0%	0.7	1800.5	0.204	7.54	7	11.5
79.9%	20.1%	0.69	1800	0.212	7.64	7.1	12
70.0%	30.0%	0.69	1800.3	0.216	7.75	7.15	12.25
60.0%	40.0%	0.69	1800.5	0.219	7.83	7.2	12.5
50.0%	50.0%	0.69	1800.6	0.222	7.9	7.25	12.75
39.9%	60.1%	0.69	1801	0.228	7.96	7.3	13
29.9%	70.1%	0.69	1801	0.232	8	7.35	13.25
19.9%	80.1%	0.68	1801	0.241	8.05	7.4	13.5
10.3%	89.7%	0.68	1801	0.247	8.1	7.42	13.75
0.0%	100.0%	0.69	1801.2	0.254	8.14	7.42	14

Appendix F

TEMPERATURE VARIATION

Table F.1: Temperature Variations for Pure Fuels

CH4					
Phi	Temperature (K)	CO (vol%)	CO2 (vol%)	O2 (vol%)	NOx (ppm)
0.71	1805.1	0.244	7.88	6.8	11.4
0.7	1787.7	0.238	7.68	7.1	10
0.69	1777	0.238	7.57	7.3	9.3
0.68	1763.6	0.234	7.45	7.5	8.4
0.67	1751.7	0.233	7.33	7.6	7.6
0.66	1736.3	0.236	7.18	7.9	6.9
0.65	1723.2	0.24	7.18	8.1	6.4
0.64	1708.4	0.246	6.93	8.4	5.7
C2H6					
Phi	Temperature (K)	CO (vol%)	CO2 (vol%)	O2 (vol%)	NOx (ppm)
0.69	1811	0.149	8.32	7	12.6
0.67	1791.5	0.14	8.13	7.34	11.0
0.66	1776.6	0.134	7.99	7.6	9.9
0.65	1763.7	0.128	7.85	7.77	9.0
0.64	1750.4	0.126	7.74	8.01	8.2
0.63	1741.7	0.124	7.65	8.1	7.7
0.62	1727.3	0.121	7.52	8.31	7.0
0.61	1716.2	0.12	7.41	8.48	6.6
0.61	1708.1	0.119	7.31	8.64	6.2
C3H8					
Phi	Temperature (K)	CO (vol%)	CO2 (vol%)	O2 (vol%)	NOx (ppm)
0.67	1809.5	0.117	8.65	7.42	13.9
0.66	1794.1	0.112	8.46	7.71	12.0
0.65	1784.2	0.109	8.35	7.87	11.0
0.64	1771.6	0.107	8.23	8.04	10.0
0.63	1759.6	0.106	8.11	8.23	9.2
0.62	1745.5	0.105	7.99	8.38	8.3
0.62	1738.7	0.106	7.91	8.5	7.9
0.61	1729.5	0.106	7.81	8.64	7.5
0.60	1717.5	0.107	7.7	8.82	6.9
0.59	1703	0.109	7.57	9.02	6.2
H2					
Phi	Temperature (K)	CO (vol%)	CO2 (vol%)	O2 (vol%)	NOx (ppm)
0.60	1808.4	0	0	9.75	6.9
0.59	1791.5	0	0	10.01	5.7
0.57	1772.6	0	0	10.23	4.6
0.57	1761	0	0	10.32	4.1
0.56	1750.5	0	0	10.46	3.6
0.55	1734.6	0	0	10.63	3.1
0.54	1722.6	0	0	10.78	2.7
0.54	1708.2	0	0	10.96	2.3

Appendix G

64 CC JSR

Table G.1: A summary of the experimental tests conducted on the 64 cc JSR

Mixture	Composition	1490 C (1800 K)*	1400 C (1700K)*	1300 C (1590 K)*	Blow Out (deg C)
0	100% CH_4	10	5	NA	1337
1	55% CH_4, 30% C_3H_8, 15% C_4H_{10}	4	NA	NA	1417
2	74% CH_4, 18% C_3H_8, 8% C_4H_{10}	4	2	NA	1387
3	80% CH_4, 20% C_3H_8	7	3	NA	1367
4	75% CH_4, 5% C_3H_8, 15% CO_2, 5% N_2	4	2	NA	1363
5	65% CH_4 5% CO_2 30% H_2	4	2	2	1140
6	45% CH_4 5% CO_2 50% H_2	4	2	2	1010
7	75% CH_4 25% CO_2	5	3	NA	1352
8	65% CH_4, 25% CO_2, 10% CO	4	2	NA	1373
9	50% CH_4, 50% CO_2	5	3	NA	1368
10	25% CH_4, 10% CO_2, 54% H_2, 11% CO	2	1	1	1086
11	10% CH_4 32% H_2, 58% CO	1	x	1	1205
12	100% C_3H_8	5	NA	NA	1418

Table G.2: Mixture 0

Mixture 0													
Date	tau (ms)	MW	C	H	O	C/H ratio	stoich F/A						
3/22/2007	3.98	16.043	1	4	0	0.25	0.058						
	R (mm)	0	2	4	6	8	10	12	14	16	18	20	22
NOx	ppm	1.53	4.49	7.34	8.16	8.65	8.82	8.83	8.86	8.8	8.85	8.89	8.89
CO	%	0.44	1.02	0.95	0.47	0.26	0.15	0.1	0.08	0.08	0.08	0.08	0.09
CO2	%	1.19	3.28	5.79	6.81	7.1	7.2	7.24	7.26	7.26	7.25	7.25	7.25
O2	%	17.61	12.94	9.19	8.38	8.27	8.17	8.17	8.17	8.17	8.17	8.17	8.17
NOx - 15% O2	ppm	2.73	3.34	3.71	3.86	4.06	4.11	4.11	4.12	4.1	4.12	4.14	4.14
T (K)		860.5	951	1326	1600.5	1725.7	1769.4	1778.7	1782.4	1783.9	1789.6	1800.5	1808.2

Table G.3: Mixture 1

Mixture 1													
Date	tau (ms)	MW	C	H	O	C/H ratio	stoich F/A						
9/13/2007	4.16	30.77	2.05	6.1	0	0.3361	0.0625						
	R (mm)	0	2	4	6	8	10	12	14	16	18	20	22
NOx	ppm	2.03	3.96	6.29	7.41	8.12	8.53	8.93	9.54	10.56	10.35	9.95	9.54
CO	%	0.85	1.97	1.38	0.92	0.63	0.47	0.35	0.26	0.12	0.09	0.10	0.10
CO2	%	1.01	3.91	6.23	6.98	7.31	7.46	7.60	7.70	7.89	7.90	7.90	7.88
O2	%	11.42	9.19	8.98	8.78	8.63	8.58	8.58	8.58	8.43	8.43	8.43	8.48
NOx - 15% O2	ppm	1.21	1.85	2.96	3.49	3.82	4.02	4.24	4.54	4.99	4.90	4.71	4.53
T (K)		916.8	1056.3	1163.1	1296.9	1428.6	1552.0	1641.7	1701.9	1782.0	1792.6	1797.6	1808.9

Table G.4: Mixture 2

Mixture 2													
Date	tau (ms)	MW	C	H	O	C/H ratio	stoich F/A						
9/19/2007	4.19	24.46	1.60	5.20	0.00	0.3077	0.0613						
	R (mm)	0	2	4	6	8	10	12	14	16	18	20	22
NOx	ppm	1.82	3.33	5.45	6.67	7.37	7.88	8.58	9.29	9.90	9.59	9.29	9.09
CO	%	0.65	1.49	1.54	0.98	0.67	0.46	0.33	0.25	0.11	0.09	0.09	0.10
CO2	%	1.01	2.78	5.51	6.65	7.01	7.27	7.40	7.55	7.68	7.69	7.67	7.63
O2	%	16.80	9.90	8.88	8.78	8.68	8.58	8.48	8.38	8.38	8.32	8.38	8.38
NOx - 15% O2	ppm	2.42	1.68	2.53	3.13	3.48	3.72	4.04	4.35	4.66	4.51	4.38	4.28
T (K)		918.4	1041.3	1149.8	1293.3	1427.3	1543.9	1630.3	1689.9	1778.8	1789.7	1797.2	1808.1

Table G.5: Mixture 3

Mixture 3													
Date	tau (ms)	MW	C	H	O	C/H ratio	stoich F/A						
3/23/2007	3.95	21.68	1.40	4.80	0.00	0.2918	0.0605						
	R (mm)	0	2	4	6	8	10	12	14	16	18	20	22
NOx	ppm	1.73	4.67	7.41	8.93	9.54	9.74	9.84	9.84	9.74	9.64	9.54	9.44
CO	%	0.57	1.46	0.96	0.44	0.24	0.15	0.10	0.09	0.08	0.09	0.09	0.09
CO2	%	1.19	3.84	6.56	7.28	7.49	7.57	7.65	7.66	7.66	7.65	7.64	7.64
O2	%	17.42	10.63	8.81	8.51	8.41	8.41	8.41	8.30	8.30	8.30	8.30	8.30
NOx - 15% O2	ppm	2.69	2.52	3.49	4.20	4.48	4.59	4.65	4.62	4.57	4.52	4.47	4.43
T (K)		875.0	928.0	1254.2	1520.4	1697.0	1755.8	1776.8	1783.9	1789.4	1795.4	1803.3	1817.6

Table G.6: Mixture 4

Mixture 4													
Date	tau (ms)	MW	C	H	O	C/H ratio	stoich F/A						
6/7/2007	4.24	22.29	1.05	3.39	0.30	0.3093	0.0927						
	R (mm)	0	2	4	6	8	10	12	14	16	18	20	22
NOx	ppm	1.37	2.99	5.53	6.85	7.46	7.76	7.97	7.97	7.76	7.76	7.66	7.56
CO	%	0.41	1.04	1.09	0.54	0.30	0.17	0.12	0.09	0.09	0.10	0.10	0.11
CO2	%	2.13	3.88	6.72	7.83	8.17	8.32	8.37	8.38	8.38	8.37	8.36	8.35
O2	%	17.59	13.19	9.20	8.38	8.28	8.18	8.18	8.13	8.13	8.13	8.13	8.13
NOx - 15% O2	ppm	2.29	2.15	2.68	3.18	3.46	3.59	3.70	3.68	3.59	3.59	3.54	3.49
T (K)		858.7	934.1	1310.2	1584.7	1712.6	1766.5	1788.0	1794.0	1801.1	1810.5	1820.1	1824.0

Table G.7: Mixture 5

Mixture 5													
Date	tau (ms)	MW	C	H	O	C/H ratio	stoich F/A						
6/22/2007	4.16	13.24	0.65	3.2	0	0.203	0.0663						
	R (mm)	0	2	4	6	8	10	12	14	16	18	20	22
NOx	ppm	1.82	4.85	5.45	5.96	6.36	6.77	6.97	7.27	7.37	7.27	7.17	7.17
CO	%	1.04	0.93	0.58	0.4	0.28	0.2	0.15	0.11	0.05	0.05	0.05	0.05
CO2	%	2.03	5.68	6.21	6.42	6.57	6.65	6.7	6.75	6.79	6.79	6.79	6.79
O2	%	13.19	9	8.79	8.69	8.69	8.59	8.59	8.54	8.54	8.54	8.54	8.54
NOx - 15% O2	ppm	1.31	2.32	2.61	2.85	3.05	3.23	3.33	3.47	3.53	3.48	3.43	3.43
T (K)		1012.6	1235	1430.2	1563.9	1660.7	1731.8	1767.9	1790.8	1803	1806.4	1813.6	1817.8

Table G.8: Mixture 6

Mixture 6												
Date	tau (ms)	MW	C	H	O	C/H ratio	stoich F/A					
6/18/2007	4.20	10.40	0.45	2.79	0.00	0.1601	0.0659					
	R (mm)	0	2	4	6	8	10	12	14	16	18	20	22
NOx	ppm	5.61	5.10	5.71	6.53	7.04	7.14	7.24	7.24	7.14	7.04	6.83	6.73
CO	%	0.84	0.62	0.31	0.17	0.10	0.06	0.04	0.04	0.04	0.04	0.04	0.04
CO2	%	5.23	5.45	5.80	5.95	6.06	6.11	6.13	6.14	6.14	6.13	6.13	6.13
O2	%	9.30	9.10	9.00	8.90	8.79	8.79	8.79	8.79	8.79	8.79	8.79	8.79
NOx - 15% O2	ppm	2.77	2.50	2.81	3.20	3.43	3.49	3.54	3.54	3.49	3.44	3.34	3.29
T (K)		1294.0	1341.7	1602.0	1759.4	1803.9	1806.2	1798.4	1796.3	1801.8	1810.0	1815.6	1820.1

Table G.9: Mixture 7

Mixture 7												
Date	tau (ms)	MW	C	H	O	C/H ratio	stoich F/A					
6/11/2007	3.33	22.98	0.75	3.01	0.00	0.2500	0.1110					
	R (mm)	0	2	4	6	8	10	12	14	16	18	20	22
NOx	ppm	1.12	2.74	5.18	6.70	7.31	7.61	7.81	7.81	7.71	7.51	7.41	7.31
CO	%	0.32	0.82	1.10	0.65	0.36	0.21	0.15	0.12	0.12	0.12	0.13	0.14
CO2	%	3.01	4.59	7.09	8.63	9.10	9.29	9.35	9.36	9.36	9.35	9.32	9.32
O2	%	17.84	14.18	9.71	8.28	7.98	7.88	7.78	7.78	7.78	7.78	7.78	7.78
NOx - 15% O2	ppm	2.03	2.27	2.61	3.07	3.31	3.44	3.51	3.51	3.47	3.38	3.33	3.28
T (K)		860.8	933.0	1286.4	1545.4	1691.3	1758.1	1776.1	1785.1	1790.2	1798.6	1806.6	1816.2

Table G.10: Mixture 8

Mixture 8												
Date	tau (ms)	MW	C	H	O	C/H ratio	stoich F/A					
6/11/2007	4.08	24.28	0.65	2.59	0.00	0.2500	0.1363					
	R (mm)	0	2	4	6	8	10	12	14	16	18	20	22
NOx	ppm	1.17	2.59	5.02	6.75	7.46	7.87	7.97	8.17	8.17	7.97	7.87	7.76
CO	%	0.34	0.74	1.14	0.74	0.39	0.23	0.16	0.13	0.13	0.13	0.14	0.16
CO2	%	3.45	4.81	7.12	8.92	9.51	9.72	9.78	9.83	9.83	9.82	9.80	9.78
O2	%	17.48	14.52	9.92	7.98	7.57	7.46	7.36	7.36	7.36	7.36	7.36	7.36
NOx - 15% O2	ppm	1.91	2.26	2.58	3.01	3.27	3.44	3.47	3.56	3.56	3.47	3.43	3.38
T (K)		830.1	912.9	1265.8	1539.9	1679.8	1759.2	1785.6	1796.3	1805.6	1810.9	1821.9	1827.8

Table G.11: Mixture 9

Mixture 9													
Date	tau (ms)	MW	C	H	O	C/H ratio	stoich F/A						
5/16/2007	2.28	29.95	0.50	2.01	0.00	0.2500	0.2162						
	R (mm)	0	2	4	6	8	10	12	14	16	18	20	22
NOx	ppm	1.44	2.77	5.64	7.59	8.30	8.71	8.92	8.92	8.92	8.71	8.51	8.30
CO	%	0.34	0.77	1.32	1.00	0.61	0.42	0.32	0.29	0.28	0.30	0.32	0.33
CO2	%	7.83	9.27	11.78	13.83	14.52	14.80	14.89	14.90	14.90	14.92	14.90	14.89
O2	%	16.41	13.57	8.66	6.28	5.87	5.77	5.77	5.77	5.77	5.77	5.77	5.77
NOx - 15% O2	ppm	1.81	2.12	2.59	2.97	3.21	3.37	3.46	3.46	3.46	3.38	3.30	3.22
T (K)		825.9	894.1	1240.0	1507.9	1666.7	1747.0	1771.3	1785.6	1792.7	1799.8	1809.2	1813.0

Table G.12: Mixture 10

Mixture 10													
Date	tau (ms)	MW	C	H	O	C/H ratio	stoich F/A						
2/12/2007	4.10	12.58	0.36	2.08	0.11	0.1731	0.1108						
	R (mm)	0	2	4	6	8	10	12	14	16	18	20	22
NOx	ppm	4.57	5.78	6.98	7.59	7.89	7.99	7.99	7.99	7.89	7.79	7.79	7.79
CO	%	0.84	0.51	0.28	0.16	0.10	0.06	0.05	0.04	0.04	0.04	0.04	0.04
CO2	%	7.11	7.42	7.61	7.73	7.82	7.86	7.87	7.88	7.89	7.90	7.90	7.90
O2	%	8.90	8.90	8.79	8.79	8.79	8.79	8.79	8.79	8.79	8.79	8.90	8.90
NOx - 15% O2	ppm	2.18	2.79	3.38	3.69	3.85	3.90	3.90	3.90	3.85	3.81	3.84	3.84
T (K)		1333.0	1321.0	1463.2	1669.1	1786.4	1800.2	1793.1	1790.0	1787.6	1790.1	1797.3	1803.8

Table G.13: Mixture 11

Mixture 11													
Date	tau (ms)	MW	C	H	O	C/H ratio	stoich F/A						
2/18/2007	3.59	18.50	0.68	1.04	0.58	0.6538	0.2067						
	R (mm)	0	2	4	6	8	10	12	14	16	18	20	22
NOx	ppm	2.28	3.20	5.13	6.55	7.36	7.66	7.56	7.66	7.56	7.46	7.26	7.16
CO	%	3.00	2.08	1.03	0.56	0.31	0.18	0.13	0.11	0.10	0.10	0.10	0.10
CO2	%	6.90	7.62	8.62	9.11	9.40	9.53	9.59	9.61	9.61	9.62	9.62	9.63
O2	%	11.68	11.38	10.76	10.56	10.25	10.15	10.04	10.04	10.04	10.04	10.04	10.04
NOx - 15% O2	ppm	1.26	1.79	2.85	3.65	4.03	4.18	4.10	4.16	4.11	4.05	3.94	3.89
T (K)		1221.3	1292.3	1466.8	1675.5	1789.7	1813.8	1813.9	1810.3	1810.1	1809.5	1813.3	1824.8

Table G.14: Mixture 12

Mixture 12													
Date	tau (ms)	MW	C	H	O	C/H ratio	stoich F/A						
4/10/2007	3.54	44.10	3.00	8.00	0.00	0.3750	0.0641						
	R (mm)	0	2	4	6	8	10	12	14	16	18	20	22
NOx	ppm	3.22	6.33	7.64	8.54	8.94	9.14	9.25	9.14	9.04	8.94	8.64	8.44
CO	%	2.30	1.43	0.70	0.38	0.21	0.13	0.10	0.09	0.09	0.10	0.11	0.11
CO2	%	3.01	6.46	7.36	7.73	7.92	7.98	8.01	8.03	8.01	8.00	8.00	8.00
O2	%	9.94	9.43	9.13	9.02	8.92	8.92	8.92	8.87	8.87	8.87	8.87	8.87
NOx - 15% O2	ppm	1.57	3.08	3.73	4.20	4.39	4.50	4.55	4.49	4.44	4.39	4.24	4.14
T (K)		994.0	1058.3	1384.0	1592.4	1706.8	1759.3	1775.3	1779.2	1787.5	1793.8	1795.7	1807.8